Alma Mater Studiorum – Università di Bologna

DOTTORATO DI RICERCA IN

Ingegneria Ambientale, Civile e dei Materiali

Ciclo XXVII

Settore Concorsuale di afferenza: 08 A2

Settore Scientifico disciplinare: ING/IND 30

TITOLO TESI

Valorisation of organic waste: new developments from proton nuclear magnetic resonance characterization

Presentata da: ***Marianna Vannini***

Coordinatore Dottorato **Relatore**

Alberto Lamberti ***Villiam Bortolotti***

Esame finale anno 2015

Abstract

The last half-century has seen a continuing population and consumption growth, increasing the competition for land, water and energy. The solution can be found in the new sustainability theories, such as the industrial symbiosis and the zero waste objective. Reducing, reusing and recycling are challenges that the whole world have to consider. This is especially important for organic waste, whose reusing gives interesting results in terms of energy release. Before reusing, organic waste needs a deeper characterization. The non-destructive and non-invasive features of both Nuclear Magnetic Resonance (NMR) relaxometry and imaging (MRI) make them optimal candidates to reach such characterization. In this research, NMR techniques demonstrated to be innovative technologies, but an important work on the hardware and software of the NMR LAGIRN laboratory was initially done, creating new experimental procedures to analyse organic waste samples. The first results came from soil-organic matter interactions. Remediated soils properties were described in function of the organic carbon content, proving the importance of limiting the addition of further organic matter to not inhibit soil processes as nutrients transport. Moreover NMR relaxation times and the signal amplitude of a compost sample, over time, showed that the organic matter degradation of compost is a complex process that involves a number of degradation kinetics, as a function of the mix of waste. Local degradation processes were studied with enhanced quantitative relaxation technique that combines NMR and MRI. The development of this research has finally led to the study of waste before it becomes waste. Since a lot of food is lost when it is still edible, new NMR experiments studied the efficiency of conservation and valorisation processes: apple dehydration, meat preservation and bio-oils production. All these results proved the readiness of NMR for quality controls on a huge kind of organic residues and waste.

Nomenclature

^{1}H NMR = Proton Nuclear Magnetic Resonance

BET = Brunauer–Emmett–Teller adsorption technique

CPMG = Carr-Purcell-Meiboon Gill

FID = Free Induction Decay

FOV = Field Of View

FT = Fourier Transform

FW = Food Waste

IR = Inversion Recovery

LAPSRSE = Logarithmically Aperiodic Saturation Recovery Spin Echo

MIP = Mercury Injection Porosimetry

MRI = Magnetic Resonance Imaging

MRR = Magnetic Resonance Relaxometry

NMR = Nuclear Magnetic Resonance

OM = Organic Matter

PSD = Pore Size Distribution

QRT = Quantitative Relaxation Tomography

RF = Radiofrequency

SE = Spin Echo

S/N = Signal to Noise ratio

SR = Saturation Recovery

TD-NMR = Time-Domain Nuclear Magnetic Resonance

TD-MRR = Time-Domain Magnetic Resonance Relaxometry

B_0 = static (external magnetic field)

B_1 = induced magnetic field

T_1 = spin lattice or longitudinal relaxation time

T_2 = spin spin or transverse relaxation time

R_1 = spin lattice or longitudinal relaxation rate

R_2 = spin spin or transverse relaxation rate

ρ = surface relaxivity

S/V = surface to volume ratio

φ = porosity

TE = Time of Echo

TR = Time of Repetition

Chapter 1

Introduction

1.1 The importance of the characterization, identification and valorisation of waste driving toward a zero waste society

Agricultural, food and industrial waste is generated daily in extensive quantities, producing a significant problem in its management and disposal. A widespread feeling of "environment in danger" is increasing in our society year by year, which, however, is not yet crystallized in a general consciousness of cutting waste production in our daily lives. Landfill, incineration and composting are common, mature technologies for waste disposal. However, they entail many problems related to the generation of toxic methane gas and bad odour, high energy consumption and slow reaction kinetics (Arancon et al.; 2013).

Since the development of innovative systems to maximize the recovery of useful materials and/or energy in a sustainable way has become necessary, a new concept, the industrial symbiosis concept, is becoming popular in both scientific and sociological field. Industrial wastes are generated through different industrial processes or energy production utilities as surplus materials. The industrial symbiosis theory defines non-deliberately produced material as by-products or valuable raw materials which can be exploited in other industrial ways.

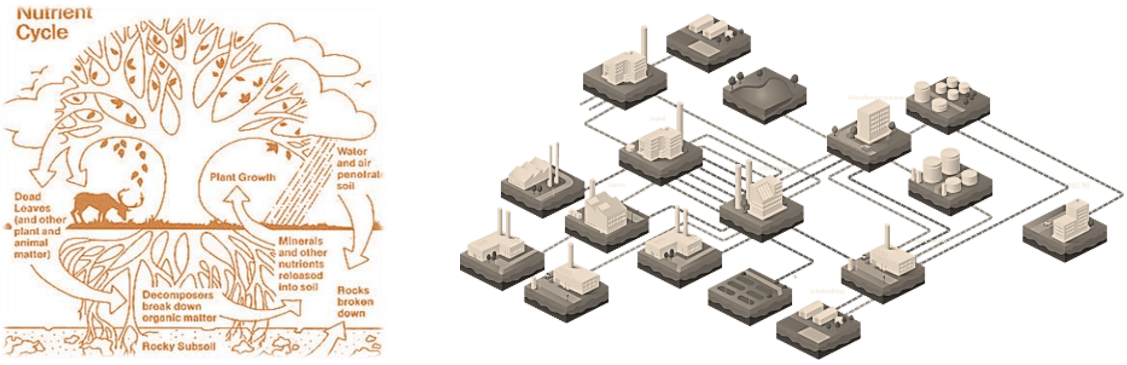

Figure 1.1.a) *Nutrients cycle in nature,* 1.1.b) *industrial symbiosis scheme.*

This idea is inspired by the nature cycles, where the concept of waste does not exist (Figure 1.1.a). Industrial symbiosis is the ingenious idea that one company's waste becomes another's raw material, leading to enormous carbon, costs and resources savings (Figure 1.1.b).

The percentage and weight of waste components in a solid waste stream are important data for decision-makers. This information is necessary to plan waste reduction and recycling programmes to reach the zero waste objective.

According to the figures, in Europe, as well as in Italy, the waste stream is made of huge quantities of materials that are well away from their end of life. Furthermore, it is quite evident how some materials are definitely more wasted than others, therefore more efforts have to be done to reuse or valorise them. Among these materials there are: organic waste, with 25% for EU27 and 42% for Italy, and paper, with 18% for EU27 and 24% for Italy. Other types of waste that follow are plastic, RAEE and metals (Figure 1.2.a and 1.2.b).

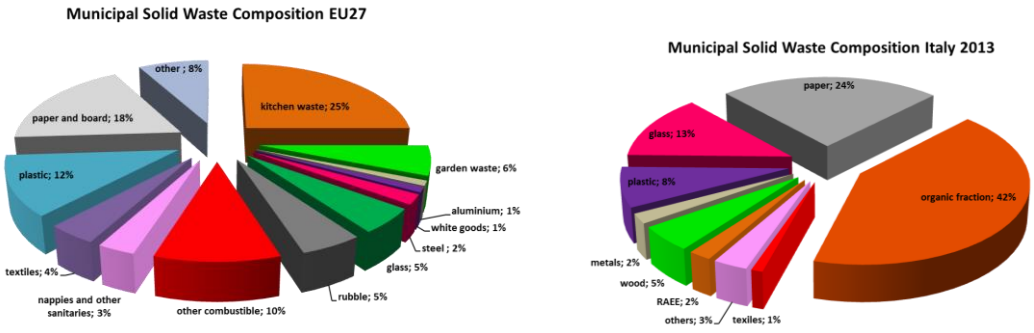

Figure 1.2.a) *Municipal solid waste composition for EU27, adapted from www.zerowasteurope.eu, source Eurostat;* 1.2.b) *municipal solid waste composition for Italy.*

The problem of food waste, in particular, is gaining attention day by day for a number of reasons: the 15% of population in developing countries is starving, world population is increasing almost exponentially and the energy crisis is forcing every country to

adopt stricter energy saving solutions. The production of food waste concerns all the food life cycle starting from agriculture, up to industrial manufacturing and processing, retail and household consumption. All of these stages produce large amounts of waste. The food and drink industry represents a large and economically important sector in Europe, as much as in Italy, but until the recent past, the food waste phenomenon was underestimated. Only in 2011 a study provided a quantification of the waste along the whole food supply chain: 20 million tons from the field to the point of sale (Figure 1.3; Segrè and Falasconi, 2011).

FOOD CATEGORIES	QUANTITY AVAILABLE g/PERSON/DAY (A)	ESTIMATED CONSUMPTION g/PERSON/DAY (B)	SURPLUS% (A) - (B)
Grains, grain products and substitutes	433	258	40%
Vegetables, fresh and processed	463	211	54%
Fruit, fresh and processed	418	208	50%
Alcoholic beverages and substitutes	205	91	55%
Meat, meat products and substitutes	242	110	54%
Fish and fish products	67	44	33%

Source: Segrè and Falasconi, 2011.

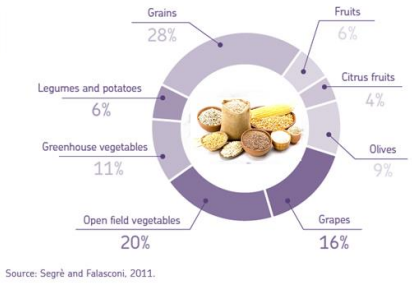

Source: Segrè and Falasconi, 2011.

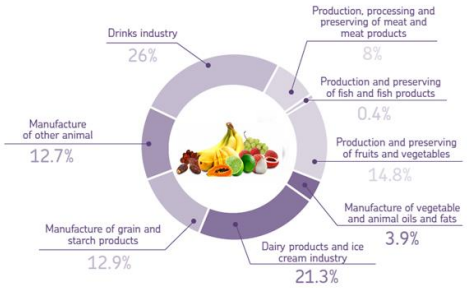

Source: Segrè and Falasconi, 2011.

Figure 1.3. *Percentages of agricultural production remaining in field and percentage breakdown of waste in the food industry in Italy. Extracted from Barilla centre food and nutrition report on "Food waste causes impacts and proposals", 2012.*

In general the large amount of waste produced by the food industry, in addition to being a great loss of valuable materials, also raises serious management problems, both from the economic and environmental point of view. Many of these residues,

however, have the potential to be reused into other production systems, e.g. in the biorefineries. A sustainable agro-food industry recognizes that waste prevention, minimization and valorisation, rather than 'end of pipe', are the required solutions for waste management. However, strategies and technologies to secure economic and environmental solutions for an effective management of food by-product and waste still have to be implemented. In general, such streams are nowadays only partially valorised at different value-added levels (spread on land, animal feeding, composting, among others), whereas the main volumes of them are managed as waste of environmental concern with relevant negative effects on the overall sustainability of the food processing industry (Fava et al., 2013).

This happens, in general for all types of waste, also because of the lack of waste information. Usually the types and the quantity of the different components that can be found in a waste stream are often lacking or unknown, even these information are very important for the waste management planners, the local officials and material recovery facility designers. In conducting a study of local (regional, …) conditions, a variety of waste characterization methods can be used. Computer models generally use national averages for waste generation rates and other community features to calculate waste quantities. An alternative is to use materials-flow surveys based on production data for the materials and products in the waste stream, with adjustments for imports, exports and product lifetimes. Both approaches neglect some important aspects: the first does not account for local waste characteristics that can vary significantly from national or regional averages, the second never collects physical samples and it is difficult to apply when waste characteristics are evaluated at a facility such as a landfill or a treatment facility (Zeng et al.; 2005).

Collecting and characterizing samples is a good practice, which must be considered at various stages of the waste chain. First, characterization is needed to identify waste composition and properties among a waste stream. This could be useful to choose the best disposal option. Then, if the disposal option concern reuse (e.g. organic waste for

composting), a new characterization would be required to monitor the quality of the intervention. Furthermore, if the waste can be even valorised extracting new products (chemicals, materials, fuels, etc) from it, a deep characterization would be important to assess the quality of the originated by-product.

The already known practises to reuse waste, especially organic waste, such as composting or soil remediation, have proved to be satisfactory in many cases, if well monitored, but the new horizon of waste reuse is valorisation. Such concept comes from the past and it was mostly related to waste management, but it has been brought back to our society with renewed interest due to the fast depletion of natural and primary resources, the increased waste production and the need for more sustainable and cost-efficient waste management protocols (Arancon et al., 2013). Various valorisation techniques seem to be promising in meeting industrial demands, above all because of the need of products and processes that minimize the use and generation of hazardous substances, which is the concept of green chemistry.

There are a lot of test methods, supported by international standards, to characterize many types of waste, but a constant improvement of scientific methods is needed, moreover test methods produce waste themselves. So, further efforts are needed to make also test methods greener.

In this research thesis, Nuclear Magnetic Resonance (NMR) Relaxometry (MRR) and imaging (MRI) have been proposed, almost for the first time, to characterize organic waste materials and by-products. The strength of this technique consists in its non-destructive and non-invasive features. Magnetic resonance employs magnetic fields and radiofrequencies devices to obtain information on the nuclei on which the system is tuned. The analysed samples generally can be measured without any significant treatment and, after the measure, they can be reused. NMR is hence non-invasive and non-destructive.

The typical applications of MRR and MRI concern petrophysical and biomedical fields, so its use in environmental field is quite new. This is the reason why this work starts with

an optimization of the hardware and software, in this case of the NMR LAGIRN laboratory: to use NMR equipment on this kind of samples specific experimental features have been improved and adopted.

After such preliminary, but essential, work some cases study have been analysed to fully demonstrate the power of this techniques.

It has been found that MRR technique can give information on the porosity of soils treated with organic waste (in this case paper sludge). In particular the study of the microporosity (< 2 μm) has confirmed that organic matter (OM) clogs this range of pores. This evidences that high OM contents affect soils structure and they may produce negative effects on them, like anaerobic degradation, with biogas production.

Then, biodegradation of compost, obtained by domestic organic waste, has been detected with both MRR and MRI, highlighting the possibility to follow OM biodegradation, establishing the maturity of compost both globally and locally, to detect eventual compost components not well degraded.

As the waste chain that leads to the production of organic waste can be further improved, other studies, which are still in progress, that conclude the experimental developments of the thesis, are focused on the reducing of organic waste, in particular of food waste.

MRR and MRI have been employed to control the efficiency of the process of fruit dehydration, which is a practice largely used to avoid food waste.

The PERFIDI filters (Sykora et al., 2007) have been employed in MRI to separate the signal in the animal meat, of the fat from that of the muscle, to improve quality controls, and to finally sell meat on the basis of its nutritional characteristics.

Then bio-oils, which are the liquid products from biomass valorisation processes, have been studied to be selected on the basis of their quality, to further propose the best way to be employed.

All these applications confirm that NMR is an innovative technique ready to be used for characterization and for quality controls on organic waste.

Chapter 2

Low-field Nuclear Magnetic Resonance

2.1 Introduction to low-field NMR application to industrial processes

The first Nuclear Magnetic Resonance (NMR) experiment in bulk materials date back to 1946 by Bloch, Hansen, and Packard at Stanford and by Purcell, Torrey and Pound at Harvard. The importance of their discovery was recognized, in 1952, with the Nobel Prize in Physics awarded to Bloch and Purcell. In the past 60 years NMR has bloomed in the form of different techniques: spectroscopy, relaxometry and imaging (Becker, 1993). Each technique is leader in a specific field, for example, MRI has traditionally been employed in clinical medicine, presenting a non-destructive technique for biomedical investigations, becoming today one of the most valuable clinical diagnostic tool in health care. High-resolution NMR spectroscopy provides a method of structural determination for complicated molecules such as proteins, but it also allows studies on molecular interactions including enzyme activity (Mitchell et al., 2014). MRR is strongly used in petroleum industry as a well-logging tool. In general NMR applications are still more than those currently explored.

Not all NMR techniques use the same field strength. Even if there has been a continual drive towards the use of high magnetic field, not necessarily very strong magnetic fields are desirable in all scientific contexts. At present, in several industrial fields, low-field NMR, frequently associated to permanent magnets, is to be preferred as it can provide a suitable compromise between magnetic field strength and experimental versatility for installation in industrial environments and it allows the investigation of heterogeneous materials. Moreover no cryogenic cooling is needed, economic costs are restrained, safety measures are limited (in some cases negligible) and, last but not the least, the design versatility of the magnet permits also open-access and single sided magnet arrangements. A disadvantage to take in particular care is the field stability in case of thermal fluctuations, for this reason

excellent thermal regulation is essential on permanent magnet low field systems designed for such experiments (Mitchell et al., 2014).

The majority of low-field experiments exploit ^{1}H (proton) spins; the high natural abundance and large gyromagnetic ratio of the hydrogen nucleus provides a detectable magnetization even with low-field instrumentation (Mitchell et al., 2014). For these reason it is not difficult to imagine how many applications this technique could have. There are several fields in which low-field NMR is already successful, and others in which its potentialities are not fully developed. In the world of industries it is possible to find a number of low-field NMR applications, but it is worthy to say that in the petroleum production, the food manufacture and the built environment there are the most successful ones. Low-field NMR plays two important roles in oil and gas production: well-logging tools provide access to ''reservoir-scale'' measurements of the formation fluids, whereas bench-top instruments are used to examine fluids and cored plugs of rock recovered from the reservoir. Bench-top, or laboratory, NMR systems provide fluid characterization, rock properties, and a platform for trialling new recovery methods prior to single-well pilots in the reservoir. Moreover low-field bench-top magnets are used in process control in the food industry. Total signal intensity, relaxation time distributions, or diffusion measurements (e.g. for droplet size distributions) can be evaluated and monitored. These low-field instruments can be installed to operate readily in an industrial environment. Low-field NMR and MRI has been used as a characterization and quality control tool for a wide range of food products including bread and biscuit dough, potatoes and potato starch, tomatoes, apples, processed soybean protein, and powdered food products, to cite but a few of the more recent studies. Advanced imaging techniques have been used to investigate oil and water in fried foods. Finally in civil engineering and construction industry low-field NMR is providing increased understanding of construction materials: rocks, cement and

wood, and the application of mobile NMR for conserving ancient buildings (Mitchell et al., 2014).

A part from these most popular applications low-field NMR can also be applied to study a whole range of physico-chemical properties and processes relevant in the field of reuse and valorisation of waste. One of the central problems is that industrial processing activities produce in Europe large amounts of by-products and waste and such waste streams are only partially valorised whereas the main volumes are managed as waste of environmental concern, with relevant negative effects on the overall sustainability. Hence the realization of regional synergies in industrial areas with intensive processing provides a significant avenue toward sustainable resource processing. To do that the need of valorise waste and by-products is becoming urgent, so wastes from one sector become the input for other sectors. The first step for applying these industrial symbiosis concepts is the identification, quantification and characterization of residues (Mirabella et al. 2013). Thanks to its non-destructive and non-invasive features, low-field NMR is a suitable candidate to explore the output of this topical sector.

2.2 Basics of NMR theory

The NMR technique is based on the magnetic properties of atomic nuclei. The phenomenon of nuclear magnetic resonance occurs when the nuclei of certain atoms are immersed in a static magnetic field and exposed to a second oscillating magnetic field. Some nuclei experience this phenomenon, while others do not, depending on whether or not they possess non-zero values of a quantum mechanical property known as spin. Nuclear spin has a magnetic moment associated with it which will interact with an applied magnetic field. When a nucleus with spin, I = 1/2, such as a proton is placed in a magnetic field, two energy levels are generated. These energy levels can be

characterized by the magnetic spin quantum number, m_I, and are separated by an amount ΔE, which is given by:

$$\Delta E = \hbar \gamma B_0 = \frac{h \gamma B_0}{2\pi} \qquad (2.1)$$

where γ is the gyromagnetic ratio, B_0 is the applied static magnetic field, h and $\hbar$ are respectively the whole and reduced Planck constants.

The gyromagnetic ratio is a proportionality constant which relates the observation frequency for a particular nucleus to the applied field. The lower energy state, in which the nuclear magnetic moment is parallel to the applied magnetic field B_0, corresponds to m_I = + 1/2. The higher energy state in which the magnetic moment is antiparallel to B_0 corresponds to m_I = -1/2.

In the presence of the magnetic field the magnetic moment precesses around the applied field, with a precession frequency, Larmor frequency, which can be expressed in terms of the gyromagnetic ratio and the applied field as:

$$\nu = \frac{\gamma B_0}{2\pi} \qquad \text{or} \qquad \omega = \gamma B_0 \qquad (2.2)$$

where, ω is the resonant frequency in radians/second and ν is the resonant frequency in hertz. The two energy states (α,β) will be unequally populated, with the ratio of their populations given by the Boltzman equation:

$$\frac{N_\beta}{N_\alpha} = e^{\left(\frac{-\Delta E}{kT}\right)} \qquad (2.3)$$

where, N_α is the population of the lower state and N_β is the population of the higher state.

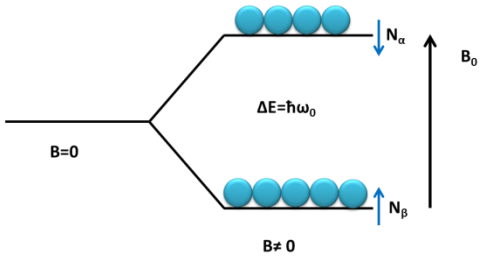

Figure 2.1 Schematic representation of the two energy states generated on protons by the B_0.

Although individual spins obey the law of quantum mechanics, the average behaviour of a group of ½-spins experiencing the same magnetic field strength, can be described using the classical mechanic. So it is possible to say that the population difference is dependent both on the field and the nucleus being observed, and it corresponds to a bulk magnetization (M), which is the sum of the magnetizations of the individual spins.

Since the magnetic moment has magnitude and direction, its behaviour in a magnetic field is usually described using vector diagrams. Initially, the bulk magnetization M, will be aligned with the applied magnetic field, till the system is perturbed (Figure 2.2 a)). The direction of the applied field is defined, for practice, as the *z* direction. If the induced magnetization is misaligned from the applied field B_0, a force acts on M. This magnetization is generated from nuclear spins and as a result, it behaves in a manner similar to that of a spinning top in the Earth's gravitational field. The torque exerted by B_0 on M causes M to precess around B_0 (Figure 2.2 a)) at a frequency of $\gamma B_0/2\pi$ hertz. This motion is known as Larmor precession. If a coil of wire is wound around an axis perpendicular to the B_0 field, the precessing magnetization would induce an oscillating current in the coil. After necessary amplification and processing, this current becomes the NMR signal. The coordinates *x*, *y*, *z* are in the three-dimensional "laboratory frame of reference".

From the perspective of the nuclei, these coordinates are rotating at the Larmor frequency. If the *x*, *y* coordinates are changed to those in the rotating frame *x'*, *y'*, the magnetization appears static. The net magnetization now lies along *z'* and its behaviour at equilibrium is shown in Figure 2.2 b).

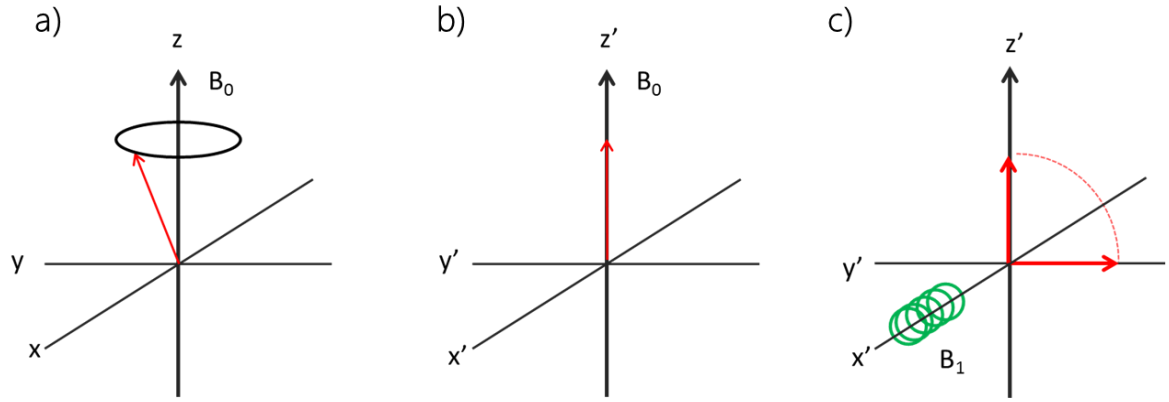

Figure 2.2 *Behaviour of the bulk magnetization (M): **a)** at equilibrium in laboratory frame of reference; **b)** at equilibrium in the rotating frame of reference; **c)** application of a B_1 to displace the magnetization from the equilibrium.*

In an NMR experiment, the magnetization is displaced from its equilibrium position by applying a second magnetic field B_1, which oscillates at the Larmor frequency. This field is induced from a current in a coil perpendicular to B_0 and is applied for a few microseconds. This rf field is also at the Larmor frequency. As the introduced rf radiation exactly matches the energy difference between the two states, the energy is absorbed and the nuclei are in resonance with the electromagnetic radiation. The frequency of radiation needed to induce resonance also depends on the nature of electronic shielding around the nucleus. Different functional groups or bond types in organic molecules have different electron distributions and thus their constituent nuclei resonate at different frequencies. Therefore it is possible to identify a particular functional group from its resonance frequency.

2.3 NMR relaxation and Bloch's equations

The response of an isolated proton's spin in an external magnetic field has been modelled by the classical equations of motion of a single magnetic moment. The use of classical precession picture for static fields, and of the rf induced rotation of magnetic moments in the rotating reference frame for spin ½ is justified by specific quantum analyses. In thermal equilibrium conditions the magnetization is oriented along the B_0 field. In order to change the condition of the system rf pulses can be used to displace the magnetization from the equilibrium. These pulses generally rotate the magnetization of 90°or 180°degrees. When magnetization is rotated it is not in a stable condition, so the systems returns in the equilibrium state, this is called *relaxation process*.

It is possible to distinguish two processes of relaxation: the *longitudinal relaxation* and the *transversal relaxation*. The environment surrounding a nucleus is often summarily described as a lattice. The thermal motions of the lattice set up fluctuating electric and magnetic fields at the nuclei position. The interaction of the nuclear moments with these fields helps stimulate the transitions between the magnetic energy levels by emitting or absorbing energies to or from the surroundings. This process, called spin-lattice relaxation, eventually leads to thermal equilibrium. A constant interaction growth rate of the proton interactions with the lattice implies that the rate of change of the longitudinal magnetization is proportional to the difference M_0 - M_z. The proportionally constant represents the inverse of the time scale of the growth rate "T_1":

$$\frac{dM_z}{dt} = \frac{M_0 - M_z}{T_1} \tag{2.4}$$

The solution is for $\vec{B} = B_0\hat{z}$ and M_0 is the magnetization equilibrium value.

$$M_z(t) = M_z(0)e^{-\frac{t}{T_1}} + M_0(1 - e^{-\frac{t}{T_1}}) \quad (2.5)$$

Where T_1 is the longitudinal, or *spin-lattice* relaxation time. This time reflects how effectively the magnetic energy of the spin system is transferred to or from its surroundings. A large T_1 corresponds to weak coupling and a slow approach to equilibrium, whereas a small value of T_1 indicates strong coupling and a rapid approach to equilibrium. The transversal relaxation, which is also called *spin-spin* relaxation, occurs in the *xy* plane and it can be described by the following equation, in the rotating reference frame:

$$\frac{d\vec{M}_\perp}{dt} = -\frac{\vec{M}_\perp}{T_2} \quad (2.6)$$

With the solution:

$$\vec{M}_\perp(t) = \vec{M}_\perp(0)e^{-\frac{t}{T_2}} \quad (2.7)$$

Any process that causes the loss of transverse magnetization, including the return to the z axis, contributes to T_2. The first thing that comes into consideration is the inhomogeneity of the static field B_0; recall that the magnetization vector M, when processing in the *xy* plane about B_0, is actually composed of all spins of the system and all of them processing about the *z* axis. As a result, spins are precessing at slightly different Larmor frequencies, becoming out of phase. Moreover the decay of magnetization in the *xy* plane is frequently dominated by the field inhomogeneity effect, and the transverse relaxation time is generally referred to as T_2^* which represents the sum of these effects. It is possible to experimentally separate the loss of

magnetization due to macroscopic field inhomogeneity from that due to other causes. In other words it is possible to experimentally lead to a rephasing of the spins.

In solids the nuclei are not free to move around. Hence, no matter how uniform the applied field is, the local magnetic fields due the neighbouring nuclei in the material can cause T_2 to be very short.

In contrast, the nuclei in liquids move so fast that they average out the varying local fields so quickly that the only cause for transverse relaxation is the returning of the magnetization to the z axis. Thus frequently T_2 equals T_1 in liquids. However, T_2 can never be longer than T_1.

The differential equations (2.4) (2.6) are the Bloch's equations and they can be summarized as (in the laboratory reference frame):

$$\frac{d\vec{M}}{dt} = \gamma \vec{M} \times \vec{B}_0 + \frac{1}{T_1}\left(M_0 - M_z\right)\hat{z} - \frac{1}{T_2}\vec{M}_\perp \tag{2.8}$$

The general time-dependent solution for the transverse components is seen to have sinusoidal terms modified by a decay factor. The sinusoidal terms correspond to the precessional motion and the damping factor comes from the transverse relaxation effect. The longitudinal component relaxes from its initial value to the equilibrium value M_0.

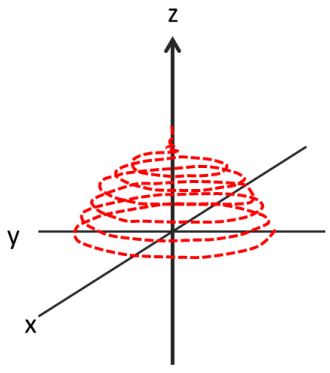

Figure 2.3 *Representation of the precession motion.*

2.3.1 How to do a NMR experiment: rf pulse sequences

In a typical laboratory NMR apparatus, the sample is placed in a sample holder which is positioned between the poles of the magnet. An induction coil is looped around the sample holder such that the generated magnetic field direction is at right angles to the field magnet B_0.

The coil is crossed by pulses of current at the Larmor frequency of the nucleus interrogated. The duration of these pulses determines the angle which the spins are turned apart from the direction of the B_0. After the pulse is turned off, the same coil or an additional coil is used to measure the decay or relaxation of the signal. The signal in the coil is induced by the precession of the spins around the static field in the transverse plane.

A sequence is a series of rf pulses with different duration or intensity. Rf pulses permit to rotate the magnetization of a certain angle (90° or 180°). The effect of a series of rf pulses is to obtain a signal which carries information only on T_1 or T_2 relaxation times. For this reason it can be said that there are T_1 or T_2 measurements.

If for example, a 90° pulse is used, the signal that we measure is called the Free Induction Decay (FID). The FID is largely influenced by T_1, T_2, magnetic field uniformity and by the presence of paramagnetic centres. Generally speaking, a long FID, when Fourier transformed to the frequency domain, gives a narrow peak at the Larmor frequency, whereas a short FID, exhibits a wide peak, indicating a heterogeneous field distribution over the sample. For example rock samples, due to very heterogeneous field, typically have a very broad peak in the frequency domain (Figure 2.4).

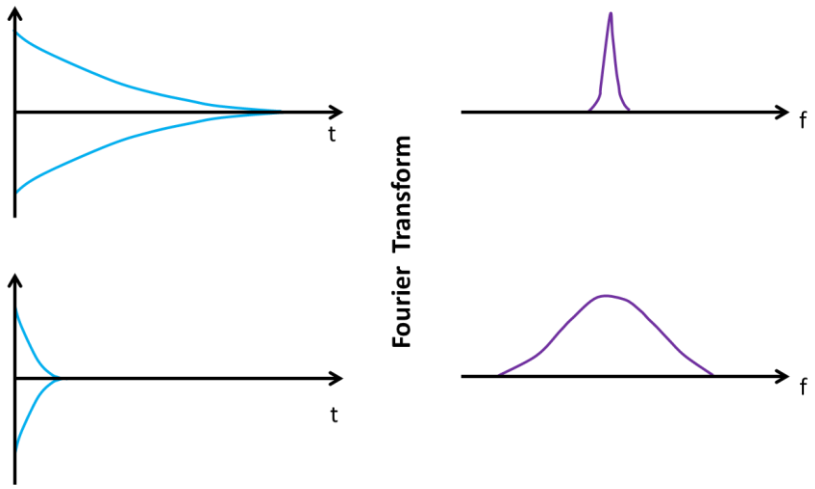

Figure 2.4 *Different FIDs and the respective representation in the frequency domain.*

Because of the complexity of FID interpretation, multi-pulse sequences have evolved to separate out these effects.

2.3.2 T_1 measurements

To measure the longitudinal relaxation, the *inversion recovery* (IR) pulse sequence has the advantage to almost eliminate any T_2 effects. The sequence consists of a 180˚ inversion pulse followed by a recovery time and then a 90˚ "read" pulse.

The 180˚ pulse inverts the magnetization vector from the positive z' direction axis to the negative z' directions axis. Longitudinal relaxation now occurs, causing the magnetization to go from $-M_0$ to M_0 (equilibrium). If at the time t, after the 180˚ pulse, a 90˚ pulse is applied, still along the x' axis, M is rotated to the y' axis. A FID results, whose initial height is proportional to $M_{z'}$ at time t. The system will return to equilibrium by waiting at least five time the maximum T_1 value. The solution for the Bloch's equations for inversion recovery is (Farrar & Becker, 1971):

$$M(t) = M_0(1 - 2e^{-t/T_1}) \qquad (2.9)$$

How much the vector grows in the $+z$ direction during the variable recovery period also cannot be directly measured because there is no transverse component.

The purpose of the subsequent 90˚ pulse is to tilt the magnetization into the plane of the receiving coil where it can be acquired. A FID follows the 90˚ pulse, which strength is related to the growth of the magnetization along the positive z axis that has occurred since the initial 180˚ pulse.

A sequence of such experiments consists of a number of FIDs which are acquired at different inversion times. T_1 can be computed from fitting data to equation (2.9).

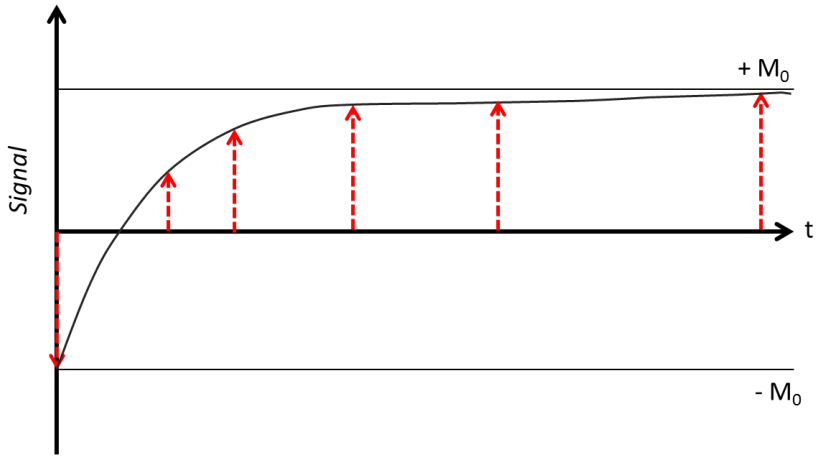

Figure 2.5 *Signal of a typical IR experiment.*

Another sequence, used to measure the T_1 relaxation time, is the *saturation recovery* (SR), which uses a 90˚ pulse followed by a 90˚ "read" pulse. The magnetization of the saturation recovery is described by the following equation:

$$M(t) = M_0(1 - e^{-t/T_1}) \tag{2.10}$$

The popularity of the IR method is due to the fact that the dynamic range for magnetization is $2M_0$ as opposed to M_0 for the saturation recovery. However SR has the advantage of having an arbitrary short delay between two pulse pairs, so reducing

the whole acquisition time (Dunn et al., 2002). This procedure is limited to cases where $T_2 << T_1$, otherwise the magnetization remaining along the y' at time t would be rotated to the z' axis and would invalidate the equation to determine T_1 (Farrar & Becker, 1971).

2.3.3 Field inhomogeneities and T_2 measurements

The signal received by the rf detector coil is determined not just by the properties of the sample but also by magnetic interactions. The T_2 relaxation is related to the dephasing of the nuclear spins that are the result of local field inhomogeneities, among other things. The T_2 relaxation mechanisms are best examined when **M** is first rotated of 90°.

As already said, the constant B_0 is not particularly uniform over the whole sample, so the behaviour of the individual spins that contribute to the 90° rotated **M** (they should all be rotating together at the Larmor frequency), for one reason or another, do not rotate at exactly the same frequency. Thus in time they begin to noticeably get out of phase. In doing so, the magnitude of the vector M will decrease with time, with an exponential decay characterized by the T_2^* constant.

Alteration of the spin precession frequency come from the mutual interaction (spin–spin) of the proton spins (intrinsic dephasing T_2). In summary the apparent decay time will be composed, in part, of the spin–spin interactions, as well as a component due to local field inhomogeneities.

Another cause of the signal decay will be, not the dephasing, but the reorienting of the rotated spins to the direction of B_0. As said before, since B_0 has remained on, the z-component of the source magnetization will increase from its initial value of zero to a final value of M, with a characteristic time constant T_1 which is generally much longer than T_2 except in bulk liquids. Another source of dephasing, of interest for protons in fluids contained in pores, concerns interaction of the proton spins with the pore walls.

All of the sources of relaxation (or signal decay) that are not reversible are lumped into the quantity referred to as T_2.

The time evolution, after a 90˚ pulse, is suggested in Fig. 2.6 (first row). After the **M** vector has been rotated by 90˚ it is seen at its maximum along the *y'* axis. Because of the slight field differences at various parts of the sample, each of the protons may have a slightly different precessional frequency. In regions where the field is slightly larger by an amount δB the protons will precess at a slightly faster rate, $\gamma (B_0 + \delta B)$. After a time *t* these protons will have advanced by an amount $(\gamma\delta B)t$ radians over the ones precessing in the nominal field B_0. The converse is true for the protons that find themselves precessing in a slightly smaller field. The spins from these various regions will tend to separate. As time progresses the spins dephase, decreasing the size of the *y'* axis projection of **M**.

To make a measurement of T_2, it is necessary to remove from the measurement any reversible dephasing. This can be obtained by applying an Hahn echo, which is generally employed in the rf pulse sequence, the *spin echo* (SE). The Hahn echo is obtained when after the 90˚ pulse, one applies a 180˚ pulse.

When the 180˚ pulse is applied, gradually the entire arrangement of proton spins can be flipped around their position on the transverse plane so that now the slower-precessing protons will lead, and the faster ones will follow (Figure 2.6, second row). The accumulated phase of all spins experiencing a time-independent field variation will return to zero at a time called Time of Echo (T_E). Therefore it is clear that all of the spins will be realigned at the same time and the realignment is called "spin echo".

The SE technique is limited in its range of applicability because of the effect of molecular diffusion. The refocusing of all the spins is dependent upon each nucleus remaining in a constant magnetic field during the time of echo. If diffusion causes nuclei to move from one part of an inhomogeneous field to another, echo amplitude is reduced. In general the effect of diffusion in the SE experiment is dependent upon the

spatial magnetic field gradients, the diffusion coefficient and the time during which diffusion can occur.

This problem can be solved by applying many 180° pulses, spaced by a short half time of echo, and alternating the phase of this pulses (Farrar & Becker, 1971). This particular technique origins the pulse sequence called the *CPMG* pulse train after its inventors Carr and Purcell, and Meiboom and Gill. In this sequence the number of echoes which can be acquired is directly related to T_2 processes.

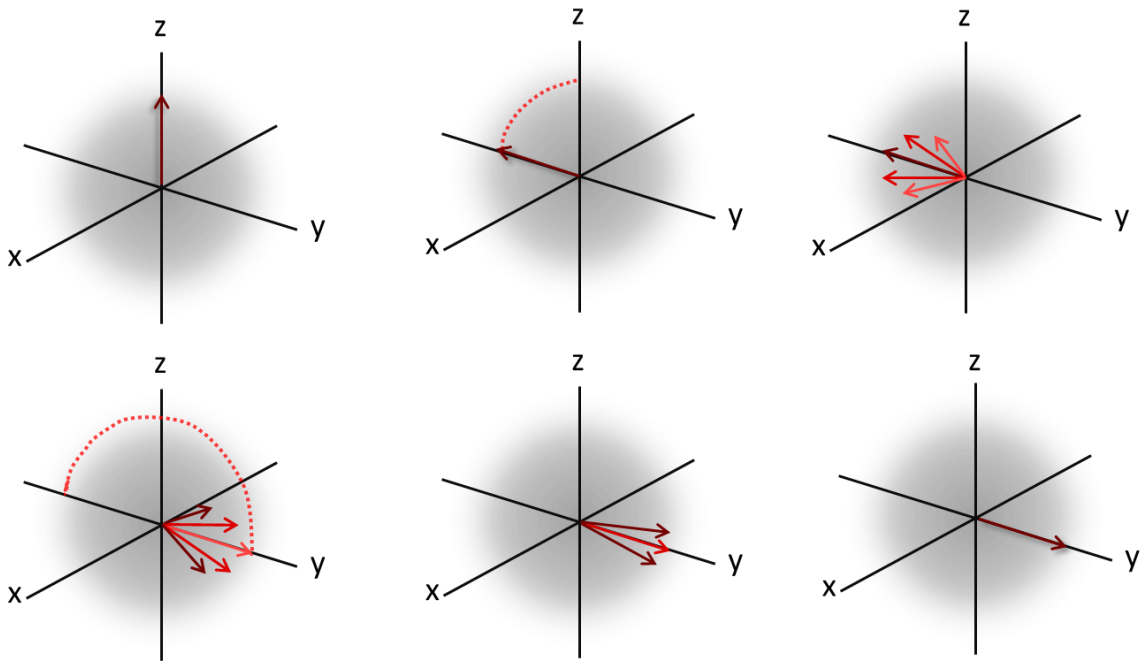

Figure 2.6 *Effects a 90°pulse on M: dephasing of the spins (first row); effects of a 180°pulse: rephasing of the spins (second row).*

2.3.4 NMR Relaxation in porous media

Relaxation processes of ^{1}H fluids in porous media are important to determine a series of petrophysical properties such as porosity, permeability, viscosity, etc. For this reason, since the 50s, applications of NMR techniques on porous media were thought for the hydrocarbons industry. Although both T_1 and T_2 are important measurements in porous media, especially in modern devices of well-logging the convenience of the more rapid

T_2 has taken precedence. Unfortunately much of the early laboratory measurements, especially in petrophysical applications, were done on T_1 since it avoided the difficulties of having a gradient-free magnetic field.

Local magnetic fields at the surfaces of the rock grains are major factor in the determination of the effective T_1 and T_2 for fluids in porous formations. If confined in porous media, relaxation is often controlled by solid-fluid interactions at the surfaces of the pore space. Water molecules diffuse and eventually reach a pore wall surface where there is a finite probability that their spins are relaxed due to interactions with fixed spins, paramagnetic ions or paramagnetic crystal defects. Further transversal relaxation occurs via diffusion in local field gradients (Bayer et al., 2010). The quantity governing the interaction is the fluid diffusion length ($\sqrt{6Dt}$) and its relation to the pore size. T_1 and T_2 of confined fluids were much shorter than those of bulk fluid.

The conclusion is that the faster relaxation of the water protons must be related to the enhanced relaxation at the pore walls since the water not altered by impurities.

Brownian motion allows liquid molecules to diffuse relatively large distances during the course of NMR measurements which are on the order of a second. The distance can be estimated from the definition of diffusion, which states that the mean square distance travelled in time *t*, is proportional to the product of the diffusion coefficient (*D*) and time:

$$\left\langle x^2 \right\rangle = 6Dt \tag{2.11}$$

Since the molecular diffusion coefficient of water at room temperature is 2×10^{-5} cm^2/s, a molecule can diffuse about 100 microns in a second. For many porous rocks this is much larger than the average dimensions of a pore. This means that the molecule can have many opportunities for approaching or striking the pore wall during a measurement period. Either the spin will realign with the imposed field (a T_1 process) or the spin will be irreversibly dephased (a T_2 process). However there may be several

collisions before a relaxation occurs. The ability of a surface to relax the spin is called the "relaxivity" or surface relaxivity coefficient, ρ (Ellis & Singer, 2008).

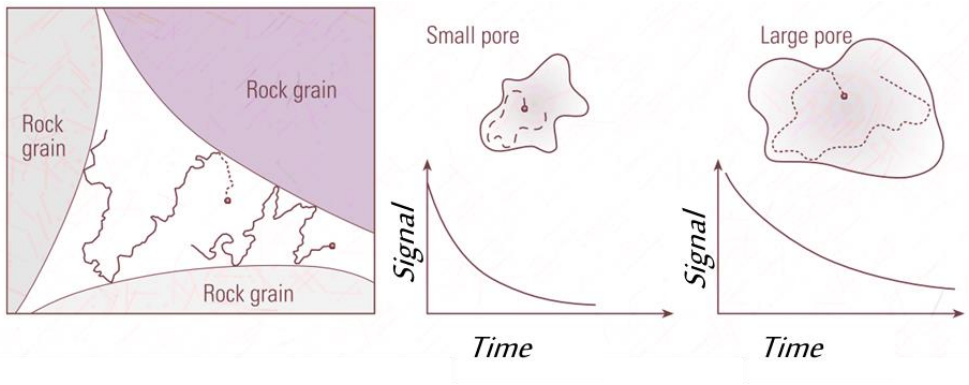

Figure 2.7 *Adapted from Ellis and Singer (2008). Schematization of proton relaxation inside pores (left). Signal from a small and a large pore (right).*

The total relaxation rate ($1/T_{1,2}$) is, therefore, the sum of bulk relaxation (B) and surface relaxation (S) and, for T_2, of relaxation due to diffusion in field gradients (diff-FG):

$$\left(\frac{1}{T_1}\right)_{total} = \left(\frac{1}{T_1}\right)_B + \left(\frac{1}{T_1}\right)_S \tag{2.12}$$

$$\left(\frac{1}{T_2}\right)_{total} = \left(\frac{1}{T_2}\right)_B + \left(\frac{1}{T_2}\right)_S + \left(\frac{1}{T_2}\right)_{diff-FG} \tag{2.13}$$

The surface relaxation term contains information of the pore system and is, therefore, further analysed. Relaxation time at the surface is determined by the residence time of the spin at the surface. The longer the residence time the higher the probability for interaction with the surface and, therefore, to relaxation. As long as this surface relaxation is slower than the transport of unrelaxed spins to the surface the fast-diffusion or surface-limited regime is fulfilled. Water molecules can pass through the pore several times before being relaxed and the magnetization decay in an individual

pore is, therefore, spatially uniform and depends on the surface-to-volume ratio. Surface relaxation is then related to the internal surface area *S*, internal pore volume *V* and the surface relaxivity which, as already said, is strongly influenced by paramagnetic ions, like Mn^{2+} or Fe^{3}, present on the surface.

Surface limited: $$\frac{1}{T_{1,2S}} = \rho \frac{S}{V} \approx \rho_{1,2} \frac{\alpha}{r} \quad (2.14)$$

where *r* is the pore radius and α is the shape factor (1, 2, 3 for planar, cylindrical and spherical pore geometry). If, in contrast, the magnetic decay is controlled by the transport of the molecules to the surface the conditions of the slow-diffusion or diffusion-limited regime is met. This may be the case if pores are large or surface relaxation is strong, e.g., due to the presence of effective paramagnetic centres.

Diffusion limited: $$\frac{1}{T_{1S}} = \frac{1}{T_{2S}} = D \frac{c}{r^2} \quad (2.15)$$

where *D* is the diffusion coefficient and *c* is a shape-dependent factor. Note that in the case of diffusion limitation T_{1S} and T_{2S} are equal. Relaxation times in the diffusion-limited regime depend on temperature in the same way as the diffusion coefficient. In this case, relaxation times are not spatially uniform, which results in a multiexponential magnetic decay, even within a single pore, and relaxation is additionally dependent on pore shape (Bayer et al., 2010).

In the fast diffusion limit the decay of magnetization (either T_1 or T_2), from a single pore, should exhibit a single exponential. As expected, real rocks show a slightly more complicated behaviour, which is multi-exponential. The distribution of the values of the components is related to the granular nature of the sample, hence to the pore size distribution. If the decay distribution times is viewed as a distribution of pore sizes, then

there is an important set of assumption: each pore is in the fast diffusion limit, the relaxing properties of the walls of all the pores are the same.

Studies (a full explanation could be find in Dunn et al., 2000) demonstrated that there is a connection between pore size, or rather the surface-to-volume ratio, and the T_1 or T_2 distributions. To get an actual pore size distribution, a surface relaxivity needs to be assigned and some model of the geometry needs to be assumed. If a certain geometry is assumed and the surface relaxivity is constant (usual assumption), then there will be a relation between the pore size distribution and the T_1 and T_2 distributions, since the latter depend on the surface to volume ratio. Assuming a certain geometry also is equivalent to establishing a connection between a measure of the pore size and the S/V ratio. Further NMR petrophysical applications depend on a correlation between pore body size and pore throat dimension which is frequently the case for sandstones.

The enhancement of the T_2 decay can be due to the additional dephasing of spins due to their diffusional displacement in a magnetic field with a gradient. The actual analytical form predicts a magnitude that depends on the diffusion coefficient. This predicted decay rate was derived for unhindered motion of the polarized molecules. For the case of, say, water molecules confined to a small pore in a porous rock, the diffusion might not be unhindered. Depending on the size of the pore and the magnitude of the self-diffusion coefficient, the molecule may be prevented from reaching its predicted mean squared displacement. In fact, for a saturated rock sample in the fast diffusion limit, it is expected that the molecules will encounter the grain surfaces a number of times during an echo spacing.

This can be exploited experimentally using a pulsed gradient spectrometer, where a gradient is actually applied to the magnetic field to enhance this effect, which can appear as a time-dependence of the self-diffusion coefficient. At very early time, D has the value expected for the unconfined fluid; its apparent value will be seen to decline as time increases and can be construed as a measure of the pore size and tortuosity. With the development of gradient tools coupled with sophisticated pulsing and signal-

processing tools, D and T_2 can be measured simultaneously. These measurements add a second dimension to the traditional measurements and will be very useful for determining fluid properties and perhaps wettability. The interpretation of these data may require consideration on pore system diffusion restriction (Ellis & Singer, 2008).

2.3.5 Paramagnetic impurities

Paramagnetic systems contain one or more unpaired electrons and have therefore a positive magnetic susceptibility. The more studied paramagnetic systems usually contain either free radicals or transition metal complexes in solution. The unpaired electron spins interact with nuclear spins and influence NMR spectra of liquids. Both relaxation times are greatly reduced in the presence of paramagnetic ions. The strength of the effect depends on the ion environment and specification and it is called paramagnetic relaxation enhancement. Its most palpable effect is a more or less marked broadening of the NMR resonance lines. In porous media, the paramagnetic relaxation enhancement, influences the process of relaxation inside the pore volume: when there are ions at the surface such as Mn^{2+} and Fe^{3+}, the relaxivity can strongly change. So for a quantitative estimation of pore-size distribution, the surface relaxivity of the solid must be known, which is specific for every solid fluid combination. Furthermore, surface relaxivity must be determined experimentally by comparing NMR relaxation measurements with surface-to-volume measurements using additional techniques such as optical or electron microscopy, mercury porosimetry, capillary pressure or adsorption isotherms (for example nitrogen adsorption) (Jaeger et al., 2009).

The effect of paramagnetic substances on the relaxation rate can be much stronger when they are adsorbed to the solid surface, due to the restricted molecular motion of the adsorbed species which in turn results in a longer rotational correlation time for the coordinated water molecules (Bayer et al., 2010). Nevertheless, bulk relaxation is also

accelerated in the presence of dissolved paramagnetic ions. This relaxation acceleration in the bulk solution is dependent on the speciation of the ion. Concluding, the acceleration of the bulk relaxation rate in comparison to pure water may give additional information on the ion environment in complex soil solutions (Bayer et al. 2010). An example of this situation is when soils saturated with water are studied: the paramagnetic ions in solution change relaxation times, and the interact with organic components (Bayer et al. 2010).

2.3.6 NMR Relaxation in biological systems

NMR applications on biological systems are at now probably more famous than those on porous media. This is largely due to the successful employment, especially of MRI, to the biomedical sciences.

Going deeper in the explanation, it is useful to speak in terms of molecular motions. For this reason the τ_C correlation time, should be defined as the average time between molecular collisions for a molecule in some state of motion, and relaxation times are related to it.

As can be deduced by Figure 2.8 everything that modifies the thermal molecular motion, as for example the temperature, the viscosity, …, it will induce a variation in the relaxation times.

The BPP (Bloch Purcell Pound) theory that gives the specific plot of Figure 2.8, describes relaxation via magnetic dipole-dipole interactions (typically dominant process in liquids and tissues). It tries to explain the relaxation constant of a pure substance in correspondence with its state, taking into account the effect of tumbling motion of molecules on the local magnetic field disturbance. The theory makes the assumption that the relaxation is proportional to $e^{-\frac{t}{\tau_c}}$. Observing the plot of Figure 2.8 (left), it is possible to understand that from solids to liquids (increasing molecular motion) we obtain different relaxation times. If for solids T_1 and T_2 are very different, for a liquid

they become almost equal. The theory is accurate for bulk water, but not for complicated systems such as, for example, the human body. Biological systems in general are complex systems, because sum of different components, with different molecular motion. Anyway the T_1 and T_2 study approach give solid results, especially when different biological species are studied separately.

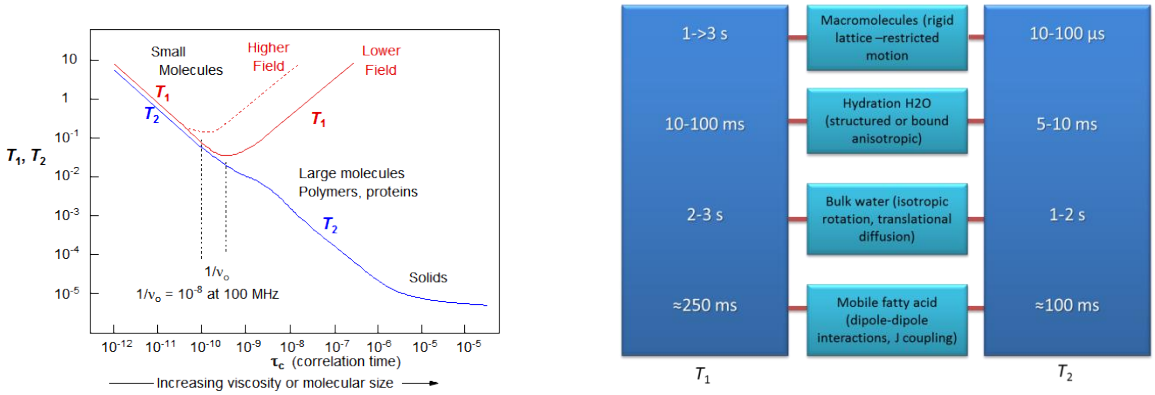

Figure 2.8 *Representation of relaxation times (s) vs the correlation time (s) (left); a summary of the principal molecules with their relaxation times.*

NMR techniques span the whole range of biological systems. These include: structure determination of large biological molecules, understanding biochemistry and functional behaviour of proteins and nucleic acid; cell metabolism; structure and function of tissues: imaging, metabolism and function of whole organs; pharmacology; plants and agricultural sciences and several other areas of life sciences. The application of the ^{1}H NMR to complex systems as biological tissues, is mainly due to the large abundance of water inside them. Broadly speaking, one can say that the cellular metabolism is strictly related to the water content. Furthermore not all the water of a biological system has only one physical or biological function. NMR can explain the different water roles; for example the measurements of relaxation times give information on the molecular motions, as relaxation phenomena are strictly related to the fluctuations of the local magnetic field caused by rotation and translation of the molecules.

Furthermore NMR can be applied to a wide range of liquid and solid matrices without altering the sample or producing hazardous wastes. Nowadays also food engineering, food processing and waste management are fields interested in applying innovative technologies able to detect the structure and the processes of the biological system.

It is interesting, for example, to cite the example of food. Many foods are proton-rich, with protons originating, e.g., from water, fat, carbohydrates, and proteins ^{1}H NMR becomes the most common type of NMR to determine these abundant food components. These components are essential for human nutrition and also they influence the intrinsic properties of food during processing, storage, and transportation (Marcone et al., 2013).

2.5 NMR Imaging

2.5.1 The principles of images reconstruction

It follows a brief explanation of imaging methods, only to give idea of what is an image reconstruction in MRI.

With MRI is possible to determine the spatial distribution of a given component within the sample. Since nuclei process at different rates in locations where the magnetic field has changed, the position of the spins can be determined from frequency content of the resulting MRI signal. Furthermore the signal is the Fourier Transform (FT) of the spin density. The coverage of k-space, that will be later defined, is pivotal to reconstruct an image of a sample by the inverse FT techniques.

The signal can be represented as:

$$S(k_x) = \int_{-\infty}^{+\infty} \rho(x) e^{jk_x x} dx \qquad (2.16)$$

If the Fourier transform in known, the $\rho(x)$, which represents the spin density, is given by the inverse FT:

$$\rho(x) = \frac{1}{2\pi} \int_{-\infty}^{+\infty} S(k_x) e^{jk_x x} dk_x \tag{2.17}$$

This is a one-dimensional example, with the choice of a x direction, but other directions could be chosen.

It is impossible to obtain $S(k_x)$ as a function of continuous k_x. Instead $S(k_x)$ is measured only at a finite number of sampling points. To demonstrate how discrete samples of the signal can be used for image reconstruction, let's assume that $S(k_x)$ is measured at N locations:

$$k_x = 2\pi n / L_x \tag{2.18}$$

Where $-N/2 \leq n < N/2$, and N is assumed to be even; L_x is a positive constant, known as field-of-view (FOV), which defines the size of the imaged region.

By substitution, it is possible to define the reconstructed image intensity, I, as the inverse discrete FT of the signal:

$$I(p) = (1/N) \sum_{n=-N/2}^{n=(N/2)-1} S(n) e^{-j2\pi np/N} \tag{2.19}$$

Where $-N/2 \leq p < N/2$. Since $S(n)=S(k_x(n))$, substituting $S(n)$ with the complete expression of $S(k_x(n))$, it is possible to obtain the relationship between the spin density and its image:

$$I(p) = \int_{-\infty}^{\infty} \rho(x)\, PSF\left(x - x_p\right) dx \tag{2.20}$$

Where $x_p = pL_x / N$ and $PSF(x) = \dfrac{e^{-j\pi x/L_x} \sin\left(\pi N x / L_x\right)}{N \sin\left(\pi x / L_x\right)}$ (2.21)

It follows that the image intensity is given by the convolution of the $\rho(x)$ and $PSF(x)$, known as point-spread function, where $PSF(x)$ represents the image of a point source described by the Dirac delta function.

These results can be generalized to describe Fourier reconstruction from discrete samples in two or three dimensions.

Image intensity is the sum of weighted elements $\rho(x)dx$ with $PSF(x)$ as the weighting function. Furthermore, spatial resolution is the minimum distance between two points in an object at which they can still be distinguished from another in the image. δx can be defined as the effective width of a point-spread function:

$$\delta x = \frac{1}{PSF(0)} \int_{-L/2}^{L/2} PSF(x) dx \tag{2.22}$$

Using *PSF* definition:

$$\delta x = L_x / N \tag{2.23}$$

PSF oscillates such that its maximum at the origin $x=0$ and rapidly decreases with increasing distance from the origin.

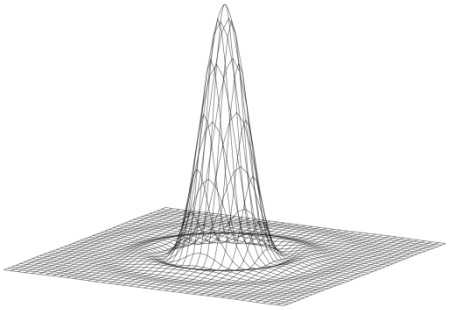

Figure 2.9 *Point spread function representation.*

Since *PSF* is a periodical function with period L_x, the reconstructed image intensity $I(p)$ is defined by a sum of the equally weighted object intensities at:

$$x = \frac{pL_x}{N} + mL_x \text{ where } m = 0, \pm 1, \pm 2, \ldots \tag{2.24}$$

This phenomenon, aliasing, results from discrete sampling of $S(k)$ and in general prevents complete recovery of $f(x)$. However, under the circumstances typical for MR imaging the object has a limited spatial extent such that:

$$\begin{cases} |f(x)| \geq 0 \Rightarrow -a/2 \leq x \leq a/2 \\ |f(x)| = 0 \Rightarrow otherwise \end{cases} \tag{2.25}$$

Aliasing can be fully recovered by satisfying the Nyquist criterion for the sampling interval Δk:

$$\Delta k \leq \frac{2\pi}{a} \tag{2.26}$$

It follows that in order to prevent aliasing the selected FOV L_x should be equal to or greater than the length of the object, a.

2.5.2 K-space

It is most useful to formulate imaging arguments in terms of image and data space. The inverse FT implies that the spin density can be reconstructed from the signal, if the latter is collected over a sufficiently large set of k values.

Spatial position is encoded in the reciprocal k-space signal *I*(*k*) and the image amplitude is obtained from the FT of *I*(*k*); k-space is therefore the Fourier inverse of real space. The variation of the angular frequency if the spins is defined by:

$$\omega(r) = -(\gamma B_0 + \gamma g \cdot r) \tag{2.27}$$

which is related to the applied magnetic field gradient vector g (in the laboratory reference frame), and it is written as 3D extension.

When k-space data are acquired on resonance in the rotating frame, the voxel intensity is obtained by the 3D FT of *I*(*k*) such that:

$$I(r) = \iiint I(k) \exp[+j2\pi k \cdot r] dk \tag{2.28}$$

(Mitchell et al., 2014)

2.5.3 Frequency and phase encoding

In practice MRI is most frequently performed by using a sequence of pulsed magnetic field gradients which are applied during a FID or a SE to ensure that the signal is given by FT of the transverse magnetization in the sample. At this stage two basic imaging techniques for Fourier encoding must be described: frequency and phase encoding.

Frequency encoding is implemented by acquiring signal in the presence of an external magnetic field gradient, whose purpose is to make the Larmor frequency of nuclei spatially dependent during signal acquisition.

The signal acquired is composed of components with frequencies from a narrow range, known as the signal bandwidth, around the Larmor frequency ω_0 at the centre of the FOV.

Two-dimensional spatial encoding is achieved using an additional gradient, the phase-encoding gradient, which is perpendicular to the frequency-encoding gradient.

As a result of the frequency and phase encoding the NMR signal in a two-dimensional case is given by 2D Fourier transform of the magnetization:

$$S = \iint M_{xy}(x,y)\, e^{jk_x(n)x + j\phi(y)} dxdy = \iint M_{xy}(x,y)\, e^{jk_x(n)x + jk_y y} dxdy \qquad (2.29)$$

Where: $k_x(n) = \gamma G_0 \tau_w n$ and $k_y = \gamma \int_t^{t+t_{ph}} G_y dt$; with τ_w, dwell time equal to the ratio between the acquisition time and the number of samples.

Phase encoding requires repetitive excitations of the transverse magnetization in the sample in order to collect signals at different values of k_y. In the initially proposed phase-encoding scheme, changes in k_y were achieved by varying the duration of the phase encoding gradient while keeping its strength constant. A more common approach is to vary the strength of the phase-encoding gradient in a step-like fashion.

In this case the signal obtained with frequency and phase encoding can be written as:

$$S(n,m) = \iint M_{xy}(x,y)\, e^{jk_x(n)x + jk_y(m)y} dxdy \qquad (2.30)$$

Where $k_x(n) = \gamma G_{0,x} \tau_w n$ and $k_y(m) = \gamma G_{0,y} t_{ph} m$; with t_{ph}, duration of the gradient.

After all phase encodings are implemented, image reconstruction is performed by computing the inverse discrete FT of $S(n,m)$. Using the previous results we find that the reconstructed image intensity is given by the convolution of the transverse magnetization in the sample and a two dimensional *PSF*. The resultant spatial resolution in the x-y plane is $(L_x/N)\times(L_y/M)$.

Note that the reconstructed image intensity is a complex quantity which can be written in polar form $Ie^{j\theta}$, where I is the amplitude of the intensity and θ is the phase of the intensity. It is the amplitude of the intensity which is normally used to display MR images (often referred as magnitude images) while the phase information is neglected. The useful interpretation of the signal acquisition in Fourier MRI as sampling along trajectories, in a spatial frequency space, is the k-space. In 2D imaging one of the components of $\boldsymbol{k}$ produced by the phase-encoding gradient is constant during acquisition, whereas another component produced by the readout gradient changes linearly with time. The corresponding trajectories in k-space are reproduced by a number of parallel lines.

The signal amplitude at low spatial frequencies in the central region of k-space is typically much higher than the signal amplitude at high spatial frequencies on the periphery of k-space. In general, low spatial frequencies are needed to reconstruct the bulk of the object, and high spatial frequencies are required to accurately reproduce rapid spatial variations in the object (e.g. sharp edges).

2.5.4 Contrast in MRI

Variations in the local relaxation times T_1 and T_2, and the amount of hydrogen nuclei per unit volume (named proton density) are the predominant sources of contrast in proton MRI. The intensity of the signal in various zones of the sample may be directly proportional, for example, to water molecule content. This images, called proton

density weighted images are produced using short echo time $TE < T_2$ and long repetition time $TR > T_1$ in order to reduce T_1 and T_2 modulations of the signal.

On the other side, images can be weighted on the basis of the relaxation mechanisms. The T_1-weighted images are generally acquired with $TE < T_2$ of the sample in order to reduce T_2 modulation of the signal. T_1 contrast between components with close T_1 values diminishes at either very short $TR \ll T_1$ or very long $TR \gg T_1$, whereas the maximum contrast is achieved at the intermediate $TR \approx T_1$.

On the other side, the T_2 weighted images are acquired with TE approximately equal to or longer than the shortest T_2 in component of interest, and with long repetition time ($TR > T_1$) needed to reduce T_1 modulation of the signal.

2.5.5 Spin Echo sequence

The Spin Echo sequence for imaging could be represented as in Figure 2.10.

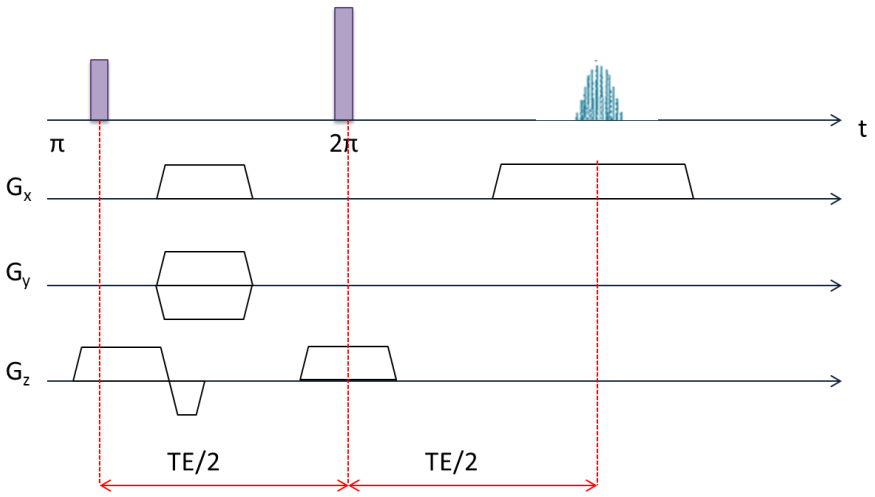

Figure 2.10 MRI *spin echo sequence.*

This sequence adopts a spin echo refocusing by means of 180° pulse that causes the formation of a spin echo during signal acquisition. For this reason spin-echo imaging is generally less sensitive to the presence of magnetic field inhomogeneities. The intensity

of a spin echo image is proportional to e^{-TE/T_2}, where *TE* is the time between the excitation pulse and the formed echo (Kuperman, 2000).

2.5.6 Saturation recovery sequence

Saturation recovery is not so frequently adopted in MRI, but the repetition of this measure at different inversion time is useful to represent the entire curve of the T_1 relaxation, as it will be explained in the next section.

2.5.7 Quantitative Relaxation Tomography (QRT) technique

MRI and relaxation analysis are combined in a spatially resolved technique named quantitative relaxation tomography (QRT), which is able, for example, to quantify the parameters connected to the local structure in the internal regions of a porous material saturated by water, giving information on the pore space structure beyond the nominal instrumental resolution. Voxel-by-voxel T_1 and T_2 relaxation curves are acquired in order to obtain T_1 and T_2 maps. QRT permits to obtain images of pure T_1 and T_2 or on the intensity of magnetization. QRT permits for example the evaluation of the porosity (ratio of pore space to total volume), at different length scales, from the sample to the voxel, not all achievable by traditional methods. Applications in biological samples is more evident, as it permits to obtain local information of the components, both on structure and on water mobility.

QRT requires the acquisition of a series of images, both using SE or SR, if T_2 or T_1 are respectively investigated, that are later fitted to obtain one image which represents for every sample components their specific relaxation time.

For example, if one need to achieve a T_2 map, *n* SE sequences are performed with increasing *TE*. Then images are processed and voxel by voxel, the signal intensities obtained at variable TE are fitted to the function:

$$S(TE) = S(0)e^{-\frac{TE}{T_2}} + c \tag{2.31}$$

Where c is the offset to get the extrapolated total equilibrium magnetization $S(0)$.

The assumption implies the approximation of single-exponential decay of the transverse and longitudinal components of the magnetization in each voxel.

In a similar way T_1 maps, obtained with increasing inversion times, is described by the function:

$$S(t) = S(\infty)\left[1 - c_1 e^{-\frac{t}{T_1}}\right] e^{-\frac{TE}{T_2}} + c_2 \tag{2.32}$$

Where c_1 and c_2 are constants, $S(\infty)$ is the total equilibrium magnetization to be compared with $S(0)$, and T_1 is the longitudinal relaxation time to be determined.

The elaboration of data of is obtained using the in-house software program ARTS (as described in the next chapter), written in C++, which fits experimental data of each voxel by an algorithm based on the Levenberg–Marquardt nonlinear least-squares minimization method with four free parameters, with the T_1 computation using in addition the T_2 value from the T_2 computation, if available.

Chapter 3

NMR equipment: hardware and software optimization for measurements on organic waste

3.1 New hardware and software releases

As already explained in the Chapter 1 it has been necessary to adapt the experimental equipment of the NMR laboratory to improve its efficiency and its compatibility towards the study of organic waste. In this chapter the new releases of hardware and software tools will be discussed as the results of a first part of this research thesis. It is important to describe these new tools because they will be integral part of the experiments, shown in the next chapters, where real organic waste samples and similar are examined by NMR techniques.

The discussion of this chapter will include the description of the whole experimental equipment with a detailed attention on the new elements realized, both on the hardware and on software. In particular the new coils configuration and tuning, the creation of new software for acquisition and pre, post-processing tools.

3.2 Hardware optimization

3.2.1 The NMR permanent magnet of the laboratory

The NMR LAGIRN laboratory is equipped with a permanent magnet, part of an ARTOSCAN (ESAOTE S.p.a., Genova, Italy) tomograph. This magnet was designed for musculoskeletal imaging, so it has a hole in centre of the magnet where originally patients could insert their articulations for a NMR examination. The dimensions of the permanent magnet are optimal for the study of the samples of dimensions required, for significance, by the petro-physical research field. In fact the magnet can host RF coils up to 13 cm in diameter, which is, for example, about the diameter of log cores (Figures 3.1).

It is a permanent ferrite magnet of 965 kg of weight with a field strength of about 0.2 T, classified as a low field (Figure 3.2), as discussed in the previous chapter.

The magnet can both work with the tomograph (Figures 3.1.a) and with the relaxometer, which is composed of an analogical console (Stelar S.p.a., Mede, Italy) and a laptop which commands the console (Figures 3.1.b).

The NMR equipment works at 30℃ of temperature, which is maintained thanks to a thermic controller. The maintenance of this temperature is important in terms of frequency: strong variations in temperature involve troubles in tuning the devices. To face atmospheric conditions a conditioning system is often used to ensure a room temperature between 21 and 25℃, especially in summer time when the temperature of the lab reach higher temperatures.

Figure 3.1.a) *NMR LAGIRN lab tomograph and* b) *relaxometer. In both pictures notice the ferrite permanent magnet with the probe.*

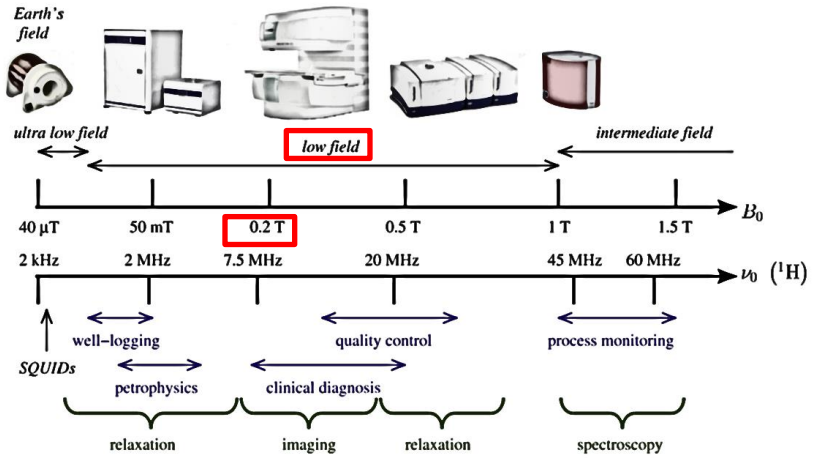

Figure 3.2 *Adapted from Mitchell et al., 2014. Some* ^{1}*H types of magnetic fields and relative NMR equipment.*

3.2.2 The dedicated NMR coils for relaxometry: new configurations and updates

A radiofrequency (RF) coil in a NMR equipment is generally a copper coil which surrounds the sample under analysis and it is hosted in the magnet that generates the static field B_0. The main function of the RF coils is to transmit the RF pulses and to receive the NMR signal. RF coils are normally designed to provide optimized signal to noise ratio and their dimensions are very important compared to the dimensions of the samples. As it is important to measure significant quantities of samples, in order to obtain reliable results on physico-chemical properties and processes, the use of an appropriate dimensioned RF coil is required.

Since, in the most cases of this research, samples were unconsolidated, the RF configuration inside the magnet was of prime importance. The NMR equipment of the lab was mainly equipped for consolidated samples (rocks, ceramic, cements,...). For example, the 1 Inch RF coil (made by Stelar S.p.a., Mede, Italy) could be placed only horizontally in the centre of the magnet. This situation was not good to arrange unconsolidated samples, since the position did not prevent sample movements, that affect NMR responses.

As the 1 Inch RF coil (which is 3 cm of height and 2,5 cm of diameter) was one of the most used for this research purposes, an intervention on its design was necessary. A special amagnetic support was built to place the coil in vertical position in the centre of the magnet (Figure 3.3).

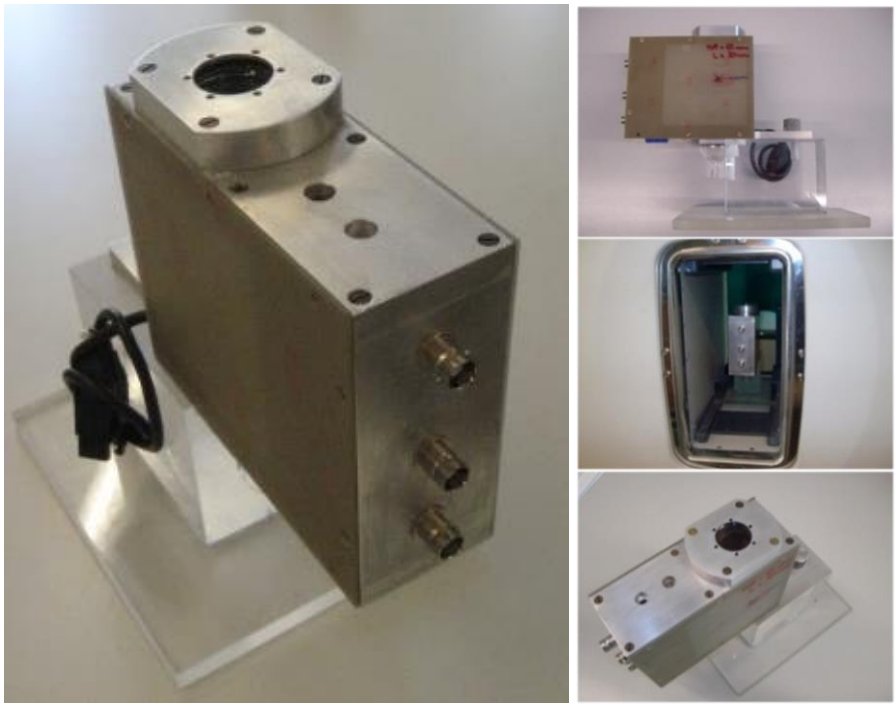

Figure 3.3 *1 Inch NMR coil for relaxation measurements. Notice the nonmagnetic PMMA support which helps the positioning inside the magnet and the maintenance of the vertical position. The support is dimensioned to place the coil in the centre of the magnet where the field is homogeneous.*

In addition to the 1 Inch RF coil other two relaxometry coils, for sample of big dimensions (Figure 3.4), respectively of 7 cm and 13 cm in diameter, are present in the lab and they have been used for these researches. No structure modifications have been necessary for these two coils. Only specials amagnetic supports have been realized to centre them in the centre of the B_0 field. All the three relaxometry coils have been specifically calibrated in order to find the best parameters such as the total attenuation (TATT) and the duration of 90˚pulse (PW90).

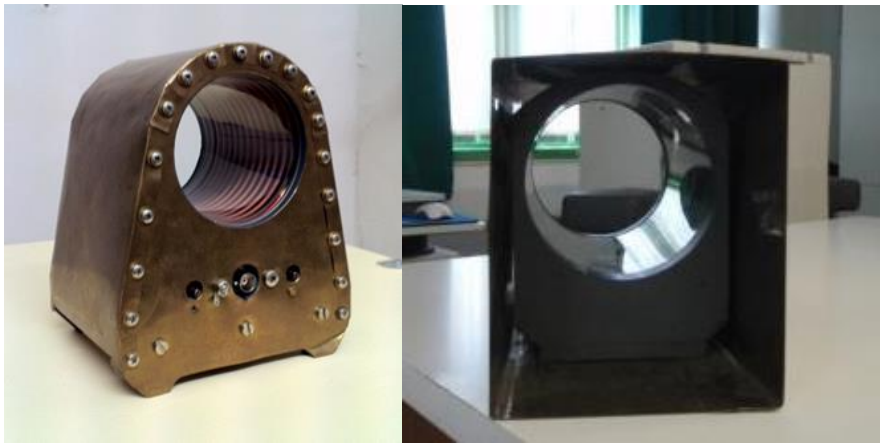

Figure 3.4 *Big dimensions coils for relaxometry.*

3.2.3 Signal-to-noise ratio problems

As in this research work the most of the samples were unconsolidated, their preparation can strongly affect the NMR results, so a procedural protocol for the same type of sample must be adopted before NMR experiments. In the following chapters for each experiments the sample preparation will be illustrated, but in this section few basic guidelines to obtain a reliable NMR measure will be described.

What is first important in a NMR measurement is the signal-to-noise ratio (SNR). Low-field NMR is considered to have an inherently poor SNR compared to experiments conducted at intermediate and high field, as SNR is proportional to ω_0, although the exact theoretical SNR owes as much as to the performance of the RF probe and to the static magnetic field (Mitchell et al., 2014). Improving the SNR in low-field conditions is not so easy if heterogeneous materials, such as porous media, dense composite materials, or any systems with gas/liquid/solid interfaces, as they are prone to the formation of internal field gradients due to the magnetic susceptibility contrasts in the sample. Strong internal gradients can lead to very rapid signal decay within the dead-time of the RF probe, preventing the detection of any signal. Capacitive coupling between the probe and the sample can lead to significant changes in the probe tuning, particularly if the sample is electrically conductive. Maximizing the coil filling factor, i.e.,

the fraction of the sensitive volume of the RF probe occupied by the sample, is also important. Due to the cylindrical geometry of solenoid RF coils, small reductions in sample radius result in a significant reduction in filling factor. It is advisable to leave some space between RF coil and sample as local B_1 ''hot spots'' will be present in close proximity to the wire (Mitchell et al., 2014). In general SNR can be improved by increasing the number of repeated scans. Then, it is a good practice to remove sources of interference whenever it is possible, the use of a simple pick-up coil, a loop of copper wire is sufficient, is recommended (Mitchell et al., 2014).

Therefore, to optimize the NMR signal that will be acquired, after an eventual pre-treatment of the sample and before starting an experiment in T_1 or T_2, in relaxometry, it is necessary to tune and match the NMR circuits and to use the S1P sequence to acquire a FID of the sample, establishing some important measurement parameters.

First of all the matching circuit of the RF coil has to match the impedance of the coil with the impedance of the receiver of the relaxometer. The circuits in NMR probes are essentially a RLC band pass filters. The properties of the band pass filter of the circuit are determined by the values of capacitance for the capacitors in the circuit and the inductance of the sample coil. One is usually able to vary the capacitance of the tuning and matching capacitors to optimize the probe for the experiment at hand. The adjustments are typically made by turning rods that extend from the bottom of the NMR probe. Changing the tuning capacitor will shift the band and it is therefore used to tune the probe exactly on the Larmor frequency. Changing the matching capacitor changes the efficiency transfer of energy of the circuit. These two capacitors are not independent and they must be adjusted iteratively to optimize the NMR probe. Proper tuning and matching are essential in getting high quality NMR results. The figure 3.5 shows the response on an oscilloscope for an NMR probe connected to a sweep generator. One can think of these plots as frequency on the horizontal axis vs efficiency on the vertical axis. The first panel shows a probe that is well matched and tuned. The

second panel shows a probe that is properly matched but poorly tuned and the third panel shows a probe that is properly tuned but poorly matched (www.nmr.uottawa.ca).

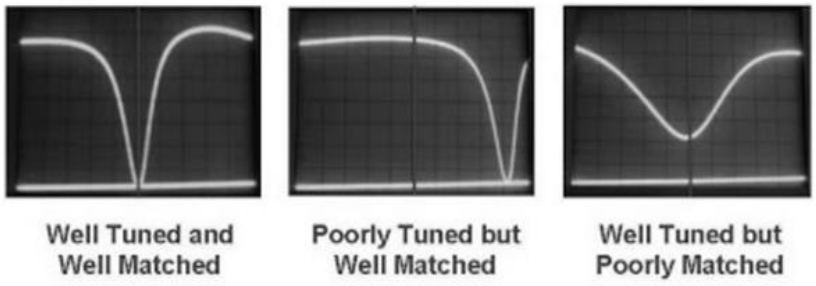

Figure 3.5 *Example of responses of the tuning and matching circuits.*

Any NMR instrument which uses the same coil to both excite the nuclei and to detect the subsequent FID is subject to artefacts due to imperfect separation between the high-power excitation electronic branch (gated transmitter) and the low-power signal-detection branch (preamplifier and gated receiver) which meet at the coil terminals.
The basic transmitter-receiver separation consists in the fact that the two devices never operate simultaneously - the sample is first excited by a very brief but powerful RF pulse and only afterwards starts the acquisition of the much longer lasting but very weak FID signal. Even so, however, one must face several problems. First of all, one must protect the preamplifier from being damaged during the high-voltage pulse. Second, no matter how good such a protection might be, it is never perfect and the preamp needs some time to recover from overload during the pulse. Third, the probe circuitry is a tuned circuit and reacts to the pulse by a ringing tail which has nothing to do with the NMR signal. The result is that for some time after the pulse, the detected signal is heavily distorted and/or contains pulse-ringing artefacts. The duration of the interval during which the receiver is "blinded" is called dead-time. The dead-time gives rise to a number of characteristic, pesky artefacts in the acquired data. It is therefore always desirable to reduce it as much as possible (Sykora; www.ebyte.it).

This is important especially when samples have short relaxation behaviours, in this cases a good choice of the dead-time is necessary to obtain as much information as possible from the signal.

3.2.4 An home-made bio-reactor device for NMR measurements

Not only NMR coils were adapted for organic waste measurements, but also new laboratory devices to contain waste samples were created.

This is the case of the bio-reactor, completely amagnetic, created to host samples which experiment biodegradation (e.g. compost samples). This simply, but efficient, reactor is made of transparent PVC, with dimensions adapted for the coils of large dimensions (13 cm in diameter). The transparent plastic has the advantage to make the sample visible, to control the process in course. It has holes to permit oxygenation and hence, aerobic reactions; furthermore it has special support to ensure the same position in all consecutive NMR measurements, since, especially for MRI, this method is important for the acquisition of the same slice every time. A similar reactor has been created for routine measurements such as temperature detection.

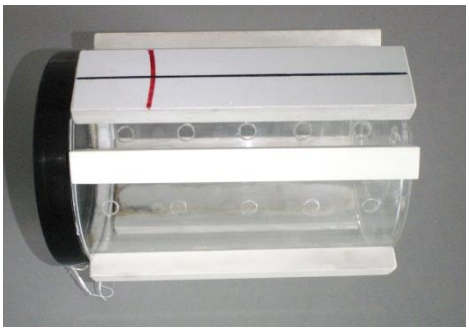

Figure 3.6 *NMR bio-rector for organic waste samples.*

3.3 Software optimization

An NMR experiment, by the software point of view, is organised on the basis of different steps (Figure 3.7). For each one, most probably, a different software is used on the basis of the stage of the experiment. Approximately pulse scheduling, signal acquisition, signal pre-processing, signal inversion and signal post-processing are the main phases of NMR investigation, and they are all supervised via software.

To optimize the set-up for the measurements of organic waste samples, it has been necessary to operate using specific created software, on three stages of the experiment (see Figure 3.7 to notice the new software realized):

- A software to generate the optimal LAPSRSE sequence: GenLapsrSE.exe;
- Optimize the use of a pre-inversion software: Field Cycling;
- A software to further process data after inversion: FiltroDAT.exe.

The pulse scheduling is still managed by the "AcqNMR" software, which is from Stelar S.p.a. and the inversion is done by the home-made software "UpenWin" (Bortolotti et al., 2009).

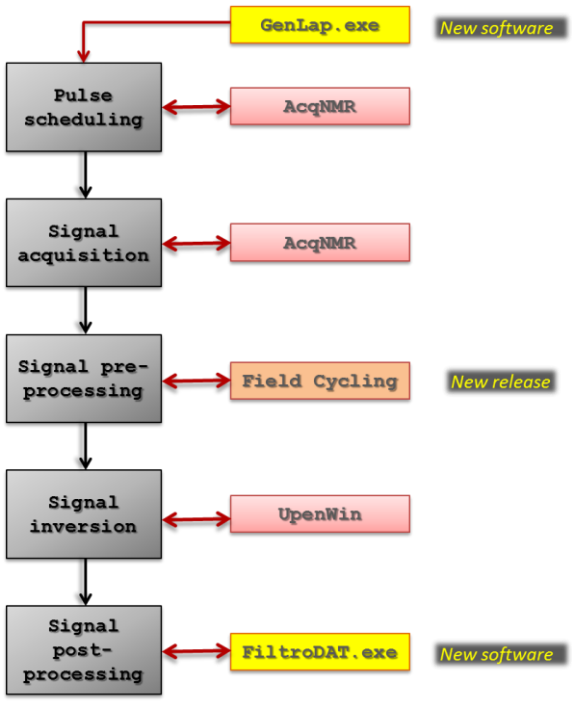

Figure 3.7 *Software steps in a low-field NMR experiment, adapted for NMR LAGIRN equipment.*

For clearly, it is helpful to specify that the "AcqNMR" software permits to lead the NMR experiment. By means of an interface, it is possible to choose the sequence and to insert all the sequence parameters (repetition time, time of echo, 90° pulse duration, attenuation of the signal, number of scans, number of blocks, etc, see appendix A). After the upload of the complete sequence, it is possible to start the experiment. The signal acquired during the NMR experiment is visualized in real time on the "AcqNMR" interface. At the end data can be saved in file format with extension ".sdf". The sequences are external script files that are uploaded in the "AcqNMR" software. So the user can eventually create its own sequence, on the basis of the need of the sample analysed, that is what it has been done in this research thesis, and that it will be discussed in the following paragraphs. For further details on AcqNMR parameters see Appendix A.

3.3.1 The creation of a dedicated NMR sequence: the Logarithmic A-Periodic Saturation Recovery Spin Echo (LAPSRSE) sequence

In many applications on consolidated systems, e.g. rocks, the relaxation times usually measured is the T_2, because a transverse relaxation measurement is not as time consuming as a longitudinal relaxation measurement, although T_1 may be the more appropriate measure than T_2 in many cases. Furthermore the spin-lattice relaxation data are usually acquired using the traditional IR sequence, which is very time consuming, since it requires the return to the thermal equilibrium of the magnetization before each repeated scan. Moreover it does not work properly in situations in which sever instrumental imperfections combines with sample complexity. If the duration of the inversion RF pulse, the 180° pulse, is comparable with the FID duration, the efficiency of the inversion is very poor. This happens for example, when there is the presence of intense paramagnetic impurities. A possible alternative is to use SR, which is faster and it doesn't need any inversion pulse. Actually when one chooses to operate

without gradient spoiler pulses, that enable SR to work properly, a good solution is to use a magnetization suppression pulse sequence. The family of sample magnetization sequences, which includes the aperiodic saturation recovery and the logarithmic aperiodic saturation recovery, aims to suppress as fast as possible the nuclear magnetization of all components of a sample. In particular, attention is being paid to samples with extremely wide distributions of relaxation times, offsets, and nutation angle (B_1 inhomogeneity).

The creation of the LAPSRSE (Figure 3.8), which is an extension of well-tested sequence logarithmically distributed a-periodic saturation recovery, permits to obtain the spin-lattice relaxation data, by means of a sequence of pulses to suppress the magnetization of the sample and allows a fast and efficient pre-saturation in the presence of a wide spread of offsets, relaxation rates, and magnetic field imperfections. In order to reduce the instrumental dead time limitation, LAPSRSE adopts an echo signal detection. In practice the result of a T_1 experiment is a collection of digitized and recorded echoes signals, as it is a multi-block sequence: a number of echoes can be acquired from a first time, just greater than the dead time of the relaxometer, to a four times the T_1 maximum of the sample.

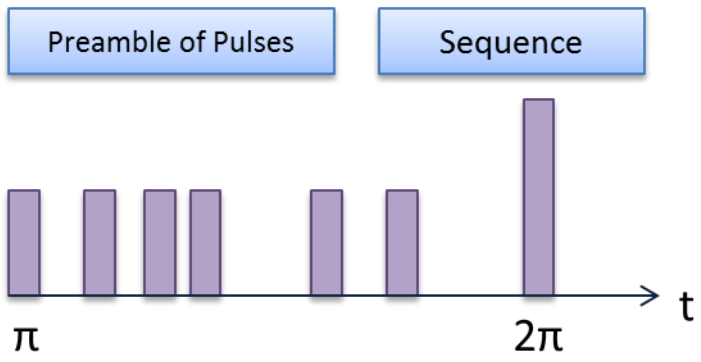

Figure 3.8 *Schematization of sequence with a preamble of pulses*

Furthermore every sample has its specific relaxation times distribution, so the preamble pulses of the LAPSRSE sequence must be logarithmically spaced in the time on the basis of the time distributions. For this reason a dedicated software was created to generate the inversion pulses, with the possibility to choose the number, the initial time and the final time.

3.3.2 The LAPSRSE generator software

The software "GenLapsrSE" (Figure 3.9) has been created as a generator of the script, an ASCII file with extension .ssf, of the LAPSRSE sequence, which is used by the "AcqNMR" software of the relaxometer to manage the whole sequence. As before mentioned the need of the use of a LAPSRSE generator is due to the fact that the LAPSRSE sequence has a preamble of pulses logarithmically distributed, whose total time has to be comparable with the relaxation times of the samples. For this reason each sample requires potentially its own LAPSRSE sequence.

The software permits to insert in input the minimum T_1, the maximum T_1 in milliseconds, the number of pulses to use in the preamble, which can be logarithmically or linearly distributed and the pulse to be used.

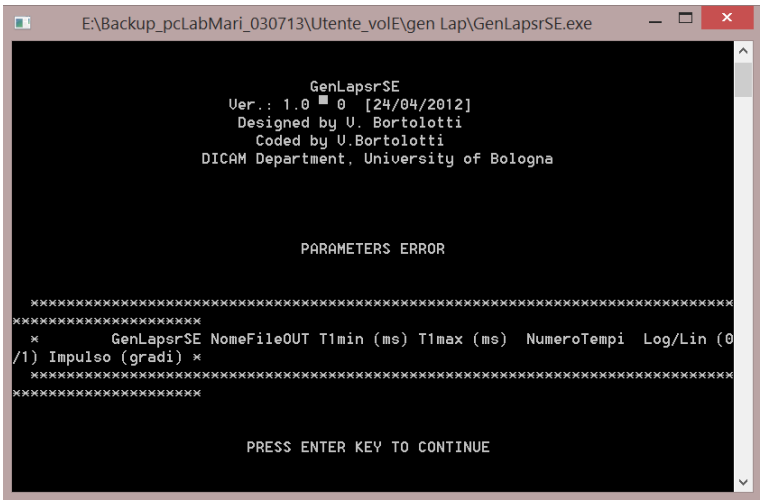

Figure 3.9 *"GenLapsrSE" screenshot.*

Shown below there is an example of the output file .ssf generated by the software. Ten pulses have been set, logarithmically distributed from a minimum T_1 and a maximum T_1. To obtain a more efficient magnetization inversion, the pulse has been set at 99°.

```
STELAR Script File

============================================================
==================================================

'

'MODIFICHE:

'         12/02/2012   Creata   LAPSRSE   con   impulsi   di   preambolo   impostabili
dall'utilizzatore.

'

SEQUENCE LAPSRSE

'Logarithmically  distributed  Aperiodic-Pulse-Sequence  Saturation  Recovery  with  Spin
Echo

'-------------------------------------------------------------------------------
----------------------

'Based on the Saturation-Recovery Spin Echo experiment (SRSE), this sequence replaces
the

'first pulse of SR by a train of preparatory pulses with logarithmically decreasing

'separation. This efficient magnetization-nulling sequence makes it unnecessary

'to use any recycle delay and tolerates large mis-calibrations of PW90.

'It uses 10 preparatory pulses starting from about 65T1max down to 50 us.

'It should suppress magnetization of all components with T1's in this range and should
work even with

'very inhomogeneous B1 field. The following parameters are used:

'PW\tExcitation pulse (default = 90 degrees)

'P1\tPulse width of the preparatory pulses

'P2\tRefocusing pulse (180 degrees)

'D1\tReserved preamble pulses

'D2\tRelaxation delay (TAU)

'D3\tDefault echo delay

'D4\tHalf echo delay
```

```
'D5\tBy default half echo delay
'RINH,ACQD and STIM have their usual meaning.
  D0
  P1;D1(0.300000)        'Pulse and exponentially decreasing delay
  P1;D1(0.123246)
  P1;D1(0.050632)
  P1;D1(0.020801)
  P1;D1(0.008545)
  P1;D1(0.003511)
  P1;D1(0.001442)
  P1;D1(0.000593)
  P1;D1(0.000243)
  P1;D1(0.000100)
  P1;D1(0.000003)
  D2;PW;D4;P2;D5
#TIME0             'Time axis starts at top of echo
  STIM             'Scan
#SETUP             'Setup section:
  RD = 0           'Default recycle delay = 0
  D0 :(RD)
  P1 = 99 [p(x,x,y,y)]   'APS pulse
  D1 : 0                 'Reserved preamble pulses times
  D2 =(TAU)              'Relaxation delay
  PW = 90 [p(x,-x,y,-y)] '90° excitation pulse
  D3 = 50e-6             'Default echo delay
  D4 :((D3-P2)/2)        'Half echo delay
  P2 = 180 [p(y,y,x,x)]  '180° pulse
  D5 = (D4)              'By default half echo delay
  ENDS [p(x,-x,y,-y)]    'Accumulation
END SEQUENCE
```

```
SEQUENCE LAPSRSE/S

'Multi-block version Logarithmically distributed Aperiodic-Pulse-Sequence Saturation
Recovery with Spin Echo

'-------------------------------------------------------------------------------------
------------------------

'Based on the Saturation-Recovery Spin Echo experiment (SRSE), this sequence replaces
the

'first pulse of SR by a train of preparatory pulses with logarithmically decreasing

'separation. This efficient magnetization-nulling sequence makes it unnecessary

'to use any recycle delay and tolerates large mis-calibrations of PW90.

'It uses 10 preparatory pulses starting from about 65T1max down to 50 us.

'It should suppress magnetization of all components with T1's in this range and should
work even with

'very inhomogeneous B1 field. The following parameters are used:

'PW\tExcitation pulse (default = 90 degrees)

'P1\tPulse width of the preparatory pulses

'P2\tRefocusing pulse (180 degrees)

'D1\tReserved preamble pulses

'D2\tRelaxation delay (TAU)

'D3\tDefault echo delay

'D4\tHalf echo delay

'D5\tBy default half echo delay

'RINH,ACQD and STIM have their usual meaning.

  D0

  P1;D1(0.300000)        'Pulse and exponentially decreasing delay

  P1;D1(0.123246)

  P1;D1(0.050632)

  P1;D1(0.020801)

  P1;D1(0.008545)

  P1;D1(0.003511)

  P1;D1(0.001442)

  P1;D1(0.000593)
```

```
  P1;D1(0.000243)
  P1;D1(0.000100)
  P1;D1(0.000003)
  D2;PW;D4;P2;D5
#TIME0             'Time axis starts at top of echo
  STIM             'Scan
#SETUP             'Setup section:
  RD = 0           'Default recycle delay = 0
  D0 :(RD)
  P1 = 99 [p(x,x,y,y)]   'APS pulse
  D1 : 0                 'Reserved preamble pulses times
  D2 =(TAU)              'Relaxation delay
  PW = 90 [p(x,-x,y,-y)] '90° excitation pulse
  D3 = 50e-6             'Default echo delay
  D4 :((D3-P2)/2)        'Half echo delay
  P2 = 180 [p(y,y,x,x)]  '180° pulse
  D5 = (D4)              'By default half echo delay
  ENDS [p(x,-x,y,-y)]    'Accumulation
  EACN= "BACQ"         'Listed parameter
  NBLK= 128              'Multi-blocks for SR sampling
  BACR= "TAU"
  BGRD= "LOG"
  BINI= 50e-6            'first tau in SR sequence
  BEND= (4*T1MX)         'last tau in SR sequence
END SEQUENCE
```

3.3.3 A tool for NMR data pre-inversion processing: the "Field Cycling" software

Many low-field spectrometers are generally analogue systems, so the data quality often does not warrant intensive processing and so many experimentalists decide to study only the magnitude of the NMR signal. Nevertheless there are several stages of initial processing that can be applied to low-field NMR data prior to fit them. The exact choice of the processing method will depend on the data acquired.

When a lot of NMR noisy data have been acquired, prior to data inversion, it could be useful to do a data compression. This choice could be successful, for example, when the echo shape is complicated, or when SNR is low, so a direct fitting of each echo becomes impractical.

The home-made software "Field-Cycling" (Figure 3.10) gives the possibility to export crude data in the format that the experimentalist prefers. It is possible to choose to work on real, imaginary, module or module with sign data. Furthermore it is possible to do a windowing on data. This could be useful when one needs to analyse for example many FID or echoes in a staggered sequence (a sequence where each experiment is repeated after an inversion time, to obtain a series of FID o echoes that sample all the magnetization curve). The data windowing permits to choose the number of points to compute and it can give back the mean, the maximum and the extrapolation of the windowing. This type of pre-processing data has been essential for crude data from LAPSRSE. In this case the echoes shapes were complicated and the windowing on n points of the echo, on which the maximum value was chosen, was usually adopted. After the windowing chosen the software can also fit a monoexponential fit to the data. It is possible to visualize the fit. Furthermore in the software are implemented different model for the fit (both on T_1 and T_2), where parameters can be changed. The pre-processing of data can be exported for the inversion knowing that a stable and reliable inversion will be obtained with reasonable SNR and an adequate number of data points.

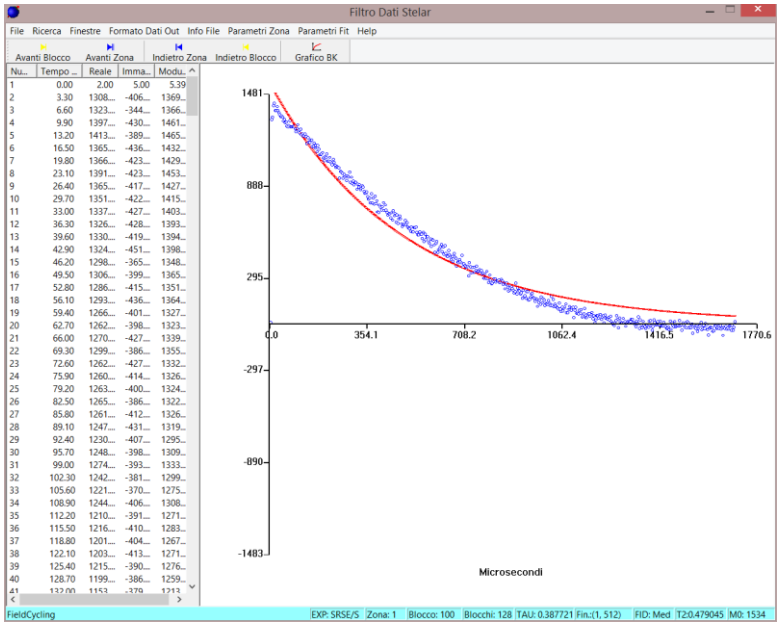

Figure 3.10 *Field Cycling screenshot. Example of CPMG data, with fitting curve of data.*

3.3.4 The NMR data inversion: the home-built UpenWin software

To work with times distributions, it is necessary to properly invert the acquired signal, in order to obtain possibly reliable times distributions which truly represents the original relaxation signal.

NMR relaxation data may consist of exponentially decaying components with a small number of discrete relaxation times, or times constants, or there may be a continuous or quasi-continuous distribution of relaxation times over some range. These distributions can be well obtained by amplitudes computed from the relaxation data at predetermined sequence of systematically-spaced relaxation times, usually equally spaced in log-time. However, such computed distributions can contain more detail than those determined by the data, which are always subject to some noise. The computed distributions are therefore subjected to some kind of smoothing, or "regulation" to avoid details that are not meaningful.

The name UPEN (Uniform PENalty; Bortolotti et al., 2009) refers to the application of negative feedback to a smoothing "penalty" function to prevent excessive detail in

distributions of relaxation times. This allows appropriate smoothing of both sharp peaks and broad features in the same distribution, allowing the sharp peaks without breaking broad features into multiple peaks not required by the data. This allows meaningful computation of the noise and supports additional UPEN objectives, which include identifying various data features and data problems, giving a series of diagnostics and warnings and allowing processing options where needed.

Many inversion algorithms minimize the sum of errors squared plus a "penalty" term. If the input data are signals s_i at times t_i and computed distribution amplitudes are g_k at relaxation times T_k (equally spaced in log-time), the quantity to be minimized is:

$$\underbrace{\sum_{i=1}^{N}\left[g_0+\sum_{k=1}^{M}g_k e^{-\frac{t_i}{T_k}}-s_i\right]^2}_{Errors}+\underbrace{C\sum_{k=2}^{M-1}\left(g_{k-1}-2g_k+g_{k+1}\right)^2}_{Penalty} \qquad (3.1)$$

The Smoothing Coefficient C appropriate for one part of a distribution may differ greatly from that appropriate for another part. In UPEN the smoothing coefficient depends on relaxation time T_k, and the coefficients C_k are adjusted by iterative negative feedback to give approximately the same penalty for all parts of the distribution with significant detail. The quantity to be minimized is now:

$$\underbrace{\sum_{i=1}^{N}\left[g_0+\sum_{k=1}^{M}g_k e^{-\frac{t_i}{T_k}}-s_i\right]^2}_{Errors}+\underbrace{\sum_{k=2}^{M-1}C_k\left(g_{k-1}-2g_k+g_{k+1}\right)^2}_{Penalty} \qquad (3.2)$$

UpenWin (screenshot in Figure 3.11) is a 32 bit application for Windows (currently tested under windows 98, XP, Vista, 7 and 8), now developed in C++ and MFC (Microsoft Foundation Class) by means of Visual Studio 2013, that implements an interface to facilitate the use of UPEN and its related input files. It is composed of a simple single

document interface application with many dialog windows. Among other things, it has a simple text editor (window-editor interface) where one can edit the parameters file used for Upen processing. By means of the dialogs the user can pre-process the data file using the appropriate filter program, sets the appropriate parameters values for UPEN and runs a computation session. When the window-editor interface is empty (no parameters file is loaded) and the user runs a computation session, Upen will use the values of parameters that are set in parameters-dialogs. On the contrary, when a set of parameters is open in the window-editor interface and the user runs a process session, Upen will use the values of parameters shown (on the screen) in the window-editor interface bypassing the values that are set in parameters-dialogs. For further details on Upen parameters see Appendix B.

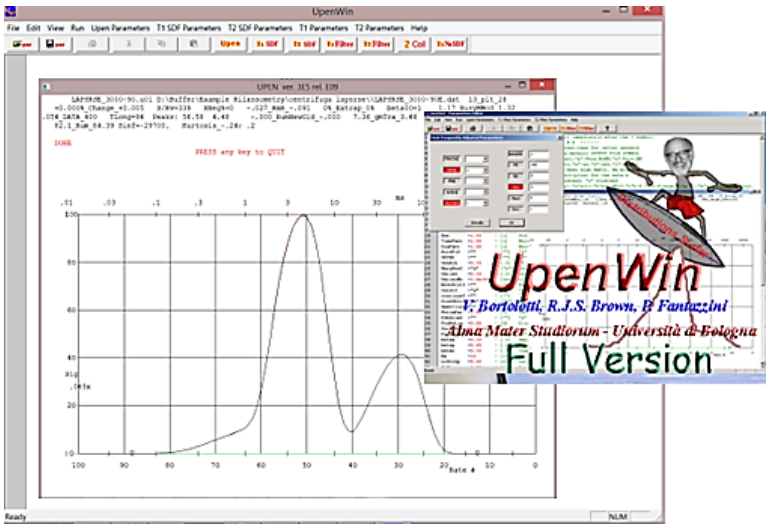

Figure 3.11 *UpenWin screenshot. Example of a relaxation time distribution.*

3.3.5 The creation of a tool for NMR data post-inversion processing: the "FiltroDAT" software

Generally when times distributions are made of different not weel-defined components, a cut-off method can be used to determine how much signal belongs to a components or to another. This could be useful when one is interested in studying only part of the

relaxation times distribution, for example when a time distribution appears multi-modal and it is important to analyse only one component at a time.

The software "FiltroDAT" (Figure 3.12) is able to do a geometric mean of the signal, given the upper and lower limits in term of relaxation times, in order to isolate one component of interest. For example, the method can be used with distribution from irreducible water experiments (Coates et al., 1999) to obtain information on bound water porosity. In this case it is first necessary to do a minima study to find the range of time between which is included the component of interest. Once the time limits are known, it is possible to use them as lower and upper boundary in the software, whose algorithm will calculate some useful parameters as the interpolated cumulative signal, the geometric mean of the range of times selected and the number of points used in the calculation, on the fully saturated times distribution.

In this research thesis this software was created to obtain information on heterogeneous samples, such as unconsolidated porous media (e.g. treated soils), which presents a wide range of pore dimensions and where pore dimensions distributions are important to study physico-chemical properties. For this reason the study of some specific compartments is greatly required.

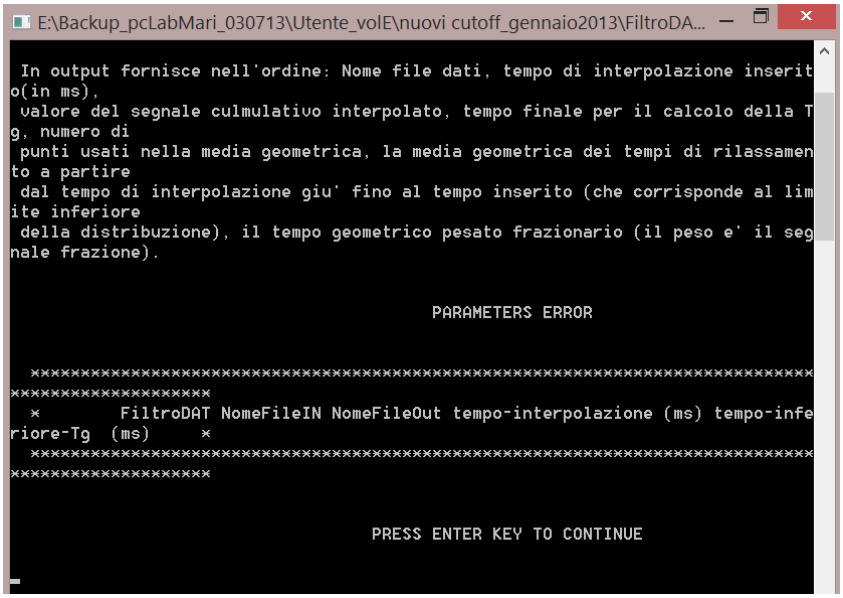

Figure 3.12 *FiltroDAT screenshot.*

3.3.6 ARTS for MRI

Here a brief description, to complete the software list, of the home-made software for MRI images analyses.

The software ARTS (Figure 3.13) examines MRI images given in a specific proprietary format, not the DICOM format which is produced by the tomograph acquisition, but properly changed to obtain quantitative information from the images.

For each pixel of the image, or creating a region of interest (ROI) made on *n* pixels inside the image, it is possible to extract information on the value of magnitude of the magnetization.

Furthermore ARTS can elaborate a series of images (acquired at different inversion times or echo times) to obtain a T_1 or T_2 maps, which are the results of the QRT technique. In this case the image realized are two: the first give the values of T_1 or T_2 for each pixel or ROI, the second represent the magnitude of the magnetization in each pixel or ROI.

ARTS give also the possibilities to do a series of operations on images (noise reduction, histogram calculation, …) that are fully illustrated in Appendix C.

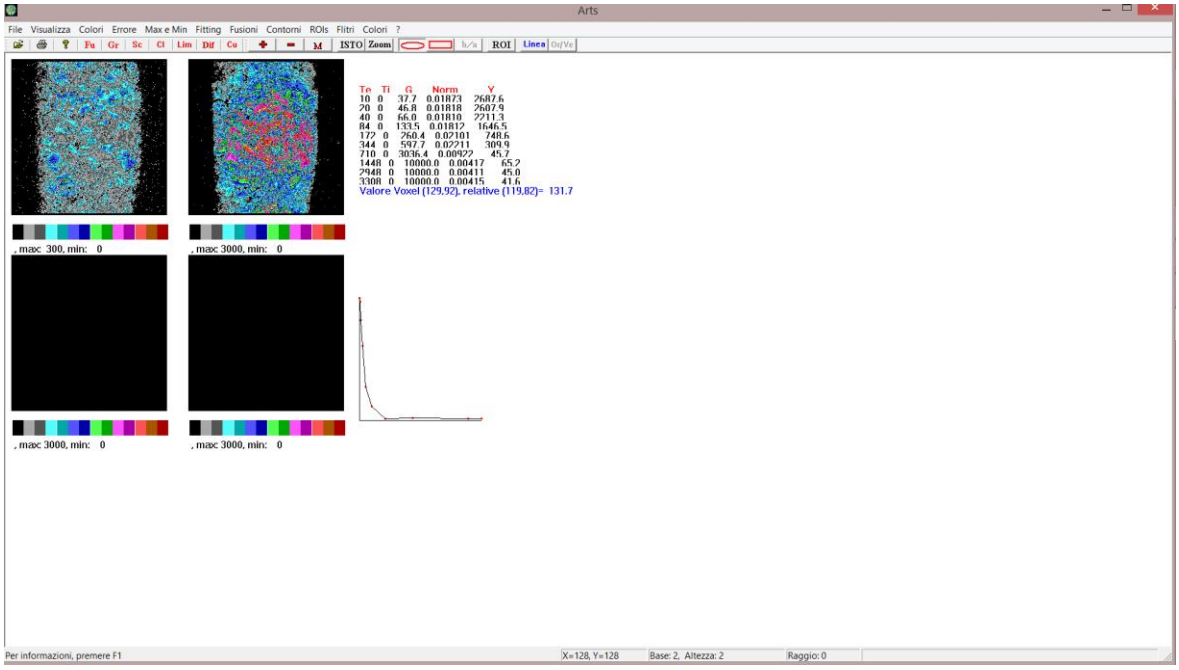

Figure 3.13 ARTS *Screenshot. Example of T_2 map of a compost sample.*

3.3.7 PERFIDI sequences optimization

Below a brief description of the optimization done on the already tested PERFIDI sequences. In medical MRI dedicated sequences able to image only specific parts or components of organs and/or tissues are of great importance to obtain images with high contrast. This is the case of Parametrically Enabled Relaxation Filters with Double and multiple Inversion (PERFIDI) sequences (Sykora et al., 2007), which are methods based on the different longitudinal relaxation times (T_1) of the tissues, able to selectively filter pixels signals and therefore create contrasted images. In particular, the innovative PERFIDI sequences that implement T_1 filters have been further developed to be applied also in imaging. In fact the validity of this family of filters has been tested overall by MRR. Only a few examples of MRI applications have been presented (Bortolotti et al., 2010). A sample characterized by a distribution of T_1, can be filtered by PERFIDI sequences using preambles of inversion pulses before standard sequences (Figure 3.14), provide an effective attenuation of the signal in a selected range of T_1 values, while the remaining signal undergoes a computable attenuation. These features make PERFIDI filter sequences

different from other techniques dedicated to the signal selection found in literature, such as Short Time Inversion Recovery and Multiple Inversion Recovery (Bernestien et al., 2004), whose effects, in general, is to zero the signal for a discrete number of T_1 values. Furthermore PERFIDI have the advantage to filter the signal during the acquisition and not during post processing. In other words, the PERFIDI method is similar to electronic band-pass, high-pass and low-pass filters, that are primarily focused on the components which pass through, rather than on those that are blocked. The PERFIDI method is in the linear algebraic combination (with sign) of magnetization signals. Therefore, it can work only if memory of the polarity (the sign) of the nuclear magnetization vector respect to the direction of B_0 is kept. In MRR this is not a problem, because the magnetization signal is always recorded with sign. On the contrary, in MRI a "magnitude" image is usually recorded and visualized. This image is computed by means of a 2D Fourier transform of the raw data. Therefore, in order to apply the PERFIDI method to MRI it is necessary to restore the magnetization sign. The PERFIDI technique is now more complete thank to the sign restoration, which is obtained using a reference image having a well-defined polarity of the signal in each image pixel. Once this polarity is known, it is possible to apply the PERFIDI filters.

Moreover the PERFIDI filtering is a linear combination of images acquired with proper sequences called PERFIDI blocks, each characterized by specific delays and rf pulses. Each PERFIDI block is made of two parts. The first one is a presaturation preamble, made in our implementation of two inversion rf pulses, whose timing is varied depending on the desired filter behaviour, while the second one is a standard image acquisition sequence.

As to apply PERFIDI filters it is necessary to keep memory pixel by pixel of the sign of the magnetization signal, a method to determine this sign was implemented. In particular the phase of each pixel of the acquired image was studied. Therefore, it has been necessary to compute for each pixel the value of the phase, starting from the complex raw data of the acquired image.

An ad hoc algorithm was implemented in MATLAB (Balbi et al., 2015) which includes an unwrapping procedure, an evaluation of the phase ramp slope by linear fitting with the subsequent compensation, to obtain from the raw data the values only of the second part of the phase, related to the polarity of the magnetization vector. The signal polarity of each pixel in the PERFIDI image has been obtained by comparison of the value of the phase, with that of the corresponding pixel in the standard image, whose polarity is known.

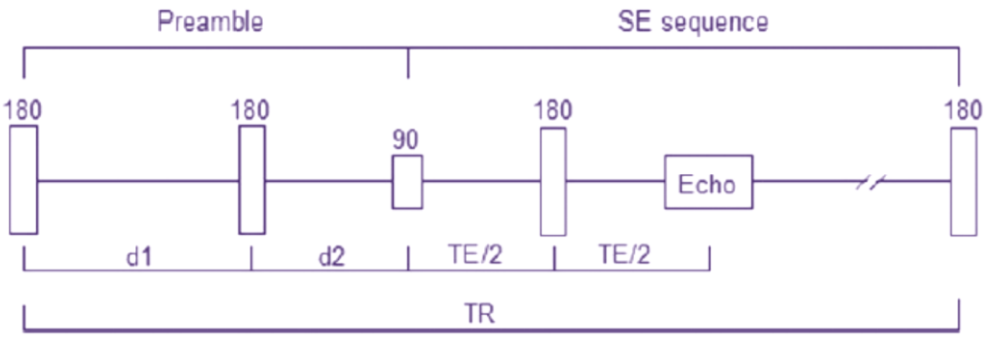

Figure 3.14 *PERFIDI sequence time diagram, image from Balbi et al., 2015.*

Chapter 4

Paper waste for soil recovery: how organic matter influences soil properties

4.1 Introduction

Since the need of achieving sustainable and more environmentally sound waste disposal strategies has become an essential topic, recently, new examples of reusing non-hazardous wastes, such as wastes from wood and paper processing, are being used as supplements for soils in farming and land remediation. These operations on soil focus on the restoration of Organic Matter (OM), re-establishing nutrient cycles and decreasing toxic levels of heavy metals, soil acidity and salinity (Fierro et al., 1997). An indication of OM quantities can be obtained by measuring the Total Organic Carbon (TOC), which in waste materials used in remediation is generally high, typically few tens of percent (w/w) (Beauchamp et al., 2002).

As paper is one of the most widely recycled materials, among its many types of waste that can be eventually used in different recycling options, paper sludge is one of the most used. In Italy, as well as in Europe, paper sludge is less and less considered as a waste (and, as such, disposed of to landfill or incinerated), and the reuse for environmental remediation (such as landscaping and dismissed quarry or mining areas reclamation) is strongly recommended due to its stability in aerobic conditions (Assocarta 2012). It is worthy to recall that, thanks to the presence of cellulose and wood fibres, paper sludge is a biomass rich in organic content, and therefore, anaerobic degradation (with CH_4 and CO_2 production) is very likely to happen.

The widespread use of this kind of treatment on soils has increased the need to gain in depth information on the interactions between the mineral components of soil and OM and also with other contaminants.

Soil has a complex structure which refers to the size, shape and arrangement of particles and pores, continuity of pores, their capacity to retain and transmit fluids and organic and inorganic substances (Bronick & Lal, 2005). Soil, in general, is formed by several aggregates of particles of different size. Pores can be found between the aggregates (inter-aggregates) or inside the aggregates (intra-aggregates). Moreover, the particles of

aggregates can have a porosity themselves (crystal defects or cracks) (Fernández-Ugalde et al., 2013). The complex structure of aggregates are the result of the interaction of many factors including the environment, soil management, plant influences and soil properties such as mineral composition, texture, TOC concentration, pedogenic processes, microbial activities, exchangeable ions, nutrient reserves, and moisture availability (Bronick & Lal, 2005).

A traditional method in soil sciences is to measure the total organic carbon content (TOC) and the total organic carbon-to-nitrogen ratio (TOC/N). This ratio is an important indicator of natural soil conditions, since its constancy is a distinctive characteristic of the quality of soils and, by extension, of treated soils. In general, favourable conditions for the decomposition of organic residues narrow the range of TOC/N values (Stevenson and Stevenson 1994). In natural soils, TOC/N generally ranges from 10 to 12 and often decreases with depth, in some cases attaining values < 5. Likewise, TOC/N is used to estimate the risks associated with remediation procedure, since a specific TOC/N threshold value establishes the risk of biogas production in polluted soils (Adani 2004). TOC/N ratio, together with P, Ca, Mg, Na and K concentrations can be used to better characterize treated soils.

The increasing use of recycled materials in soil remediation activities involves environmental implications not yet well defined, which are objects of study of numerous and interdisciplinary research fields. Possible contamination stimulated the use and customization of innovative techniques to characterize these materials. As already said, proton nuclear magnetic resonance is a powerful non-invasive and non-destructive technique that can be adequately employed to investigate porous media in the TD-MMR. This is true not only for consolidated porous media (e.g., rocks), but also for unconsolidated ones (e.g., soils).

Application of the MRR technique in petrophysical and geophysical sciences are today well established, however, not yet frequently used in soil science, although it exhibits great potential. Heterogeneity of soils and the particular structure of OM contained in soils (not

yet fully understood) do not allow one to easily transfer one-to-one MRR geophysical or petrophysical studies to soil science (Bayer et al. 2010). Moreover, in natural soils, the paramagnetic ions concentration is high enough to significantly change the surface relaxivity ρ, by increasing ρ of some order of magnitude if compared with systems with no paramagnetic ions. This can be the case of treated soils, which can contain a higher concentration of paramagnetic ions with respect to natural soils, making the application of MRR techniques more difficult. The purpose of this study was to investigate the use of MRR techniques to characterize real treated soils, in order to get information on how the high content of OM can affect the distribution of relaxation times. MRR measurements have been associated to SSA measurements, traditional soil analyses and SEM images to gain a deep description of the treated soils. In particular, the correlation of T_1 relaxation time distributions (T_1 distributions for short) with respect to TOC content has been investigated. As mentioned above, treated soils often pose several experimental problems, and meticulous experimental care must be adopted. In fact, the presence of paramagnetic ions significantly influences data measured in the time domain, possibly inducing substantial misinterpretation of the inverted relaxation time distribution. Indeed, the inversion of multiexponential relaxation data is a notoriously ill-posed problem (Provencher 1982), and thus, particular care must be adopted to prevent the production of relaxation time distributions with artefacts details which might be misinterpreted, for example, as physically meaningful resolved porous compartments. It is important to recall that the particular sample preparation procedure (quantity of saturating water, mixing and compaction procedure, etc.) affects the pore distributions, and so the shape and modality of relaxation time distributions. Thus, particular care has been used to prepare and investigate the samples (see paragraph 3.2.2). Moreover, the T_2 analysis usually adopted in soil science, normally performed with the standard CPMG sequence (Bayer et al. 2010), cannot easily be used in quantitative analyses of treated soils samples, because of their strong paramagnetic ions content. Furthermore the nature of soils samples and the large dimensions of the dedicated probe used (to accommodate a more representative quantity

of sample) forced the NMR relaxometer to take measurements close to its instrumental limits its electronic dead time, in some cases, was comparable with the length FID signal to be acquired, excluding therefore the possibility to use, for example, the standard inversion recovery sequence. To overcome all these problems, it has been necessary to develop the more convenient NMR sequence LAPSRSE (already explained in the paragraph 3.3.1) to obtain more reliable NMR signal.

The study highlight the possibility to characterize the Pore Size Distribution (PSD) and the irreducible water (Dunn et al., 2002), or bound water (which can be associated with the porosity with average pore diameter < 2 μm Vannini et al., 2012) with MRR. However, as ^{1}H MRR relaxometry is somewhat limited by the instrumental hardware, the information on pores smaller than ≈ 100 nm can be obtained with N_2 adsorption/desorption techniques to investigate the PSD < 300 nm and the Specific Surface Area (SSA) associated.

The knowledge of PSD is one important key factor in understanding fluids and nutrients transport, and TOC turnover (Bronick & Lal, 2005). In general, at each pore size range there is associated a specific physico-chemical process (Echeverria et al., 1999). It is a common practice in several research fields (soil science, geophysical science, petrophysical science, polymer science, etc) to classify the pores as micro, meso or macropores, but the choice of a specific size to delimit pore ranges is necessarily arbitrary and it is often related to the experimental technique used (Beven & Germann, 2013). Therefore in our case the pore classifications used will be necessarily related to the technique used.

Mineral SSA has a leading role for the sorption of OM, which is a major process for its preservation. The ability of soils to accumulate organic matter is limited most probably by the availability of the SSA (Kaiser & Guggenberger, 2003). Even at maximum resolution, however, it is difficult to detect thin organic coatings on the mineral surface (e.g., adsorption of low molecular-weight OM) by most current microscopic methods (Wagai et al., 2009).

For this reason we decide to combine to MRR the N_2 adsorption/desorption approach to measure the SSA of soil, where the behavior of introduced gas molecules at surfaces

which lets the characterization of much larger volume or mass of samples than microscopy (Wagai et al., 2009). This technique adopts the IUPAC classification to define the range of micro, meso and small macropores, see Table 4.1 (Sing, 1985). Micropores, which have been reported to be inter- and intra-particle pores, may be associated with clays and compounds such as Fe and Al hydroxides (Fischer, 1996; Aringhieri, 2004; F. Cabrera, 1981; Cornell, 1996); whereas mesopores are due to the inter-particles porosity of clays and aggregates (Mayer et al., 2004).

Furthermore, the SSA and the PSD of soils have been proved to be related to their TOC content. In particular the SSA is inversely related to the TOC content, according to several studies (Kaiser & Guggenberger, 2003). In fact, soil OM has low SSA (~1 m^2 g^{-1}), when measured by N_2 adsorption, (Kaiser & Guggenberger, 2003; De Jonge & Mittelmeijer-Hazeleger, 1996) and likely covers or fills micro- and mesopores associated with clay-sized mineral particles and their aggregates, reducing the N_2-accessible surface area of aggregates (Mikutta et al., 2006; Wagai et al., 2009).

Also further analyses, such as Scanning Electron Microscopy (SEM), X-Ray Diffraction (XRD), and traditional soil analyses such as granulometry, pH, total carbon and carbonates content have been performed. The main result obtained is the validation of the clogging effect of micropores by OM: the higher the OM content the higher the clogging effect of certain pore sizes, as already observed with in other experiments with other techniques (Six *et al.*, 2002; Mikutta *et al.*, 2004).

Table 4.1. *Pores classification according to the IUPAC (Sing et al., 1985) and the petrophysical cut-off method (Vannini et al., 2012) used in this study.*

Classification	Pore type	Dimensions
IUPAC	Micropore	< 2 nm
	Mesopore	2-50 nm
	Macropore	> 50 nm
Petrophysical cut-off	BWP (bound water pores)	≤ 2 μm
	FWP (free water pores)	> 2 μm

4.2 Materials and methods

4.2.1 Samples and TOC analysis

Amended soil samples come from a land reclamation area located in Northern Italy, in which authorized wastes were mixed with natural soil to reclaim a hillside profile. Among the authorized wastes there was Paper Mill Sludge (PMS). The total volume of waste was about 12000 m^3, with about 1/3 of PMS which contains cellulose fibres, together with mineral charges and residual inks. The presence of biogas in the remediation area, proved the fact that the mix of soil-waste was not well done, both for the intervention depth and for incorrect quantities used. A sample of natural soil (without waste addition) was collected as a reference sample (sample SP3). It is a silt soil, with 2% of sand (63-2000 μm), 88% of silt (2-63 μm) and 10% of clay (< 2 μm) (percentages obtained by both sieving granulometry and laser granulometry methods), with no significant presence of carbonates (Table 4.2). Its pH was approximately around 4.4.

Figure 4.1. *Preparation of the treated soil samples from sieving to NMR measurements.*

In order to characterize the soil-waste mixture, disturbed samples have been selected on the basis of the TOC content (less than 1 % w/w up to 14 % w/w), in order to cover a wide range of possible TOC values. The samples used in this work are summarized in Table 4.2.

All samples were air-dried, sieved (< 2 mm) and dried at 40℃ prior to any further analyses (see the steps of laboratory preparation of the sample in Figure 4.1).

The determination of the TOC contents has been obtained as the difference between the total carbon and the inorganic carbon, both determined using a SSM-5000A Shimadzu TOC analyser (located at the CIRI Laboratories, Rimini, Italy) for solids, by means of infrared detection of CO_2 percentages. The inorganic carbon measured is the carbon present in carbonates. For each sample four replicates were examined.

4.2.2 Scanning Electron Microscopy coupled to Energy Dispersive Spectroscopy

SEM coupled with Energy Dispersive Spectroscopy (EDS) were performed using an EVO 50 Series Instrument (LEO ZEISS) equipped with both an INCA Energy 350 EDS micro-analysis system and an INCA SmartMap to image the spatial variation of elements (Oxford Instruments Analytical). The accelerating voltage was 20 kV, and the spectra collection time 60 s. 10 regions of interest were analysed for every sample, in every region SEM images at different magnifications were taken. In every region of interest 3 EDS spectra were measured.

4.2.3 X-ray Diffraction

X-ray Diffraction (XRD) analyses were carried out using a Philips PW1050/81 diffractometer equipped with a graphite monochromator and controlled by a PW1710 unit (CuKα-Ni filtered, λ= 0,15418 nm). A 2θ range from 5° to 80° was investigated at a step size of 0.05 º and time per step of 2 s.

4.2.4 ^{1}H-MRR measurements

MRR tests were performed with a homebuilt full size relaxometer (accommodating samples up to 13 cm in diameter) that works with the low field permanent magnet (see paragraph 3.2). Before MRR measurements, all soil samples were dried at 40°C (a low temperature to minimize OM damage) to remove moisture and then sieved (ASTM mesh 10). The dry powder underflow was hydrated with a fixed proportion of water (40% of dry mass) and mixed apart, then sealed in cylindrical MRR test tubes (diameter 25 mm), approximately filled for 20 mm in height to better adapt to the sensitivity volume of the coil and to fit into a more favourable volume of magnetic field homogeneity (see Figure 4.1). The T_1 signal were acquired using the specifically developed multi-block sequence LAPSRSE (paragraph 3.3.1). For this sequence, 64 echoes were acquired from an initial LAPSRSE saturation recovery time of 50 μs to a final time equal to four times the maximum T_1 expected. This parameter ranged between 40 and 100 ms according to the maximum T_1 of the samples. In all experiments, in order to be sure that all the transversal magnetization components were destroyed before starting the acquisition, the time between the last pulse of the saturation pulses preamble and the first excitation pulse was set on the order of 100 μs. Also the echo time was the same for all experiments and, as the relaxometer dead time for the transmitter receiver coil of 1" was about 25 μs, it was fixed at 29 μs. The duration of the 90 degree excitation pulse was 11 μs. Every sequence was repeated for 32 scans to obtain an acceptable signal to noise ratio, of value of approximately 250. Phase-cycling procedure was used in all acquisitions.

All data have been processed with the UpenWin software (paragraph 3.3.4), to obtain distributions of relaxation times without multiple peaks not required by the data to be separate, preventing physical misinterpretation of data.

Vannini et al. (2012) used the petrophysical cut-off method based on the centrifuge desaturation method to identify BWP. Centrifuge cycles with increasing speeds (between 1000 and 3000 RPM) and duration (between 30 and 90 minutes) were used until a

constant mass sample was obtained. It is supposed that the progressive shift of the T_1 distributions towards short relaxation times, as a consequence of the desaturation of the samples, could be used to identify BWP.

It is important to underline that the relaxation of the ^1H nuclei magnetization represents an average over regions that can be much larger than a "single pore". Our samples are in the fast diffusion regime (as will be discussed in the results section), and this regime implies that spins can diffuse to relaxation sites on the grain surface much more rapidly than they undergo relaxation at the surface (Dunn et al., 2002). Approximately the distance that a spin can travel by diffusion before relaxing is representative of a volume (the diffusion cell) in which the relaxation of the magnetization is uniform. That is, stated in other words, all spins within the entire pore network of a diffusion cell relax with monoexponentially rate, and the relaxation times distribution will display a single peak representing all the pores of different size present inside the diffusion cell itself (Grunewald & Knight, 2009). Therefore the whole MRR signal represents the averaged signal coming from diffusion cells, each of which represents a network of several pores of different size.

4.2.5 T_1 cut-off determination

The ambiguity of micropores definition, as discussed above, suggested the use of the typical petrophysical cut-off method to identify micropores by NMR. The capillary-bound water in the pore space, called irreducible water saturation, is associated to the short components of the NMR relaxation times and for its estimation it can be useful to set a specific relaxation time (cut-off) below which the water is immobile (Dunn et al., 2002). Using the cut-off method, usually based on a fixed T_2, that divides the T_2 distribution into two parts, the irreducible water can be evaluated. The two parts are related to pores containing bound water and pores containing free water (which we identified as water in micropores), respectively. In this study, the cut-off is applied to T_1 distributions, and the desaturation was obtained with the centrifuge technique, a common approach in

petrophysical applications (Coates et al., 1999). When the mass of the centrifuged sample becomes constant, it is supposed that the respective T_1 distribution is representative of the distribution of irreducible water saturation. Therefore it is possible to deduce a T_1 cut-off value below which the T_1 values represent only bound water, which we assumed mainly as the water filling the micropores. Treated soils samples used for cut-off experiments were prepared following the same procedure described above, and NMR measurements were performed after each centrifuge run, to follow the decrease of water mass and to use the total NMR signal detected to test the ability of the NMR apparatus to correctly detect the mass of water loss.

For clearly, hereinafter in the MRR results micropores will be referred as bound water porosity (BWP) and macropores, free water porosity (FWP). Data were examined with the software Filtro.dat (see paragraph 3.3.5)

4.2.6 Relaxivity evaluation

In this study, we supposed that saturated samples are in the fast diffusion regime, since fluids are confined in a porous medium. Under this hypothesis the longitudinal relaxation time of confined ^{1}H fluids is related to the surface relaxivity coefficient ρ and to the S/V ratio. Almost all MRR studies on these kinds of samples assume that spins system satisfy this condition. Test to evaluate the dependence of the T_1 distribution with respect to the temperature can be made. In fact, if a sample is not in the fast diffusion regime, then the relaxation time of confined fluid is related to D, the fluid diffusion coefficient of spins in the pore fluid, and which is very sensitive to the temperature variations. Conversely, ρ for many kinds of samples is not appreciably sensitive to temperature variations. So, a null or a weakly dependence of the T_1 distribution with respect to the temperature variations could be assumed, in a first rough approximation, as an indication that the sample is in the fast diffusion regime (Dunn et al., 2002). Tests were made on T_1 distributions of a single treated soil sample measured at three different temperatures, 5 ˚C, 20 ˚C and 40 ˚C

respectively, which proved that samples are in the fast diffusion regime. Moreover, the geometric information of the porous system is only characterized by the internal pore surface area to pore volume ratio S/V (see paragraph 2.3.4). So that, for T_1:

$$\frac{1}{T_1} = \frac{1}{T_{1bulk}} + \frac{1}{T_{1surface}} = \frac{1}{T_{1bulk}} + \rho_1 \frac{S}{V} \tag{4.1}$$

where ρ_1 is the longitudinal surface relaxivity. The presence of para- and ferromagnetic ions on the pore surface causes strong surface relaxation. In order to use equation (4.1) to evaluate a pore size distribution from a relaxation time distribution, supposing bulk relaxation effects negligible, it is necessary to know the value of ρ_1 and suppose that it is roughly the same over the whole sample. The same equation (4.1) can be used to evaluate ρ_1, but in this case one needs the measurement of S/V, which in general it is not easy to measure, and whose result could change significantly depending on the measurement method adopted (Kleinberg, 1999). Looking for a relation between relaxation data and a single parameter, such as S/V, it is necessary to reduce the relaxation data to a single parameter. A large number of different of such single ''effective'' relaxation times can be formed from a relaxation distribution. In particular immediately after an abrupt change in non-equilibrium magnetization at t=0 (for instance, by a 90° pulse) the magnetization is uniform over the pore space even in slow diffusion regime. Therefore, if ρ_1 is constant over S, the instantaneous relaxation rate at t=0 should be $\rho_1 S/V$, whatever the diffusion regime or pore size distribution. This initial relaxation rate $R_1(0)=1/T_1(0)$, is the arithmetic average rate if a distribution of rates exists, so that:

$$\frac{S}{V} = \frac{R_1(0)}{\rho_1} \tag{4.2}$$

with

$$R_1(0) = -\left(\frac{d}{dt}\right)\ln S(t)\Big|_{t=0} = -\frac{dS(t)}{dt}\frac{1}{S(t)}\Big|_{t=0} \quad (4.3)$$

where $S(t)$ is the reversed longitudinal relaxing signal. $R_1(0)$ extrapolates both the signal and the slope of the T_1 relaxation curve back to an LAPSRSE saturation recovery time t=0 (Borgia et al., 1996).

In case of non-consolidated materials, constituted by grains approximately spherical of diameter d and randomly packed, S/V can be estimated by the following relationship:

$$S/V = 6(1/\varphi - 1)\,d^{-1}, \quad (4.4)$$

where φ is the porosity (Vogt et al., 2002). In this case, substituting the above relationship in equation (4.1) gives:

$$R_1(0) = R_{1b} + \rho_1\, 6\left(\frac{1}{\varphi} - 1\right) d^{-1}, \quad (4.5)$$

$R_1(0)$ is not the only possible NMR parameter useful for the determination of ρ_1. Various single parameters (or kinds of averages) can be computed from distributions, as the relaxation parameters T_1 peak of the distribution and the geometric weighted average time T_1 (T_{1G}). It is remarkable that $R_1(0)$ is computed directly on measured data and not on the distribution relaxation time, thus it completely overcomes the troubles of ill-posed problems. The presence of paramagnetic sites increases the relaxation of nuclear spins in an otherwise diamagnetic bulk environment. Hence, provided that the concentration of dissolved paramagnetic ions is not too high, R_{1b} is a sum of the paramagnetic and diamagnetic contributions (Mitreiter et al., 2010), so R_{1b} can be written as a sum of R_{1b0}, which refers to the relaxation rates in absence of paramagnetic species and the product of

the concentration [M] of paramagnetic substances with r_1 ($mM^{-1}s^{-1}$) the enhancement of the longitudinal nuclear spin relaxation rates due to the presence of M (Helm, 2006).

In order to estimate ρ_1, using equation (4.5), one of the soil samples was sub-sampled in five not overlapping granulometric classes, to avoid grains mixing (frequently, in soils the small grains remain attached to the large ones, forming aggregates) (Pignatello, 1998). Sieves classes used were: 1680-1190 μm, 707-595 μm, 425-300 μm, 250-150 μm and 125-63 μm. Five glass vials (diameter 8 mm) were partially filled (height 25 mm) following the sample preparation procedure (see paragraph 4.2.4). The minimum time of echo of the LAPSRSE was set on the order of 50 μs. A value for $R_1(0)$ was obtained from each LAPSRSE measurement. Special care has been taken to minimize the scatter in the computed results. So, computations were made on sequences of stacks of data blocks (in particular each stack is averaged on 4 blocks) with the last stack subtracted from each of the others. The time of each stack was computed as the geometric mean of the times of the blocks composing the stack. Data elaboration evaluated the S(t) natural logarithm and its linear behavior (shown by equation 4.5) at the very short time of the trend, using the first 20 data of the acquired $S(t)$ signal. The porosity of the sample was estimated with a gas porosimeter. Then, an estimation of ρ_1 has been calculated by means of equation (4.5). It is important to highlight that an unique relaxivity value for all analyzed samples has been used, deduced by only one measured sample, therefore introducing a small systematic error in the further calculation of the pore sizes distributions. Some Authors (Mikutta et al., 2004) indeed found that the mineral soil phase and the mineral soil phase contaminated with polygalacturonic acid have different values for relaxivity, because this acid significantly reduces the SSA of the mineral phase. Furthermore, in soils the TOC is in general correlated to the SSA, so it is likely to expect that TOC may influence the relaxivity values.

Thus, the relaxivity has been estimated using equation (4.2), where now S is the BET specific surface (μm/g), V the specific porosity volume of the sample (m^3/g) and $R_1(0)$ the usual average relaxation rate.

4.2.7 N_2 adsorption/desorption measurements at -196°C

SSA measurements were carried out in a Micromeritics ASAP 2020 instrument. Samples were previously degassed under vacuum at room temperature (to minimize OM damage) at a pressure below 4 Pa. Specific surface area values were calculated by the Brunauer-Emmet-Teller (BET) method. PSD were obtained by the Barrett, Joyner, Halenda (BJH) method in the adsorption branch and the t-plot was used to evaluate the presence of micropores (Rouquerol *et al.*, 1999).

4.3 Results and discussion

4.3.1 Samples standard analyses

In Table 4.2 the results of the pH and total carbon analyses are reported. The higher values of pH are of sample with high concentrations of both organic and inorganic carbon. This probably means a relevant presence of carbonates.

Table 4.2. *Sample name, depth, pH, TOC and inorganic carbon (IC) content of the amended soils samples and of the natural soil (SP3). They have been divided in two groups: SP1, SP2 and SP3 are samples with low TOC content (TOC ≤ 3%), SP4, SP5, SP6 have high TOC content (TOC > 3%). PH obtained using the ASTM D4972-13 (*).*

Sample	Depth / cm	$pH_{(water)}$*	TOC / %	IC / %
SP1	50-97	8.18	0.73	0.17
SP2	5-30	8.23	1.29	0.31
SP3	0-10	4.4	1.49	0.01
SP4	37-72	9.23	5.30	2.80
SP5	45-66	9.7	6.30	5.00
SP6	54-87	8.6	13.90	6.10

4.3.2 SEM and XRD results

The morphology and chemical composition of samples are studied by SEM/EDS. Soil aggregates of 500-50 μm (Figures 4.2 a,b) and inter-aggregate pores of diameter above 2 μm (Figures 4.2 c,d) are appreciable. The samples can be divided into two groups, those with low (≤ 3%) and high (> 3%) TOC content, see table 4.2, in accordance to the maximum value of TOC of the region where soil cores were sampled. The former contain particles composed of Mg, Si, Al, Fe and small amounts of K and Ca. As the TOC content increases, agglomerates of particles and fibres of cellulose of different length, characteristics of PMS (Méndez et al., 2009), have been identified. In the latter the aggregates are more compact and uniform (Figure 4.2 d). They are formed by irregular shaped particles with rounded edges and needle-like particles. The particles contain together with Mg, Si, Al, Fe and K, elements from soil minerals, large amounts of Ca, visible in Figures 4.3 a, b. Ca may be due to the presence of calcite ($CaCO_3$) coming from the PMS, as already observed in a previous work in similar samples (García et al., 2008). Large cellulose fibres are partially covered by mineral particles (Figure 4.3 c, d). Large particles of organic matter tend to be encrusted with mineral soil particles and with the considerable presence of $CaCO_3$, as confirmed by the results of inorganic carbon (Table 4.2), which is only due to the presence of carbonates. The presence of microaggregates (<250 μm, Bronick & Lal, 2005) is detectable in SEM images. Aggregation is generally promoted by $CaCO_3$ and clays (Six et al., 2002; Haynes & Naidu, 1998), both present in samples, as corroborated by pH and IC data (Table 4.2), and XRD analyses respectively. High pH observed could also mean the presence of cations, as Ca^{2+}, which form bridges between clay and OM (Bronick & Lal, 2005).

XRD diffraction analyses confirm that the crystalline phases in soils are clay minerals (kaolinite, smectite and mica) and quartz. $CaCO_3$ is identified in the samples with a high TOC content, in agreement with EDS data above-reported.

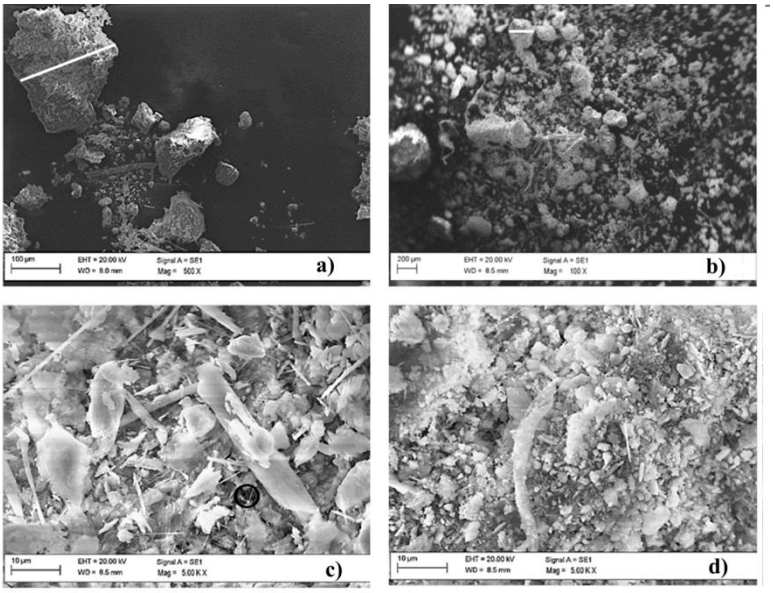

Figure 4.2. *SEM images of* a,c) *SP2 sample (small TOC content) and* b,d) *SP4 sample (large TOC content). Aggregates > 50 µm have been highlighted, and an example of pore > 2 µm has been rounded.*

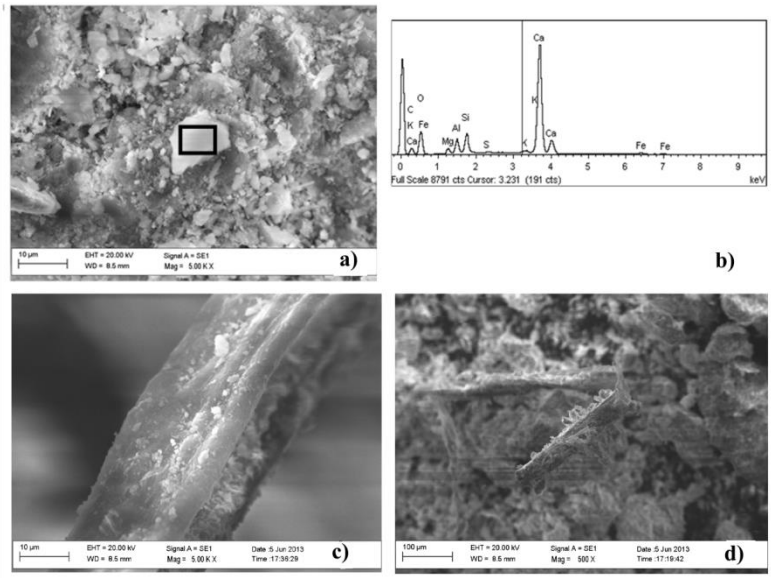

Figure 4.3. a) *Secondary electron image of SP2 and* b) *EDS of SP4,* c, d) *SEM images of large cellulose fibres covered by mineral components of samples with high TOC.*

4.3.3 N_2 adsorption/desorption results

The BET SSA, PSD and the BET constant *C* parameters (Figures 4.4 and 4.5) in the amended soils have been determined by N_2 adsorption/desorption at -196ºC. It should be pointed out that this technique presents some measurements limitations on these types of samples (Heister, 2014). The contribution of the organic matter to the surface area cannot be studied with N_2 as probe molecule, in fact the BET SSA of OM in soils measured by N_2 adsorption is ca. 1 m^2g^{-1} (De Jonge & Mittelmeijer-Hazeleger, 1996; Kaiser & Guggenberger, 2003). CO_2 is preferred to measure organic matter surface area (Echeverria et al. 1999). Thus the values reported here could be underestimated in comparison to the real surface areas. On the other hand, amended samples contain not only different TOC but also inorganic matter, as reported in the Table 4.2. The paper sludge used for the amendment is made of calcium carbonate and clays and shows a S_{BET} of 5.3 m^2g^{-1}, in agreement with values in literature for an untreated paper sludge (Likon & Trebše, 2012).

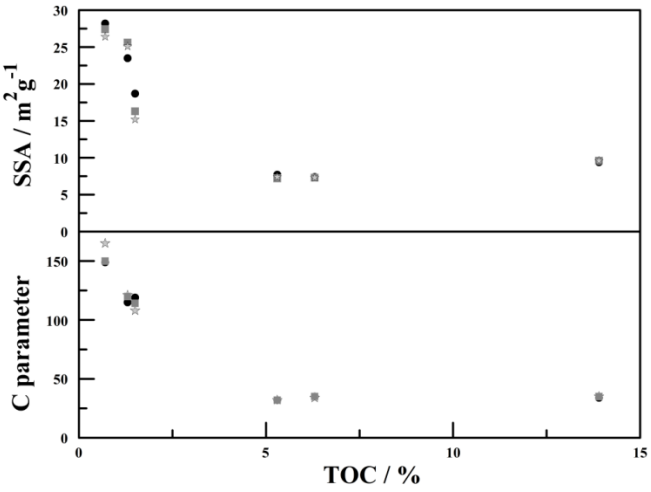

Figure 4.4. *BET SSA and C parameter values for the amended soils. The three replicates of the measurements are represented with different symbols (first replicate, circle; second replicate, square; third replicate, star).*

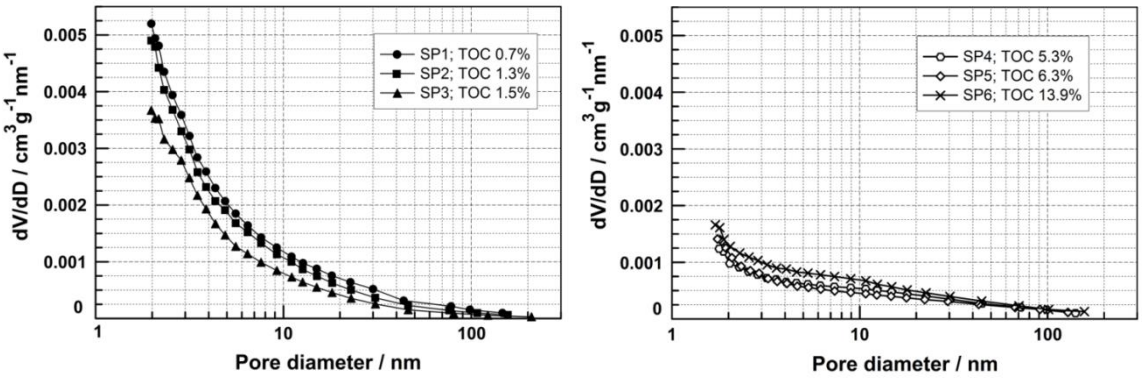

Figure 4.5. *PSD for the amended soils obtained by the BJH method using the isotherm adsorption branch, low TOC content group (left), high TOC content group (right).*

The clays in the amended soils are the compounds that mainly contribute to the surface area measured by N_2 adsorption (Séquaris et al., 2010), thus the gas adsorption approach is mainly affected by clay particles (Wagai et al., 2009). Typical N_2 adsorption hysteresis loops are observed to be narrower in the samples with TOC content above 3%, suggesting that the pores are, in part, modified in the amended soils by the increasing content of OM.

The BET SSA values are displayed in Figure 4.4. It is possible to relate BET SSA to the trend of the TOC, in particular a decrease of the BET SSA corresponds to a TOC increases, in agreement with results previously published for minerals and soils treated with different OM content (Kaiser & Guggenberger, 2003). Nevertheless the sample with 13.9 % TOC deviates from the observed trend, probably due to a contribution of the PMS to the surface area.

With only a few data there is a substantial risk of having over-fitting problems; nevertheless it is worth noting that the trend of SSA data of Figure 4.4 can be well fitted with an exponential function (shown in Figure 4.10 b):

$$SSA = SSA_0 \; e^{-\mathrm{TOC}\cdot k} + offset \,, \tag{4.6}$$

In other words, the amount of fractional SSA decrease due to the increase of TOC is proportional to the amount of TOC variations:

$$\frac{\Delta SSA}{SSA} \simeq -k \cdot \Delta \mathrm{TOC} \,. \qquad (4.7)$$

In accordance with Kaiser & Guggenberger (2003), the exponential trend of Figure 4.10 b seems to confirm that OM sorption takes place preferably at specific reactive sites. When these sites (of the mineral phase) are occupied by OM, further addition of OM cannot interact with all the others available mineral sites which, in fact, are still accessible to N_2 giving contribution to the SSA. This could explain the observed offset (see Equation (4.6)), also considering the addition of PMS which has a SSA itself.

The microporosity of the samples, evaluated with the t-plot method, only in the low TOC content samples micropores contribute to the SSA values, although in a low amount. These micropores may be present in the clay minerals and clogged with the addition of PMS.

The *C* constant in the BET equation has been reported as an estimation of the coverage of the mineral surface by OM since N_2 adsorbs onto less polar organic surfaces more weakly than on mineral surfaces (Mayer, 1999; Kaiser & Guggenberger, 2003; Wagai et al., 2009), although it should be considered that when micropores are present in the inorganic matter the *C* parameter increases (Mayer & Xing, 2001). The group of samples with a low amount of TOC has *C* parameters above 100; the differences in the values are due to the relative abundance of micropores. On the other hand, samples group with high TOC content shows a *C* value in the 32-35 range (Figure 4.4). These values are similar to that observed for the PMS (*C* = 33) and to those reported in the literature for soils covered by OM (Kaiser & Guggenberger, 2003).

PSD in the 3-200 nm range have been obtained by the BJH method. Samples show a broad PSD of mesopores and small macropores, which are formed by the aggregation of

the clay particles (Figures 4.5). Large amounts of TOC cause a decrease of pores with a diameter below 10 nm (Figure 4.5, right). The same deviations previously reported for the SSA with respect to the TOC are observed in the PSD. Namely, the soil with the largest TOC, has a slightly larger pore volume for pores smaller than 30 nm.

4.3.4 ^{1}H-MRR results

The T_1 relaxation time curves of the five sieved sub-samples are quite well-defined monomodal curves. Figure 4.6 shows the $R_1(0)$ of the five sub-samples plotted versus the inverse of the particles grain diameter, computed by means of Eq. (4.3) on a plot of ln S(t) versus t (see as an example the inset in Fig. 4.6). ρ was estimated by means of Eq. (4.5), using a constant φ = 0.4, and its value is about 180 μms^{-1} on average. In general, this seems a high value for surface relaxivity, nonetheless values of this order of magnitude are reported in literature (Bryar et al. 2000). This value is also fully supported both by MIP experiment on the same samples (see Figure 4.7) and previous studies (Kleinberg, 1996).

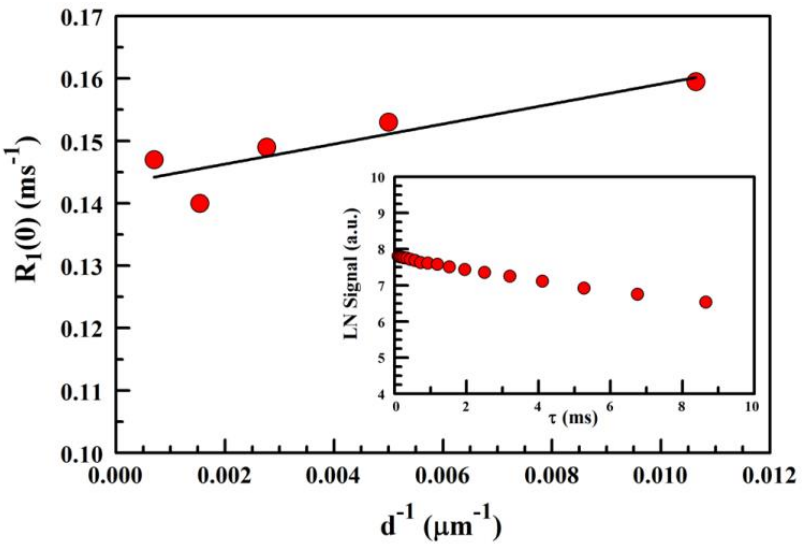

Figure 4.6 *Linear trend of $R_1(0)$ versus the inverse of grains mean diameters; by using Eq. (4.5) it is possible to deduce ρ_1 from the slope. The inset reports an example of a plot of the natural logarithm of the signal versus time, used to compute $R_1(0)$ of each sample; τ is the LAPSRSE inversion time. Only the first 10 ms have been considered in order to exploit the linear behaviour.*

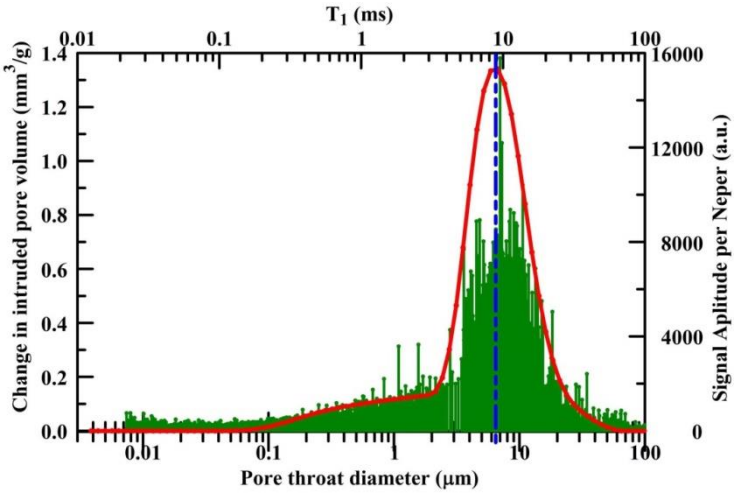

Figure 4.7. *In figure the pores throat distribution size curve obtained by MIP and T_1 distribution curve for a sample of pure soils are shown. The best overlap of the two curves is obtained by means of their convolution. The maximum overlap appear to be in correspondence of a throat diameter of 6.4 µm, that supposing to use a cylindrical model for pores, results in an effective relaxivity of about 178 µm/s. A value slightly high for a pure soil, but comparable with which obtained using the method described in in paragraph 4.2.6.*

In Figure 4.8a the solid line represents the sample SP1 in its original state, when it is saturated with 40% of water; the sample shows a peak of relaxation time of approximately 6-7 ms and a tail at longer times. After centrifugations, dashed line, the sample reaches a bimodal distribution, in part probably due to a partial gravimetric grain size redistribution (see international standards, ASTM D422), which leads to two distinct populations not in exchange between themselves, where the one at short times corresponds to the BWP.

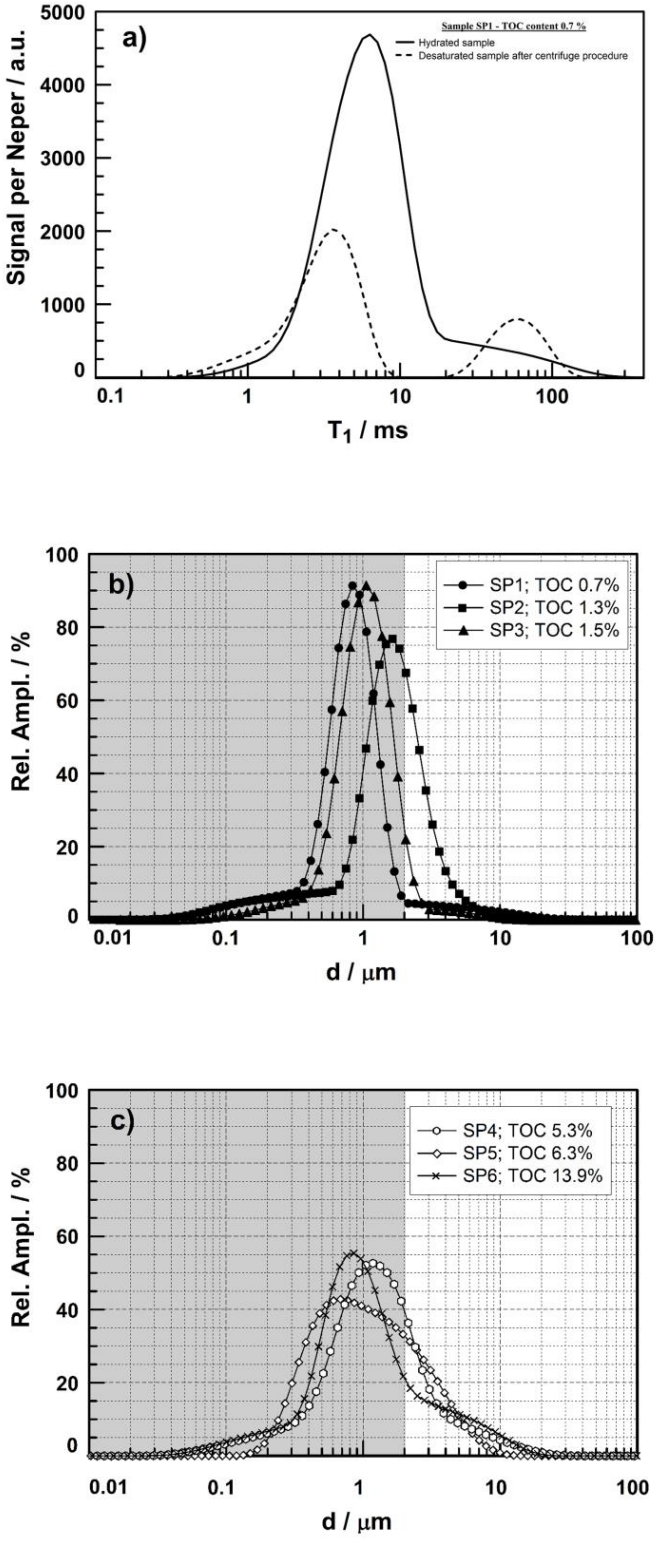

Figure 4.8. a) *T_1 distribution of the sample SP1, the solid line represents the hydration state and the dashed line the end of the centrifuge procedure, where it possible to appreciate the bimodal behaviour, in part probably due to the rearrangement of the solid phases. MRR PSD of samples with low TOC* (b) *and high TOC content* (c). *The dark grey part of the graph corresponds to the BWP domain.*

A T_1 cut-off value varying in the range between 10 and 20 ms, as the maximum relaxation time achievable by the water inside BWP, can be detected in all samples. This cut-off value is turned into a pore size as described before and it corresponds to a pore diameter of few micrometers. In such way we divided the whole T_1 distributions into FWP (which correspond to pores of diameter > 2 μm) and BWP (≤ 2 μm) (Figures 4.8 b, 4.8 c).

This choice is supported by the literature data on the MIP PSD of clayey soils in free saturation conditions (Della Vecchia & Romero, 2011), revealing an unique peak of 1-2 μm, that is also the upper limit size of free clay in natural soils (Fernández-Ugalde et al., 2013). This situation is in agreement with our soils samples if we consider how the presence of kaolinite clay, identified by XRD analyses, can influence the matrix structure of the samples (Della Vecchia & Romero, 2011), but at the same time it does not influence substantially the relaxation behavior of the samples, as it is a diamagnetic clay. Basically, samples with low TOC content (Figure 4.8 b), in hydration condition, show a single narrow peak around 6-9 ms, which corresponds to 1-2 μm. After centrifugation, FWP corresponds to 50-70 ms, that is 10-13 μm, and this is in agreement with the large pores visible in Figure 4.2c, and BWP are placed at 3-5 ms, that is 0.5-0.6 μm (data not shown). While samples with high TOC content (Figure 4.8 c), in hydration conditions, have a wider single peak which covers a range of two orders of magnitude in pore sizes (0.2-2 μm); in desaturation conditions the bimodal distribution is similar to those of samples with low TOC content, but with the BWP peak around 0.7-0.8 μm, which means a partial lack of small pores. The broadening of the hydration peak, with respect to low TOC group, is probably due to the water uptake by the solid OM phase, which causes the swelling effect of OM in saturation condition, implying an increase of the sample volume, (Schaumann et al., 2005). Swelling effects of clays is excluded since kaolinite is a non-swelling clay (Foster, 1954). FWP of high TOC content group seem likely to be between aggregates. Whereas the BWP may be related to the pores that are equal to or smaller than structural elements and which are less abundant in the samples with high TOC content. This distribution of porosity is observable also in SEM images (Figure 4.2).

The percentage of BWP decreases when TOC increases, in other words the decreasing quantity of water in BWP follows the TOC content increase. This trend is consistent with the decrease of SSA while TOC increases (Figure 4.10 b). As for N_2, these data may be well fitted to an exponential function (Figure 4.10 a). It is possible to justify the similar trend of MRR and N_2 results reasoning in terms of diffusion cells. MRR signal from BWP is averaged on local diffusion cells, which can be considered to be of a few tens of micrometers in dimension (Grunewald & Knight, 2009), but also on diffusion cells with pores of one or two order of magnitude smaller than 2 μm, that are the pores investigated by BET SSA. This is confirmed by MRR measurements of a progressive desaturation with a 40℃ oven temperature (Figure 4.9); the progressive drying of the sample leads to the vanishing in the T_1 distributions of high values and to the progressive appearance of shorter components (< 0.1 ms). This reflects less diffusion mixing between of water of adjacent pores of different sizes which might be partly empty. This reduction of the extension of diffusion cells reveals the presence of pores of approximately 10 nm. At the same time it is remarkable that OM dissolved components cover a range of dimensions, between 2-8000 nm (Mikutta & Mikutta, 2006), so they can exceed N_2 detectable macropores dimensions, but they can still have a reduction effect on BWP space. Namely, the presence of big OM components can reduce the volume of some BWP. This is consistent with the BWP exponential trend, confirming the idea that sorption of OM preferably takes place on specific mineral reactive sites, and it seems that further addition of OM persists on these same sites, reducing the volume of pores between 300 nm and 2 μm.

In brief, we can say that low TOC content samples have large SSA and *C* constant, short T_1 and higher signal from BWP, whereas high TOC content samples have an opposite set of MRR and N_2 adsorption/desorption parameters. The evaluation of these parameters could help to understand if OM is mineral associated, at pore dimensions < 2 μm (Chenu & Plante, 2006); this could be of great importance for understanding TOC turnover. It seems that in the high TOC group the reduction of pores and SSA, combined with the high pH, suggests the idea of formation of micro-aggregates where OM is protected by the clay

and silt fraction, together with the cementing action of $CaCO_3$ (Haynes & Nadu, 1998). In this case OM is hard to decompose. For the low TOC group it seems that OM degradation has successfully happened, as both SSA and BWP are accessible to N_2 and water, but pH levels are still high. This could mean a correct proportion in the mix of soil-PMS.

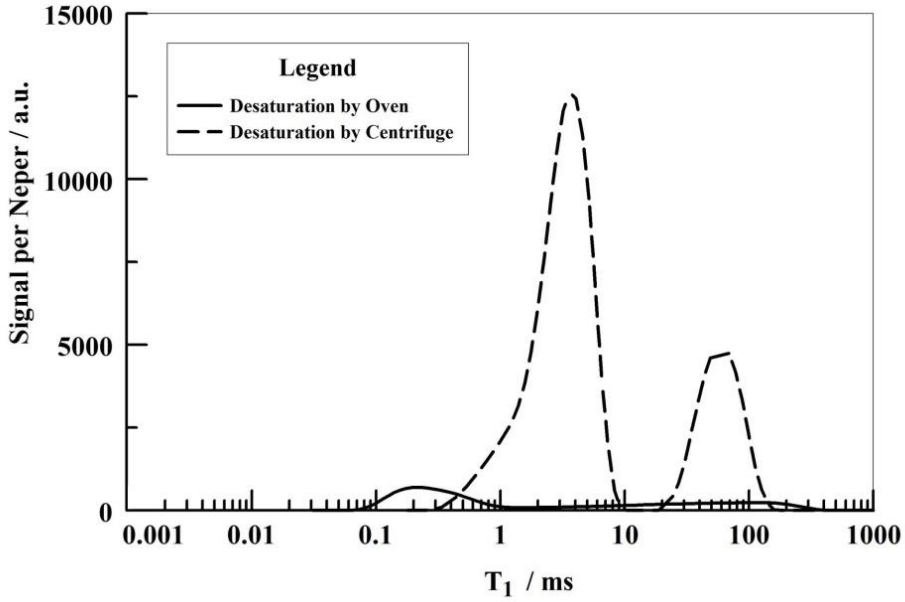

Figure 4.9 *Example of desaturation of the same sample by centrifugation and oven drying at 40°C. In the case of oven drying shorter relaxation times appear, due to the progressively desaturation of pores, this reflects less diffusion mixing between water of adjacent pores of different sizes which might be partly empty. Differences in the relative amplitude of the Signal per Neper may due to the different mass of the sample.*

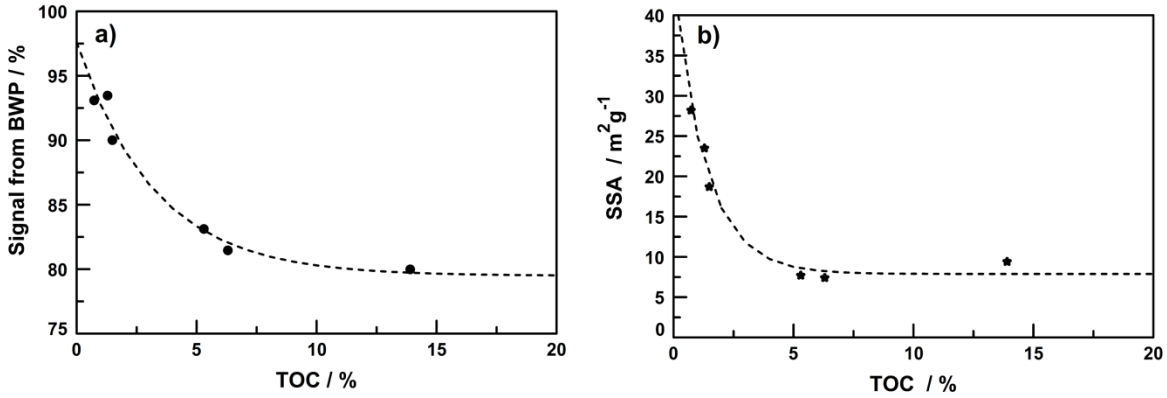

Figure 4.10. a) *Percent of MRR signal from BWP and* b) *SSA versus TOC content. Both data set are fitted to the function:* $y(TOC)=A*e^{(-k*TOC)}+offset$. *For BWT the fitted parameters are: A=18.10, k =0.31 and offset=79.5. Meanwhile for SSA: A=35.82 k=0.74 and offset=7.8.*

4.4 Conclusions

In summary, MRR data can be explained with the clogging effect of OM on soil pores. Generally it can be said that when TOC content is high, part of the original porosity measured, disappears. This is true for the MRR BWP and it is confirmed by N_2 adsorption techniques.

It is important to underline that the increase of TOC is associated with an increase of contaminant (in this case paper sludge), the latter can carry, not only additional OM, but also inorganic components that contribute to the total SSA and PSD.

MRR have been shown to be a valid tool, supported by other techniques, for both the monitoring of environmental remediation operations and for evaluating the evolution of the amended soil in the course of time. In fact they show evidence of the quality of the treatment adopted, revealing the proper or improper mixing and use of the waste components, to safe from possible environmental risks.

For this chapter thanks thank to Professor Fornasari G. and to Benito P. of the Industrial Chemistry department for BET, SEM and XRD measurements and to Professor Vassura I. and Ferroni L. of the CIRI energy and Environment labs (RN) for TOC measurements.

This work produced the publications:
Vannini, M, Bonoli, A, Bortolotti, V, Macini, P, Mesini E., Natural Soil Mixed With Paper Mill Sludge Characterization By 1H Nuclear Magnetic Resonance Longitudinal Relaxation Time, 2012, 3rd international conference on industrial and hazardous waste management, Crete, 2012.

Vannini M., Benito P., Bonoli A., Bortolotti V., Fornasari G., Macini P., Amended soils characterization by ^1H Nuclear Magnetic Resonance and N_2 adsorption/desorption Proceedings del XIV congresso nazionale di chimica dell'ambiente e dei beni culturali "La chimica nella società sostenibile", Rimini, 2-5/06/2013.

Bonoli A., Bortolotti V., Dall'Ara A., Macini P. & Vannini M.; Magnetic resonance analysis of carbon content in paper mill sludge–soil mixtures used in remediation practices International Journal of Environmental Science and Technology, DOI 10.1007/s13762-013-0431-9, 28/11/2013

Chapter 5

Organic waste for composting: an insight of the biodegradation process

5.1 Introduction

It can be estimated that one-third of worldwide food produced for human consumption is lost or wasted, entailing both a waste of energy and emissions of greenhouse gas. The production of food waste (hereinafter FW) covers all the food life cycle: from farming phase, up to both industrial manufacturing and processing, and retail and household (Mirabella et al., 2013). One of the best practice is to use wastes from one industrial sector as input for other industrial sectors, to minimize world wastes. One of the most used practice of reusing food residues is the production of compost. The collection and composting of organic waste from both households and industries has long been recognized as a valuable contribution to waste management. The first step towards a "zero-waste" concept, in particular in the food processing sector, is the identification, quantification and characterization of residue (Mirabella et al., 2013). For this reason, considerable efforts has been focused towards the definition of compost maturity in order to decide on the quality of a compost. Therefore the principal requirement of a compost for its safe use, e.g. in soil, is a high degree of maturity, which implies a stable OM content and the absence of phytotoxic compounds and plant or animal pathogens.

Over the last decades, research has been focused on the complex interaction between physical, chemical and biological factors that occur during composting. The control of parameters such as bulk density, porosity, particle size, nutrient content, Carbon to Nitrogen (C/N) ratio, temperature, pH, moisture and oxygen supply, have demonstrated to be key factors for composting optimisation because they influence the optimal microbial development and OM degradation (Bernal et al., 2009).

Generally, the degradation kinetic is accompanied by the development of a temperature profile that indicates the different phases of the process. The composting process evolves in three main phases: (i) an initial mesophilic phase, where mesophilic bacteria and fungi degrade compounds such as sugars, amino acids, proteins, etc., increasing quickly the temperature; (ii) a thermophilic phase, where fats, cellulose, hemicellulose and some lignin

are degraded; (iii) a cooling or maturing phase, characterized by a decrease of the microbial activity and, hence, of the temperature (Bernal et al., 2009).

Maturity is not described by a single property so it is best assessed by taking in account two or more parameters. Physical characteristics such as colour, odour and temperature give a general idea of the decomposition stage reached, but they give poor information on the degree of maturation. Also the C/N ratio, trend of C/N and pH during composting are usually analysed, but they don't form a complete set of standard criteria (Bernal et al., 2009).

MRR and MRI of hydrogen nuclei are optimal candidates to give information on the degree of degradation and maturity of compost, especially when there is needed a careful non-invasive and non-destructive characterization. Because many foods are proton-rich, e.g., from water, fat, carbohydrates, and proteins, MRR is a common tool to gain information about the composition and internal structure of foods, permitting also to monitor the compositional and structural modifications when they undergo natural or artificial processes. Since the relaxation times (longitudinal T_1 and transverse T_2) variations change the image contrast, MRI can easily monitor the structural changes in foods during processing and storage (Marcone et al., 2013). MRI can detect and show internal variations in the water content, as well as changes in water interaction with cellular tissues (Butz et al., 2005).

This is especially important for compost where the moisture has a role in structure changes, nutrient transport and heat conductivity.

Moisture content is usually assessed 'off-line' by dry weight measurements, which, however, does not differentiate the water available for microorganism activity from the water bound to the substrate unavailable to microorganisms (Bellon-Maurel et al., 2003).

Water is both produced by and required for microbial activity, as it is necessary to support the metabolic processes of the microbes. Water provides the medium for chemical reactions, transports nutrients, and allows the microorganisms to move about (Rynk, 1992).

The use of a moisture mass or volume ratio is a convenient and generally accepted method of describing the moisture status of materials, but as Miller (Miller, 1989) has pointed out, this approach provides only little insight into the availability of moisture.
However, consistent moisture prediction is still a challenging, as it depends on density and compost maturity (Agnew and Leonard, 2003).
In this work typical domestic food wastes have been reused as organic resources to produce compost for household. Typical MRR parameters as T_1 and T_2, and ^1H signal amplitude have been related to water content, and to micro and molecular structure of the compost, to follow the compost phases. Furthermore QRT has been used to measure locally the relaxation times by means of MRI images. An insight of compost components has been analyzed gaining information on some regions of interests. This technique allowed us to locally follow the FW biodegradation over time and to evaluate the maturity and quality parameters. In this first, but promising study, both techniques seem to well describe the stages of composting, as observed with other techniques, in addition giving information on local degradation of compost components.

5.2 Materials and methods

5.2.1 Samples

The compost analysed in this study was a mix of household organic waste with coffee grounds, fruits waste, food waste (bread, cheese and cereals) and loose grass (see Table 5.1), in proper percentages to obtain a C/N ratio around 25, which is an acceptable C/N ratio to obtain a good compost mix (Compost Maturity Index).
To obtain the percentages of Table 5.1, the Klickitat County calculator of the Washington state (www.KlickitatCounty.org) has been used.
A laboratory scale compost reactor (Figure 5.1) suitable for MRR measurements was created to both ensure oxygenation and immobility of the compost sample (as explained in paragraph 3.3.4); the last is essential to take MRI images over time (and therefore to

obtain QRT maps). Holes on the reactor surface ensure the oxygenation of the sample, which was provided using a laboratory extractor fan. Another identical reactor was used for temperature analyses.

Table 5.2 *Percetages of the domestic organic wastes used.*

Waste	***Percentage on the total mass (%)***
Fruit residues	78
Food residues	7
Loose grass	4
Coffee grounds	11

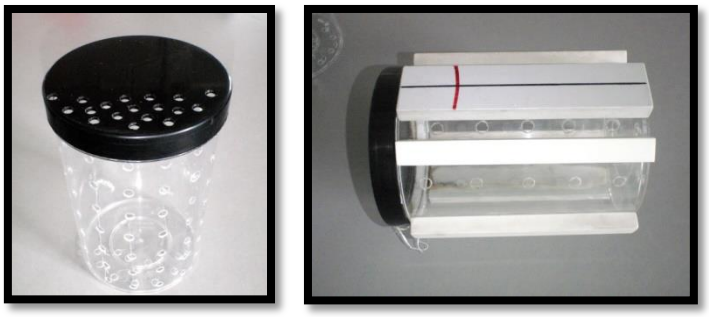

Figure 5.1 *Pictures of the reactor (d=10 cm, h= 13,5 cm) used for MRR/MRI and for temperature measurments. Right: notice the special supports to ensure the same position in the MRR/MRI coils during each measure and the holes to ensure oxygenation.*

5.2.2 Temperature and pH measurements

A mass of approximately 500 g of compost mix was stored, at room temperature conditions, in the dedicated reactor, to detect the sample temperature, using two temperature probes for the sample and one for the room temperature.

For pH analyses a standard procedure was adopted: a certain compost amount (a few grams) was mixed with a quantity of distilled water (1:5 w/w) and using a pH probe, pH was determined.

Both temperature and pH measurements were carried out over a period of time of two months starting from the formation of the compost mix. Measurements were roughly daily in the first two weeks, then they became less frequent as biodegradation changes slowed down.

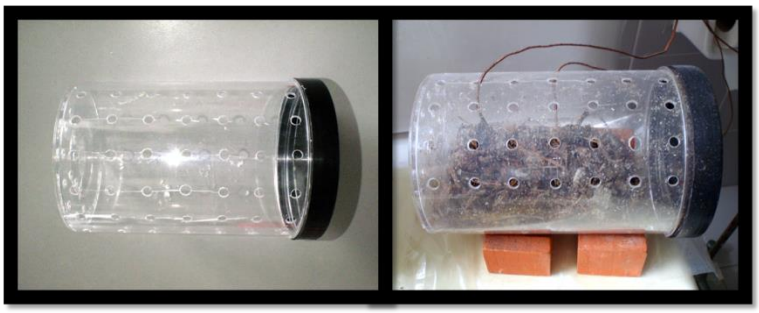

Figure 5.2 *Pictures of the temperature reactor (d=10 cm, h= 13,5 cm). Left: empty; right: with the compost sample and two probes inside the sample to detect temperature. Another temperature probe is outside the sample to monitor the room temperature.*

5.2.3 MRR and QRT measurements

A mass of the same compost, approximately equal (in laboratory conditions, oxygenation and room temperature) to the one used in temperature measurements, has been introduced in the reactor. This sample has been used for both MRR and QRT measurements.

MRR data were collected to obtain both T_1 and T_2 relaxation times distributions. The sequences used were SR for T_1 and CPMG for T_2. In the former, 64 Free Induction Decay signals log-spaced of 512 points were acquired, starting from 5 μs. Each scan was repeated 4 times in order to obtain a good S/V ratio. The measure was repeated for three different echo times: 100 ms, 250 ms, 500 ms. Each CPMG contained 3000 echoes and was repeated 4 times. For both SR and CPMG the duration of the 90˚ pulse was 60 μs. The repetition time was in all cases 4000 ms.

MRI measurements were performed at 30 °C by means of ARTOSCAN™ tomograph, corresponding to about 8 MHz for protons. A noteworthy aspect is that the low-magnetic

field instrument gives a relatively low signal-to-noise ratio, but it has the advantage of reducing the signal dephasing due to the distribution of magnetic fields within the sample, produced by the magnetic susceptibility differences between the matrix framework and the fluid in the pores. The quality of low-field MRI quantitative measurements was already confirmed previously (Borgia et al., 2001). In each MRI measurement, three axial sections of 5 mm were imaged; gap between slice of 0.2 mm; pixel size of 0.47×0.47 mm^2 were used. Depending on the signal to noise ratio, a number of excitations between 4 and 10 were used. QRT was performed both using Saturation Recovery (SR) to obtain a T_1 map and the Spin Echo (SE) sequences for the T_2 map. To create a map, a set of images was acquired, varying the inversion times in the case of SR and the echo times in the case of SE.

For T_2 maps, ten multislice SE sequences were acquired, using a fixed repetition time (TR=6000 ms) and a variable echo time (TE), from 10 ms to 3308 ms. For T_1 maps, eleven multislice SR sequences were used with fixed TE=12 ms, TR variable from 180 to 9160 ms and inversion time equispaced on the logarithmic scale from 10 ms up to 9000 ms.

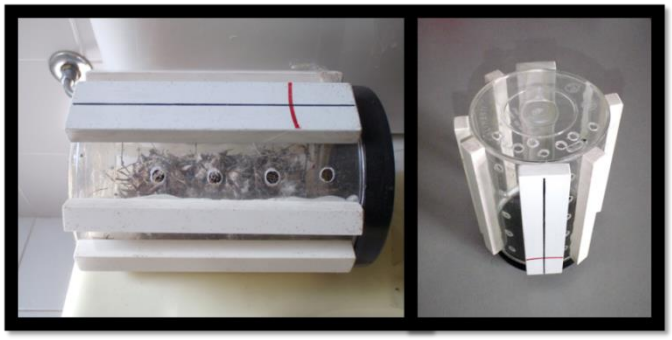

Figure 5.3 *Pictures of the NMR/MRI reactor (d=10 cm, h= 13,5 cm). Left: empty; with the compost inside.*

Relaxometry data have been processed using the in-house UpenWin (see paragraph 3.3.4). The weighted geometric mean ($T_{(1,2)g}$) was used as a characterizing parameter to summarize distributions. Images have been processed using the image analysis software ARTS (see paragraph 3.3.6).

5.3 Results and discussion

5.3.1 Temperature and pH

In the Figure 5.4 the registered temperature (orange squares) values during composting time and the reference room temperature (dotted line) are reported. The typical temperature trend during composting can be observed: an initial rise from ambient conditions, until the achievement of a maximum value, and then a slow return to lower values. The increase of temperature values of the last two data points is related to the increase of room temperature. In general temperatures did not increase over 30 ℃, which is quite normal in composting plants, where temperatures reach 70℃ (Sundberg et al., 2008). Such low temperatures are probably due to the dimensions of the laboratory-scale reactor and to the high degree of aeration, that was approximately of 200 m^3/h, which is an high aeration rate. As already observed by Sundberg et al., increasing the aeration increases both cooling and oxygen concentration, two process conditions that accelerate the increase of pH during composting and therefore resulting in an increase of the decomposition rate. In our sample, during the first week of composting, pH was around 4, followed by an increase up to values above 5. It is important to remark that the reactor conditions are basically different from the ones of industrial compost plants, which in general are completely open. The reactor has only approximately a 4% of free surface through which the air can move and the system is not agitated. These conditions, for this type of organic waste, have prevented the compost drying, obtaining an increase of pH towards basic values.

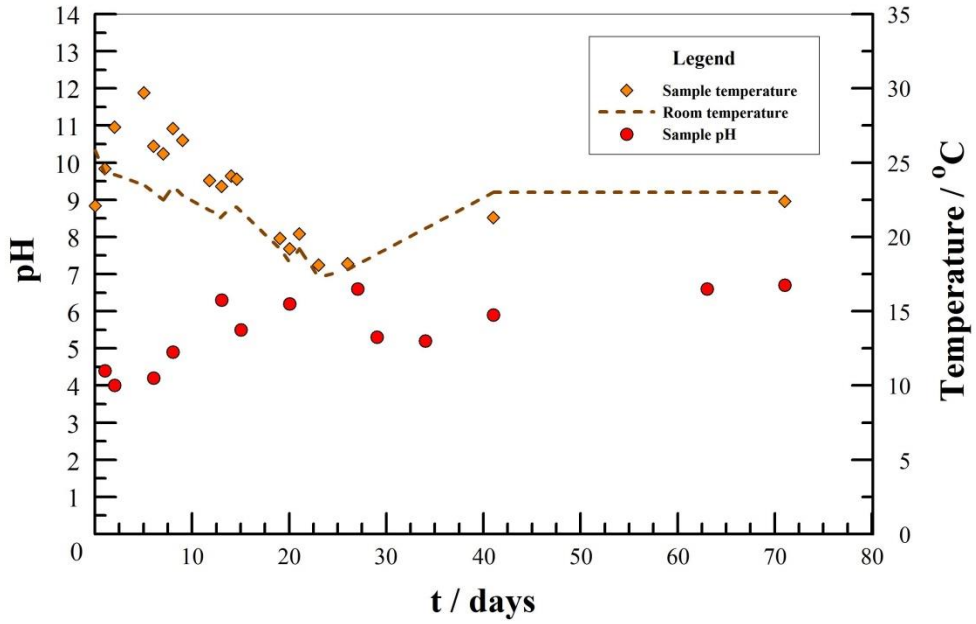

Figure 5.4 *Temperature and pH data vs the time of composting; for temperature both sample (orange squares) and room (---) data are represented, pH is represented with the (red circles) symbols.*

5.3.2 MRR

During the composting process all the T_1 and T_2 distributions were wide, from a few ms to a few seconds (Figure 5.5). Over the first days of composting both relaxation times gradually increased and then they slowly decreased. In Figure 5.6 T_{1g} and T_{2g} are plotted versus the observation time, it is possible to better appreciate the trend described above the relaxation times distributions. This trend appears similar to that of the temperature (Figure 5.4). The increase of relaxation times during the first stage of the degradation process is also due to the formation of new water released by the microbial activity. This new water is not strongly bound and therefore has longer relaxation times (Figure 5.5, 5.6).

Summarizing, during the first 6 days temperature increased, pH was acidic (≈4) (Figure 5.6) and an increase of both relaxation times appeared, probably due to the release of new free water and to the increase of temperature. During this first stage simple compounds were degraded and temperature started increasing.

Then it is possible to detect a stage during which temperature decreased, pH moved towards pH > 5 and relaxation times, after the achievement of their maximum values, started to decrease. During these stages the degradation rate is high, in fact a loss of over 40% of mass was measured in three weeks. This can be observed in Figure 5.7 where in the semi-log plots of the MRR signal intensity and mass loss are plotted: they both decrease but with different rate. This different trend is consistent because the loss of mass detects the loss of OM (by degradation), water (by evaporation) but not the presence of new water released. On the contrary MRR signal is due to the balance from the loss of water (by evaporation) and the presence of new water released. In particular in the plot of Figure 5.7 it is possible to appreciate a specific trend both for the MRR signal and the mass loss until the 19th day, with the difference in the slope due to the reasons above described, and a different trend both for MRR signal and the mass loss from the 19th to the 71th day of measure.

In general in composting processes it is preferable to identify a thermophilic phase with temperatures over 45℃, but in this laboratory-scale reactor no thermophilic phase has been detected, probably because of the high aeration rate which raised pH and decreased temperature. Nevertheless the degradation rate was anyway high (Sundberg et al., 2008).

After that, a cooling phase followed, during which approximately another 40 % of mass was lost in approximately 50 days. This can be explained with a dominance of the evaporation process while probably some components still present degradation behaviours (as it will be explained in the next paragraph).

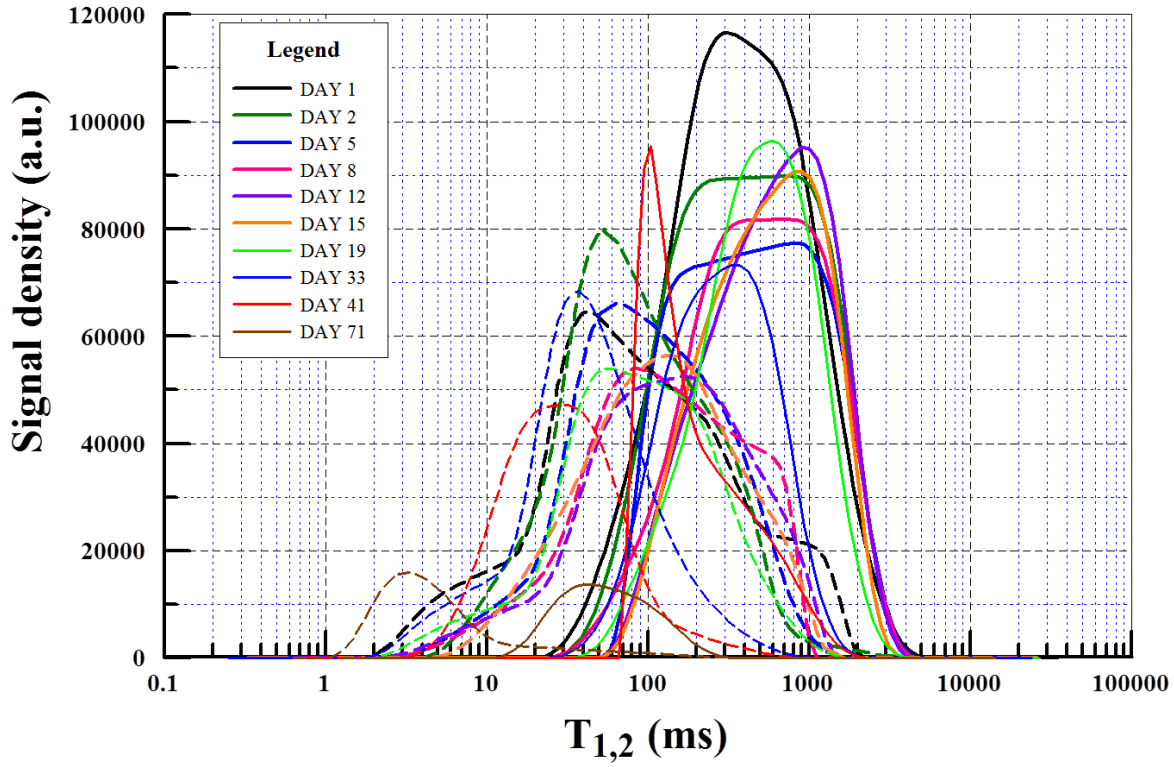

Figure 5.5 *$T_{1,2}$ distributions of the compost sample during composting time. Each color represents a different day, straight lines represent T_1 distributions, dotted lines represent T_2 distributions.*

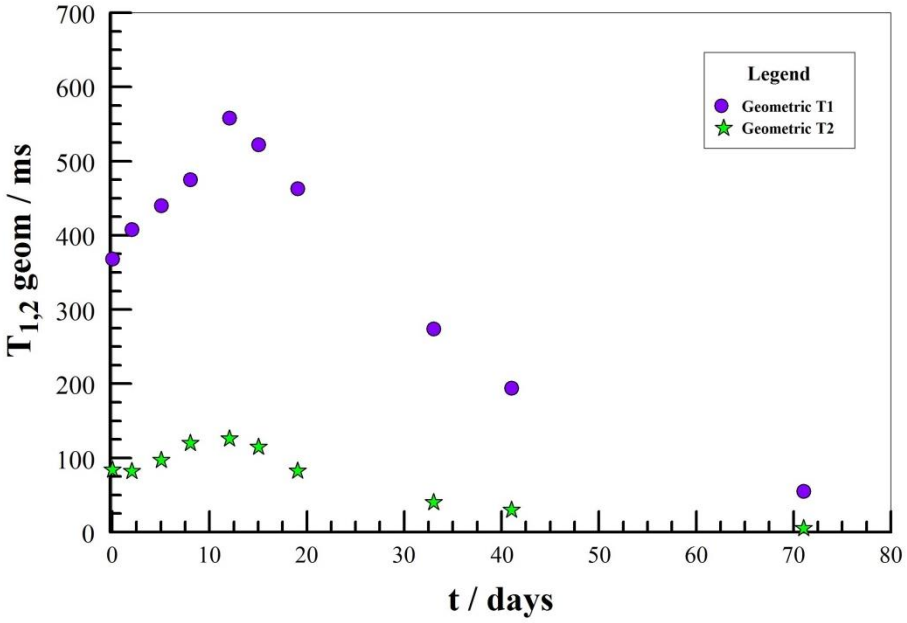

Figure 5.6 *$T_{(1,2)geom}$ during composting time, each point is the geometric mean time of the distribution.*

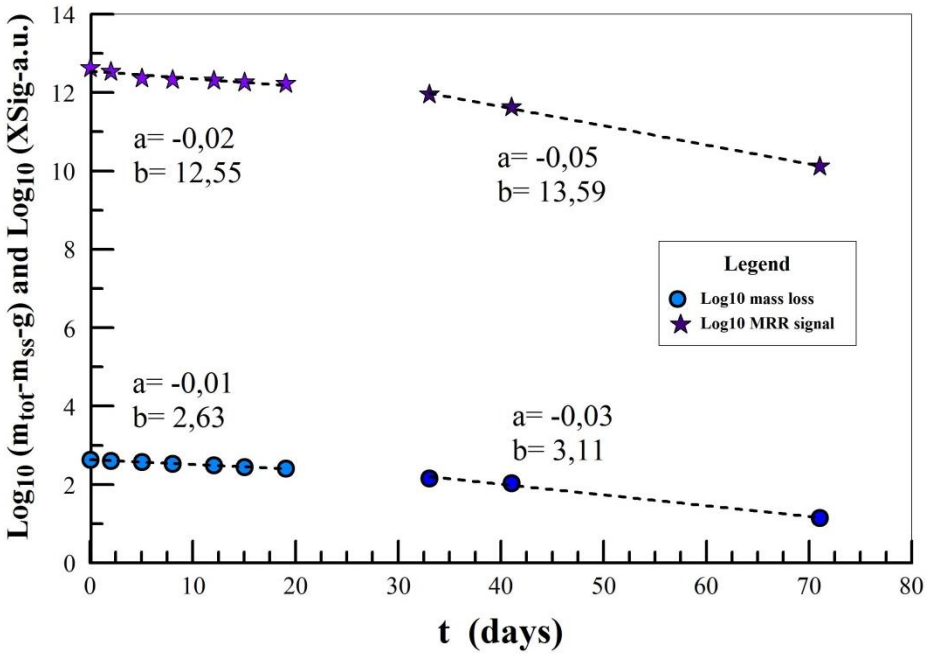

Figure 5.7 *Semi-logarithmic plot of the mass loss and the MRR signal intensity during composting time. The straight lines are the linear fit (y=ax+b) obtained on data until the 19th day of measure, in the first part of the plot, both for mass loss and MRR signal. (In this case the MRR signal is the one obtained only from saturation recovery measures. The one from CPMG has a similar trend, not shown). The same procedure has been applied also for the others 40 days of measurments.*

5.3.3 QRT

In Figure 5.8 T_1 maps obtained by QRT created during the composting time are shown, choosing only the days of measure number 1, 5, 8, 12, 15, 19, 33, 71. Thresholded T_1 images are shown, where different thresholds in the first and the second row are chosen in order to highlight the degradation phenomenon. In the first row only components longer then 700 ms are coloured. In the course of time, local degradation phenomena are acting and an extension of components with higher values of T_1 (on the order of 1-2 s) are revealed, likely meaning the release of free water by microbial activity. These phenomena happened immediately in few regions (detectable only with QRT and not with MRR) and then expanded until the twelfth day when a strong and global degradation was reached and relaxation times were uniformly high. This first stage of degradation lasted approximately

20 days, but slow degradation phenomena still acted, also during the cooling phase. Similar results have been obtained on T_2 maps (data not shown).

Relaxation times on QRT have been further evaluated choosing a ROI on each of the three slice acquired for every measure. The ROI selected over the all slice included all the sample, in order to evaluate a global relaxation time on the single slice. It is possible to notice (Figure 5.9, 5.10) that this T_1 and T_2 are different from the ones of MRR analyses since a slice is acquired on a small volume of the whole sample. In particular in the T_2 plot ROIs times are systematically lower because of the use of a SE for imaging instead of a CPMG. Nevertheless the trends T_1 and T_2 from the ROIs are in accordance with MRR.

In Figure 5.11 an evaluation of the T_1 of the compost components with long T_1 and shorter T_1 is shown. In figure 5.11 a) notice that when the composting process was just started, it is possible to individuate components with long T_1 (red circles), probably they are fruit waste, rich in water. The components highlighted with white circles have shorter relaxation times. Following the T_1 of the above mentioned components, it is possible to notice, compared to the geometric T_1 from MRR measurements, that they have different degradation periods, some of them have a fast degradation, other a slower degradation (Figure 5.11 b). It is possible to conclude that degradation is also a local process. In Figure 5.11 c) for the same components the signal amplitude is shown. It is evident that some components simply lose signal during the process; the others, after a stage of loss of signal, they gain it again. Then after the 19^{th} day they all lose signal. These observations highlight the fact that OM degradation is a complex process where the global degradation of a compost sample is a sum of many different kinetics inside it. In general it can be said that when relaxation times and signal amplitude both decrease the cooling phase is started and compost can be evaluated for reuse.

Hence QRT analysis well underlines the possibility of NMR technique to detect locally different kinetics rates, identifying components with fast and slow degradation phenomena. This local analysis helps to evaluate the readiness level and the quality of the compost.

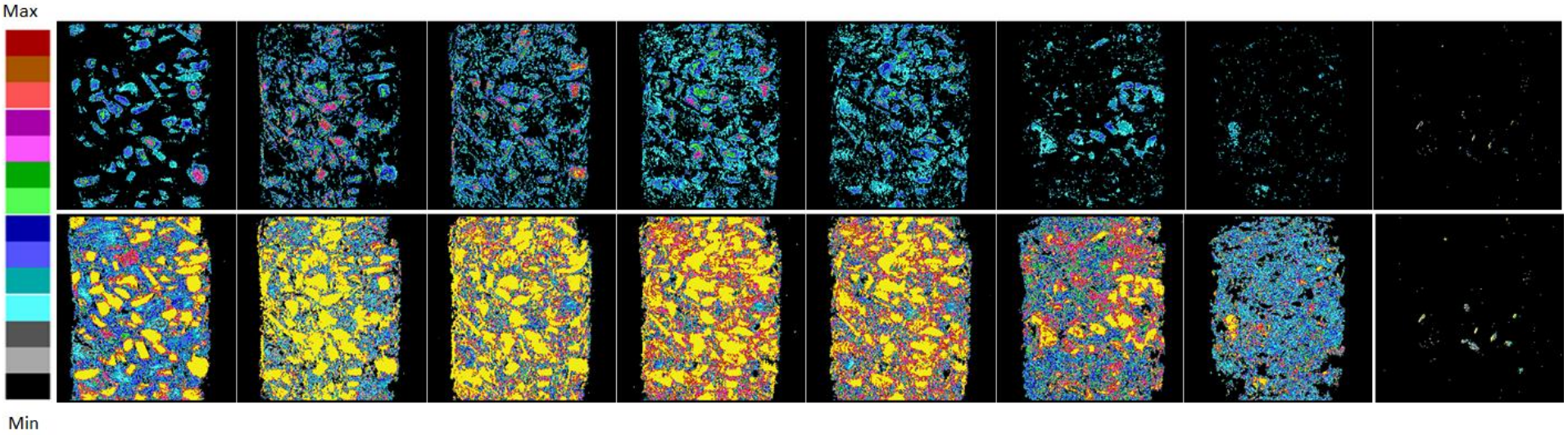

Figure 5.8 *Thresholded images. First row (a): 700 ms < T_1 < 3000 ms in the T_1 maps during composting time; second row (b): 50 ms < T_1 < 700 ms in the T_1 maps during composting time.*

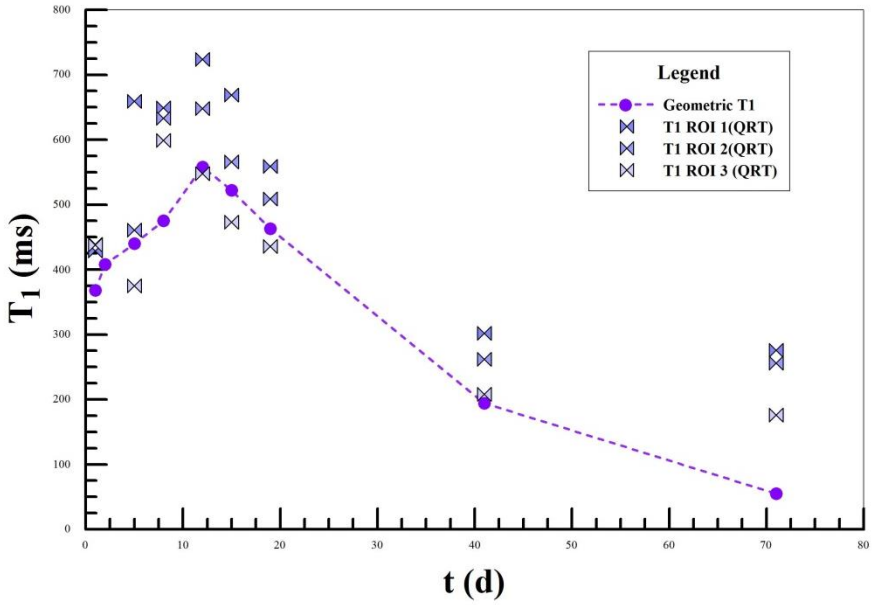

Figure 5.9 *Comparison between the geometric T_1 from MRR and the T_1 evaluated from a ROI of the whole slices. In particular for every day of measure it is plotted the T_1 of the three slices acquired on the compost sample.*

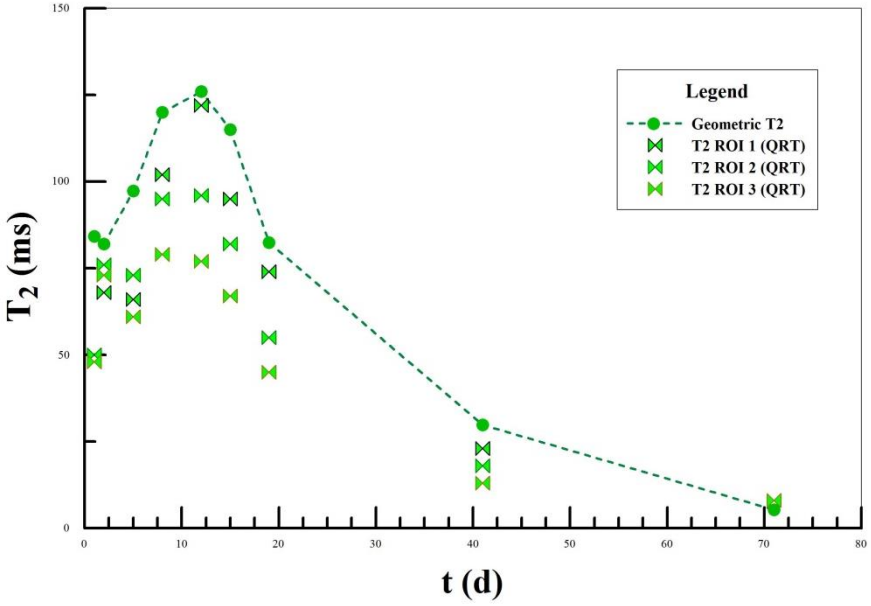

Figure 5.10 *Comparison between the geometric T_2 from MRR and the T_2 evaluated from a ROI of the whole slices. In particular for every day of measure it is plotted the T_2 of the three slices acquired on the compost sample.*

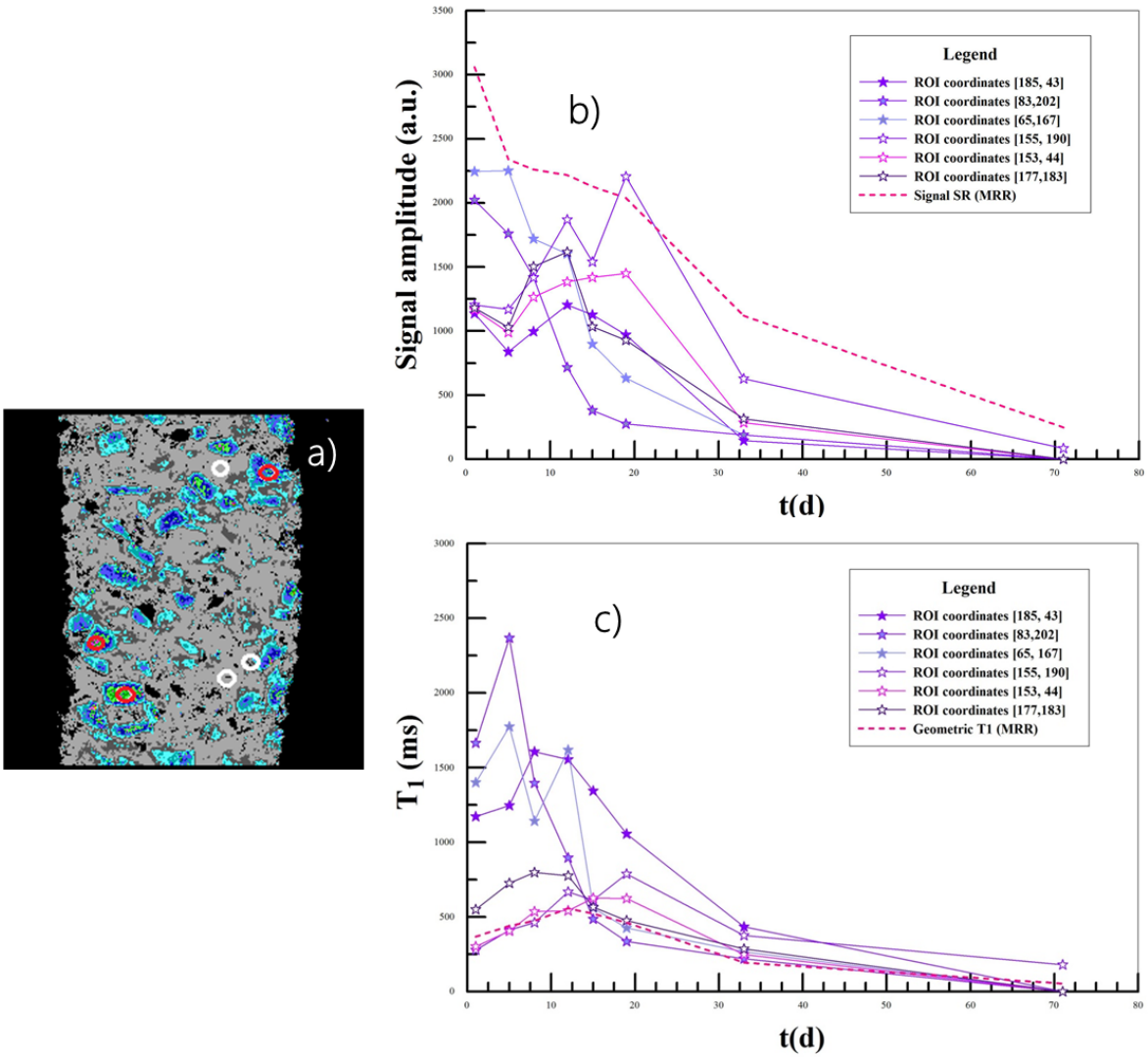

Figure 5.11 a) *Slice 1 at day 1, where circles indicates the ROIs evaluated. The red ones are components with long T_1 the first day of measure, the white ones with shorter T_1.* b) *Plot of the mean of T_1 for every ROI, full stars are red ROIs, empty stars are white ROIs. The dotted line is the geometric T_1 evaluated with MRR.* c) *Plot of the mean of signal amplitude for every ROI, full stars are red ROIs, empty stars are white ROIs. The dotted line is the signal from SR acquired with MRR.*

5.4 Conclusions

In summary, non-invasive and non-destructive MRR/MRI techniques can follow compost degradation globally, by means of the weighted geometric means of T_1 and T_2, showing a trend which is almost comparable to that of temperature. At the same time local information on degradation of compost is obtained by QRT maps, highlighting the presence of fast and slow degradation regions where specific components show their own particular behaviour.

Matching magnetic resonance techniques with other standard analyses (Temperature, pH, C/N) could be of great importance to fully describe the stages of composting and define the degree of compost maturity.

This work produced the publication:
M. Vannini, V. Bortolotti, L. Brizi, P. Fantazzini, E.M. Vasini, ***"1H Magnetic Resonance Relaxometry and Quantitative Relaxation Tomography characterization of food waste"*** *Conference Abstract Book of XII International Conference on the Applications of Magnetic Resonance in Food Science Maggio 2014, ISBN 978-88-902152-4-7*

Chapter 6

Further developments of the NMR techniques in the organic waste chain

As it has been proved in the previous chapters, NMR can be a powerful tool in the field of recycling organic waste, and to conclude this research thesis some further cases study, which are still in progress in the LAGIRN laboratory, are below discussed. This is an extension of the research work on organic waste since the examples reported are located at different stages of the organic waste chain. The first two experiments suggest NMR methods as tools to avoid food waste. The last case study is a MRR application to estimate the quality of valorised organic waste, the bio-oils, which are the products of the pyrolysis of biomass.

6.1 Dehydration of fruit to reduce fruit waste

6.1.1 The importance of reducing food waste

In the organic waste chain, since the emergency of gaining new sustainable life styles, not only recycling is important, but also reducing.

Reducing is the challenge of the first case study that follows. The most of organic waste comes from food waste. Food is a source of energy, but as already said, a lot of food is trashed when it is probably still eatable, so it is necessary to think when it is really a waste. In the food industry many techniques exist for few centuries to preserve the precious resource that food is; among these techniques, dehydration of food is largely known. This process is particularly common as a pre-treatment before air-drying or to obtain minimally processed fruit and vegetables products (Nowacka et al., 2014). In this way the shelf-life of fruit and vegetables is extended, without losing organoleptic properties. In most cases the osmodehydration, which is the dehydration obtained by means of a sucrose solution that surrounds the piece of fruit, inducing an osmotic reaction, is the technique employed to increase the product shelf life. Since by itself is not enough adequate, generally it is combined with other stronger stabilizing methods such as freezing or air-, freeze-,

vacuum-drying (Nowacka et al., 2014). Furthermore other techniques such as pulsed electric fields (PEF) could enhance the rate of osmotic dehydration, but they need to be further studied, to understand if its application can increase the efficiency of the dehydration process. In fact little is known about the consequences of this application on the water state of the cellular tissue. NMR relaxometry and imaging are optimal candidates to obtain information on the microstructure of fruit. By means of the quantification of T_1, T_2, and diffusion coefficient to obtain information about several processes and material properties (such as ice crystallization, and water mobility), the use of NMR methods are popular amongst a wide-range of fruits and vegetables (Marcone et al., 2013). MRI has already been applied on apples to study the process of ripening (Letal et al., 2003).

The aim of this still in progress work is to detect the effects of osmodehydration process with or without the application of PEF on apples in sucrose solutions. The analysis was performed after thawing (for frozen samples) and after rehydration (for the freeze-dried samples). In this study the Magnetic Resonance Imaging (MRI) was performed to assess the water distribution in apple tissue. In addition apples were analysed by the means of Differential Scanning Calorimetry (DSC). Further developments are directed to evaluate the best way to obtain dehydration fruits.

6.1.2 Apple osmodehyration results

TD-MRR data have been obtained with the CPMG sequence, on freeze dried samples. The fresh apple, the no-treated apple and the apple treated with increasing PEF pulses have been studied by means of T_2 distributions. Samples treated with PEF presented an increase of the signal from the peak at short times, which corresponds to the water with low mobility and a decrease of the area of the second peak which corresponds to the water with higher mobility. A possible explanation could be that PEF treatment may compromise the integration and continuous of the cell structure, thus the water in extracellular spaces

relaxed slowly, as water now is present in higher volumes which were created by the treatment process. The DCS results validate this explanation.

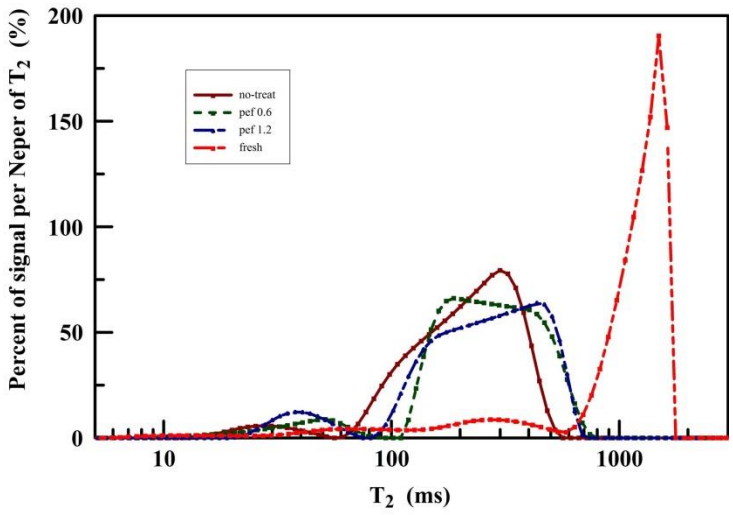

Figure 6.1 *Comparison of T_2 distributions for fresh, untreated and at different PEF pulses treated apple samples.*

Some preliminary results have been obtained also from MRI. First some preliminary images, acquired by Spin echo sequences, weighted in proton density, have been acquired to understand how image contrast gives information on the macrostructure of the fruit. On the basis of these images ripening can be evaluated (in Figure 6.2 on the left) following the colour scale to notice, where the fruit is more proton rich, for example dark blue parts have more hydrogens. Then preliminary maps have been acquired on cylindrical apple samples to have an insight of the water redistribution in the sample after one day in sucrose solution. Notice in Figure 6.2 centre and right different circles indicating different T_1 compartments.

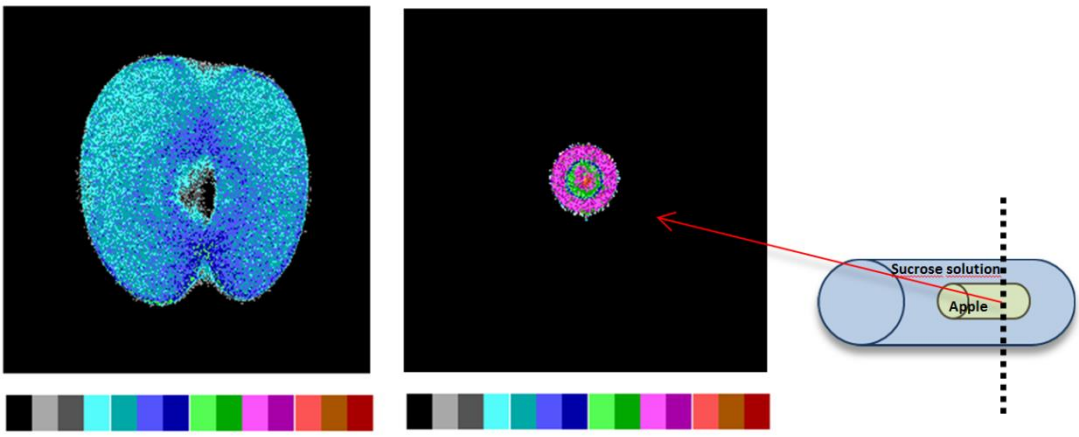

Figure 6.2 *Left: SE in proton density of a slice of a whole apple; the colours correspond to different hydrogen density, the black is zero hydrogen density, red is the maximum hydrogen density. Centre: slice of a cylindrical apple sample inside a test tube full of sucrose solution (sample volume: solution volume = 0,4), the schematization of the test tube with the sample is on the right.*

6.2 Applications of PERFIDI sequences on meat

6.2.1 Meat industry and its impact on food waste

Policy responses to the connections between food production, energy, climate, and health should include countering the world's rapidly increasing consumption of meat, which poses health risks by exacerbating climate change (McMicheal et al., 2007). So reducing or avoiding meat waste must be considered, to at least not make further non-sustainable the meat process production.

NMR technology has been applied and continues to be used on a wide range of different types of meats. Several NMR parameters can be associated with variations of water mobility as consequences of the mediations of water macromolecule interactions and changes in tissue structure, including T_1 and T_2 relaxation times, magnetization transfer ratio, and apparent diffusion coefficient (Marcone et al., 2013). The use of MRI permits the quantification of the above mentioned parameters, which has been used not only to determine chemical composition, muscle structure, and quality of meat, but also to study adipose tissue distribution, connective tissue, and muscle fiber type. These parameters

have been correlated with meat properties including pH, water-holding capacity, moisture, texture and sensory attributes (Marcone et al., 2013). In this work the PERFIDI sequences, whose potential in diagnostic medicine is already proved, have been employed to distinguish the different tissues of animal, in particular on meat samples. The contrast of PERFIDI images, combined with the T_1 distributions, can be used to detect the percentage of fat in the meat and to quantify the fat to water ratio. These analyses can be of support for quality controls, in order to avoid meat waste after commercialization of the meat products.

6.2.2 PERFIDI sequences for MRI results: validation and proof on meat

Applying the linear combinations for high-pass and low-pass filters it has been possible to obtain T_1 filtered images. In Figure 6.3 are represented the results of the validation tests on phantoms expressly created to obtain, inside two concentric cylinders, two distinct populations with relaxation times that differ of one-two order of magnitude. The images (in grey scale) of the axial section of the two cylindrical phantoms appear as two concentric circles (Figure 6.3). In Figure 6.3 a), the short relaxation time component, which is contained in the inner test tube, is completely filtered out in favor of the long relaxation time component. In the low-pass image represented in Figure 6.3 b) the situation is reversed: in this case, the signal of the inner test tube is not damped, while the rest of the sample signal is filtered out.

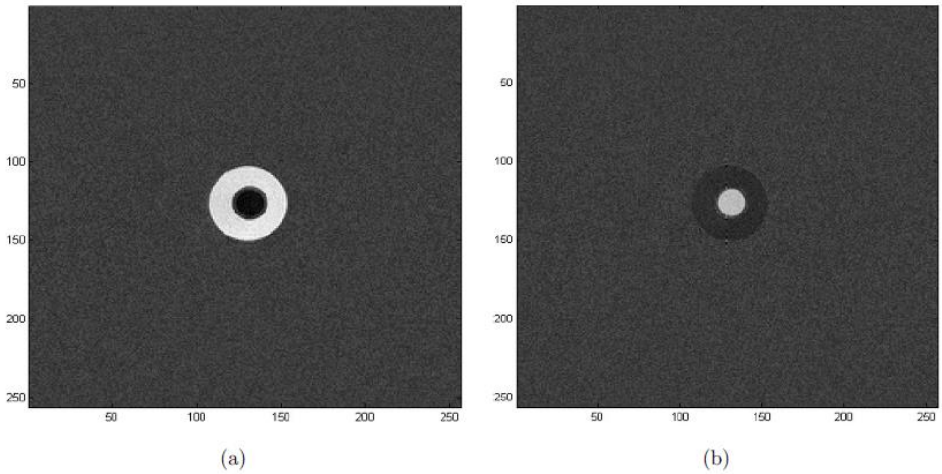

Figure 6.3 a) H*igh-pass experiment on the phantom made of two concentric cylindrical test tubes, only pixels in the external tube with longer T_1 are highlighted;* b) *low-pass experiment, only the pixels in the inner tube with shorter T_1 appear.*

The optimization of PERFIDI sequences was followed by a measurement of a meat sample (bacon sample). In Figure 6.4 a low-pass experiment is shown. Notice how the central part of the sample, which is mainly muscle, is bright, to the contrary fat in dark. These results seem promising for new developments on food waste.

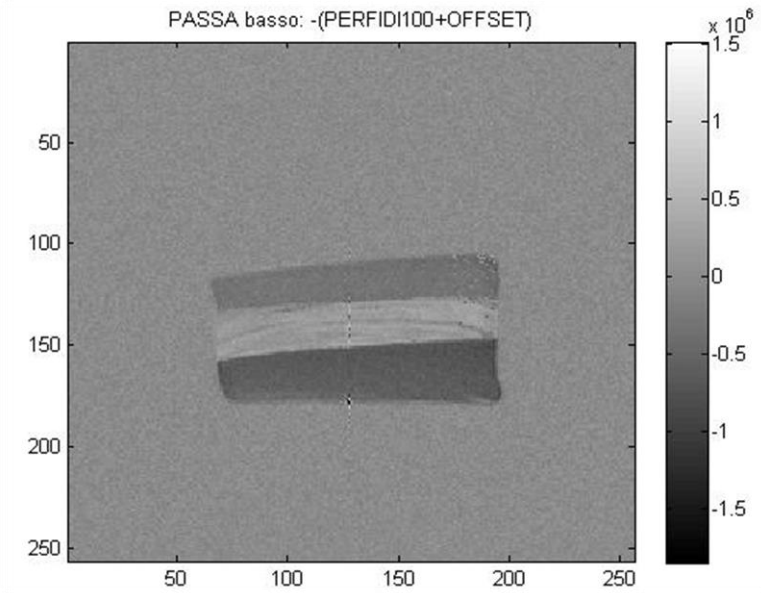

Figure 6.4 *Low pass experiment on a meat sample. Dark regions are fat tissue and the white region is muscle tissue. On the right there's the grey scale in arbitrary units.*

6.3 Evaluation of bio-oils quality

6.3.1 Bio-oil as biomass valorisation products

Bio-oils are dark brown, free-flowing organic liquids that are comprised of highly oxygenated compounds. They are the liquid products of the pyrolysis process. Pyrolysis liquids are formed by rapidly and simultaneously depolymerizing and fragmenting cellulose, hemicellulose, and lignin with a rapid increase in temperature. Chemically, bio-oil is a complex mixture of water, guaiacols, catecols, syringols, vanillins, furancarboxaldehydes, isoeugenol, pyrones, acetic acid, formic acid, and other carboxylic acids. It also contains other major groups of compounds, including hydroxyaldehydes, hydroxyketones, sugars, carboxylic acids, and phenolics.

Bio-oil is at present classified as a microemulsion in which the continuous phase is an aqueous solution of holocellulose decomposition products and small molecules from lignin decomposition. The continuous liquid phase stabilizes a discontinuous phase that is largely composed of pyrolytic lignin macromolecules. Microemulsion stabilization is achieved by hydrogen bonding and nanomicelle and micromicelle formation. The exact chemical nature of each bio-oil is dependent on the feedstock and the pyrolysis variables. The aging of bio-oil is observed as a viscosity increase. Some phase separation may also occur. This instability is believed to result from a breakdown in the stabilized microemulsion and to chemical reactions, which continue to proceed in the oil. Viscosity and water content can increase, whereas the volatility will decrease. In general the most important properties for bio-oils are appearance, miscibility, density, viscosity, distillation and ageing (Mohan et al., 2006).

Bio-oil applications are many: they can be used for heat production or electricity production, they have a big role in the production of "green hydorcarbons". New chemicals are produced from bio-oils, from the whole bio-oil or fractionated: wood preservatives, road de-icers, adhesives, liquid smoke, all environmentally friendly (Czernik & Bridgwater, 2004).

TD-NMR techniques, are at now innovative leaders in the emerging biofuel industry especially for optimization of new biofuels production processes (www.progression-systems.com). For this reason, the idea of this final case study, is to characterize bio-oils, in order to acquire a powerful on-line characterization method to find the better application of these products. The preliminary MRR results show that it is possible to distinguish between low and high quality bio-oils. Further developments would realize a model to detect the micro-emulsion components.

6.3.2 Bio-oil NMR distributions results

Preliminary TD-MRR measurements show that an high quality bio-oil and low quality bio-oil, where high and low is due to the different process of pyrolysis used, are extremely different, in relaxation times components (only T_2 are shown in Figure 6.5). An hypothesis high quality oils behave as micro-emulsion, whereas low quality probably not. What can be interesting in high quality bio-oils is to give the percentages of its components, such as pyrolitic lignin, water soluble and semi-volatiles. For this reason in Figure 6.6 four types of high quality bio-oils have been compared to typical water soluble and pyrolytic lignin distributions.

What has first appeared is that different high quality bio-oils have different distributions. High quality bio-oils named A, B and C are samples of the same pyrolytic process. High quality bio-oil named VTT1 has been obtained by another pyrolytic process (Figure 6.6). Anyway they have in common a component at long T_2, of the order of 80-100 ms, and a shorter component at short T_2, between 40 and 0.2 ms, which is an unique tail for high quality A, B and C, but it is a peak and a tail for high quality VTT1.

Furthermore notice that the component water soluble is composed by two peaks, one at 40 ms and the other of 100-200 ms, instead of pyrolytic lignin that is a wide distribution between 0.2 and 40 ms.

Further analyses are in progress to find the best model able to explain how these components act between themselves.

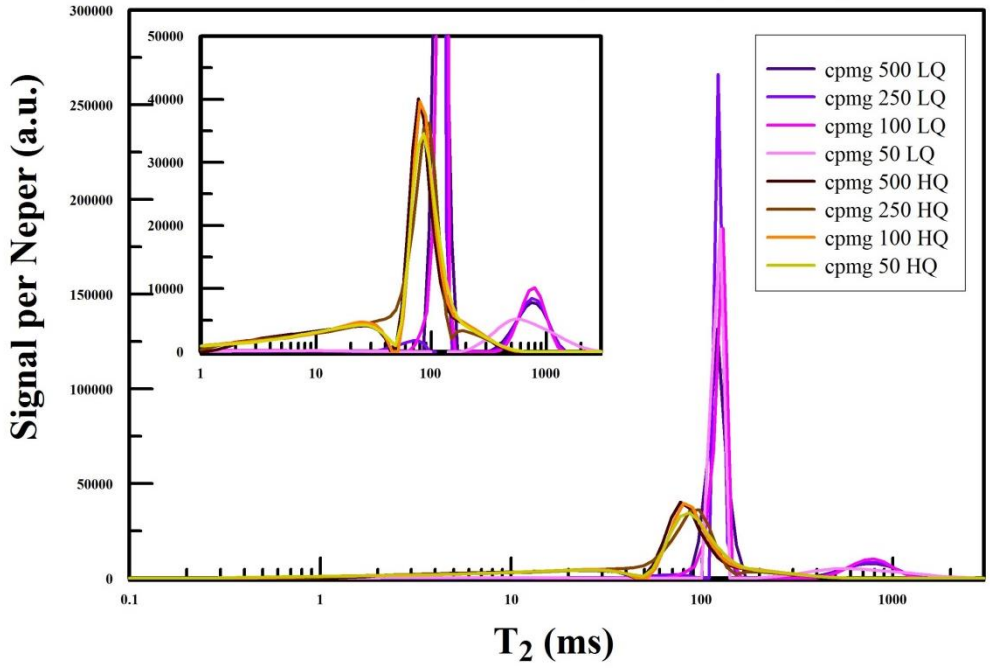

Figure 6.5 *Comparison of T_2 of high quality bio-oils and low quality bio-oil obtained at different time of echo. No significant diffusion effects are observed. It is instead clear that distributions of low quality are strongly different from the high quality ones.*

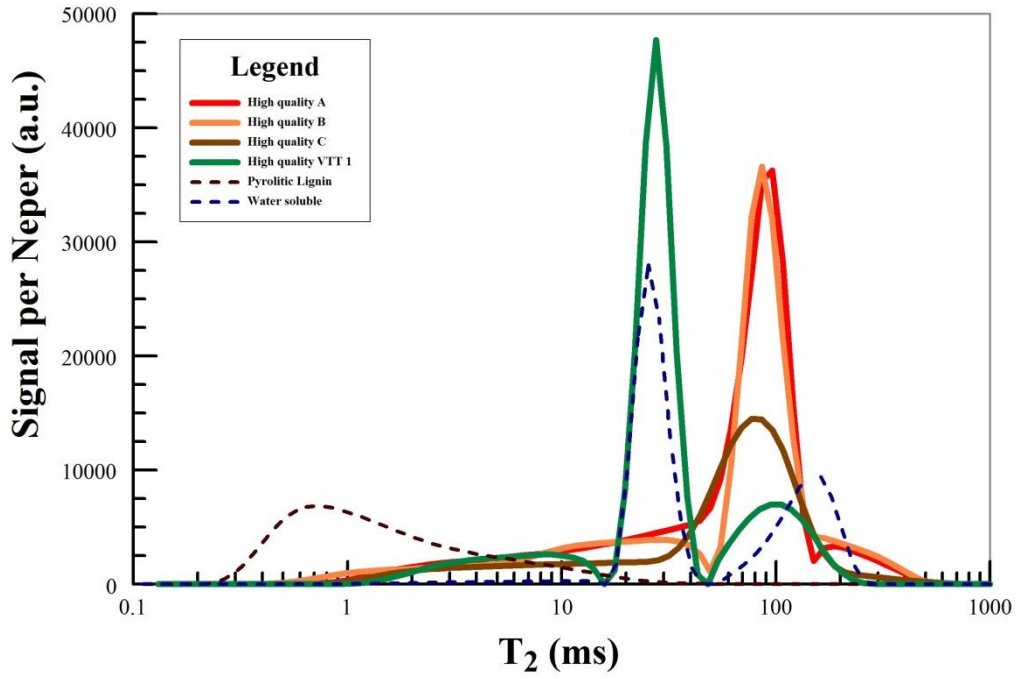

Figure 6.6 *High quality bio-oils are compared to the water soluble and pyrolytic sample alone. Notice the presence of a long component in all the samples between 40 and 100-200 ms and a short component under 40 ms, that in the case of VTT1 is formed by a peak and a tail.*

6.4 Summary

This studies, which are still in progress are a further demonstration of the potential power of the NMR techniques, especially in the field of food industry, and also in the food waste sector, where it is reaching an extraordinary importance. Preliminary results on apple dehydration and meat sample prove that the combined use of the NMR techniques, implementable in the LAGIRN lab, constitute a complete set for characterization of biological processes and structures.

Furthermore the application on waste valorisation products, such as bio-oils, confirm the utility of the NMR methods on all the waste chain.

For this chapter thanks to the CIRI agro-food laboratories and in particular to Tylewicz U. for measures on apple dehydration.
Thanks to CIRI energy and environment laboratories (RA) and in particular to Torri C. for measures on bio-oils.

This work produced the publications:

Tylewicz U., Aganovic K., Vannini M., Kiessling M., Toepfl S., Bortolotti V., Dalla Rosa M, Oey I., Heinz V. "Changes in water distribution induced by PEF treatment of apple" In Proceeding of the "School on applications of Pulsed Electric Fields for food processing – PEF School" p.154, Salerno, Italy, February 7-12, 2015. ISBN: 978-88-903261-9-6.

Balbi L, Bortolotti V, Brizi L, Fantazzini P, Greco D, Mariani M, Vannini M and Vasini EM, PERFIDI filters validation: from nuclear magnetic resonance relaxometry to magnetic resonance imaging, Journal of Mechanics in Medicine and Biology, 2015, Vol. 15, No. 5. DOI: 10.1142/S0219519415400187

Conclusions

NMR techniques represent nowadays non-invasive and non-destructive tools to study a large variety of samples in many scientific fields, from medicine to well-logging, but also in cultural heritage and in materials engineering. In this PhD thesis work, NMR shows its great potential also in the field of organic waste. The reasons that oriented this research on such kind of samples were many, but above all there is the need of achieving innovative scientific methods to characterize and valorise a precious resource such as organic waste. The today challenge is, in fact, to limit the negative impact on the environment, but also on our health, of a consuming world, driving it towards the ideal concept of a zero waste planet. This is probably only a kind of a dream, but, since waste can be considered a resource, why don't we try to reuse it in the best way? Technologies can have a great role in this challenge, and in particular we decided to improve the already known NMR methods, with the idea to create new approaches to analyse organic waste. This can help in the decision of the best way to reuse it.

First the LAGIRN NMR lab was adapted to be fully prepared to do organic waste characterization. Important results were obtained on the hardware equipment. So, for example, big capability radiofrequency coils have been reconfigured to host substantial amount of organic waste samples, that in most cases need to maintain a vertical position, because they are unconsolidated. The majority of the lab coils were tested and tuned, in order to obtain the best parameters for organic samples. A laboratory-scale bio-reactor was created to monitor samples biodegradation process over time. The software were updated: a new NMR pulse sequence (LAPSRSE) was created and successfully used on samples rich of paramagnetic impurities; a post-processing software was developed to deeper analyse relaxation times distributions and some of the software, already present in the lab, were optimized.

All these experimental tools proved their effectiveness in some specific studies concerning the second part of this research. First of all real soil samples treated with paper sludge, were analysed by MRR. The results showed the effect of the clogging of micropores (< 2 μm) at the increase of TOC content, as already observed in literature with other techniques. This effect is greatly relevant for future processes of the treated soil, because the pores clogging influences the soil properties.

Moreover the biodegradation of compost was fully characterized by both MRR and MRI. In particular the global and local biodegradation processes were analysed, proving that the whole composting process is a sum of different degradation kinetics. Relaxation times data demonstrated that the maturity phase of compost must be deeply evaluated, because of local processes that can alter again the compost stage. This analysis can support also the evaluation of the quality of the final compost product.

Finally other NMR experiments established the usefulness of the NMR characterization also to prevent organic waste. Analyses on osmodehydartion of apples are a first step to find the best way to preserve fruit, avoiding food waste. Similarly the use the innovative PERFIDI filters method, highlighted the possibility to analyse animal meat; also in this case NMR can support quality controls and help preventing waste. The last study concerned the characterization of bio-oils, which are one of the final product of the valorisation of biomasses. A good bio-oil avoids a lot of organic waste and can be reused in several fields. All this last experiments are still in progress.

The complexity of the NMR technique can be a problem for its extended use. Nevertheless the hard work done on the hardware and on the software and the creation of specific laboratory procedures to analyse organic waste, can make it easier, reducing the possibility to obtain misinterpretation of data.

Future works are especially oriented towards the study of organic resources (such as food) before they become waste, as reducing the excess of lost resources is a priority. So the application of NMR will be on quality controls, also to assess the origin of what is travelling

along a food chain. To do that, NMR equipment should be an on-line tool, in order to be employed directly inside the industries plants. Some examples already exist in the rest of the world. In Italy, where we have a huge agro-food heritage, unfortunately there is still much work to do.

APPENDIX A

AcqNMR parameters

STELAR Data File

Below there's an extract of a typical .sdf file generated by the software "AcqNMR" for NMR acquisitions. Some of the most important parameters are explained for clearly.

EXP: Sequence used for the experiment. It is possible to use both default sequences and new sequences created by the operator.

TEMP: It is necessary to register the room temperature. This parameter is only to keep information on the temperature of the laboratory, it is not used to implement the experiment.

F1: (KHz). It is a fine adjustment of the frequency of work. For every experiment this parameter has to be checked.

RFA: Attenuation: the higher the signal from the sample the higher the attenuation.

RD: (Recycle delay). It is the repetition time of the experiment, or the time needed before the repetition of the sequence and it is better to keep it 4 or 5 times the maximum T_1.

PW90: (μs). It is the duration of a 90˚degree pulse. The shorter the PW90 the more information from the sample. In fact if the duration of the PW90 is long, information from short components of the sample are lost (see the TATT parameter).

B1: (Gauss). Intensity of the B_1 field.

RPHS: phase of the experiment. As for F1, for every experiment this parameter needs to be checked.

MS: (Maximum Scans). How many times the experiment is repeated to gain a better signal-to-noise ratio.

BS: (Block size). How many points to acquire in the FID.

RINH and ACQD: together they form the dead time of the coil, RINH is the time which the ADC circuit is inhibited to protect itself from the spurious signals and ACQD is an added time to ensure that all components have disappeared before starting the new acquisition.

B0: (T) Estimation of the external permanent field.

NBLK: (Number of blocks) it is used only for staggered sequences (sequences where every block represent a FID or an echo) and it is the number of blocks acquired. For example an IR/S has a number of block which is the number of FIDs acquired over time, and every FID is formed by the BS multiplied by the points. All the experiment is repeated MS times.

EDLY: only for CPMG and SE sequences, it is the half of the time of echo.

TATT: (Total attenuation). It is the base transmitter attenuation which thus represents a pre-defined null level. The purpose of the TATT parameter is to adapt the transmitter input level to its opening threshold.

Further details are on the user manual of the Stelar console.

SDF file:

```
STELAR Data File

ZONE=   1
USER=   Stelar
OPER=   Marianna
SMPL=   Compost
EXP =   IR/S [DefaultSpmSequences.ssf]
EXPT=   0
TEMP=   23
F1  =   -2227
RFA =   47
GAIN=   1
RD  =   6
TAU =   6
T1MX=   1.5
BPOL=   7.616
BRLX=   7.616
BACQ=   7.616
HEAD=   Standard 10 mm
PW90=   60
B1  =   0.978665100803
PDMX=   P
DIOT=   2
FTM =   0
RPHS=   39
QPHC=   -90
PHCY=   Y
AFLT=   Y
NUC =   1H
SF  =   7.616
SYF1=   7613773
MS  =   4
DS  =   0
NS  =   4
BS  =   512
STIM=   0.0016896
SW  =   303030.30303
SWP =   39788.6427298
DW  =   3.3
RINH=   100
FLTR=   210000
ACQD=   32
RTIM=   6.82649927485
RFGN=   0.00446683592151
```

```
INST=   Spinmaster FFC
B0  =   0.178832014093
TATT=   20
PW  =   90 [p(x,-x,y,-y)]
P1  =   180 [p(x,x,y,y)]
ENDS=   Accumulation directives [p(x,-x,y,-y)]
D0  =   (RD) = 6
D1  =   (TAU) = 6
NBLK=   64
BACR=   TAU
BGRD=   LOG
BINI=   0.003
BEND=   (4*T1MX)
NGRP=   0
VFAC=   55.9680284642
XOFF=   0.000132
TDOM=   1
OUT1=   0
OUT2=   0
OUT3=   0
OUT4=   0
N1  =
N2  =
N3  =
N4  =
AUX1=
AUX2=
AUX3=
AUX4=
AUX5=
AUX6=
AUX7=
AUX8=
AUX9=
DATA=   0
-3483   438
-3492   413
-3505   383
-3542   390
-3557   371
-3551   383
-3567   395
-3561   369
-3573   367
-3550   337
-3568   340
-3583   319
-3591   318
-3589   283
-3582   297
-3582   323
-3594   292
-3544   304
.................
.................
.................
```

APPENDIX B

Upen output and display

Two output files are produced at the end of an UPEN run. The output file name stem is that of the input data file plus an additional character, which is chosen automatically on the basis of some parameters unless Filechar$. The output file name extension is .dat for several forms of the computed distribution and for the input decay and the extension is .tst for a text file with a list of non-default input parameters and the list of computed quantities.

.tst Files

A text file with a list of non-default input parameters and the list of computed quantities listed and described under "Display".

.dat Files

These are text files for spreadsheet or plotting programs and consist of eleven columns. The columns are T (relaxation time, with times equally spaced on a logarithmic scale), Sig_Np (amount of input signal per Neper, or factor of e, of relaxation time), Rate# (ordinal number of computed distribution value, starting at the lowest rate, or longest relaxation time), Pct_Np (percent of total extrapolated signal per Neper of relaxation time), Cum_Pct (percent of the total extrapolated signal having a longer relaxation time), SigT (signal, or data point, time: does not include points excluded by non-default values ND, Mint, Maxt), E:SNRxxxx (individual data point error of fit relative to the noise; xxxx is S/N), Sig (input signal, with Sinf, the computed or input value of the signal at infinite time subtracted unless SinfSbtr$="n"), SigCalc (the fitted signal, corresponding to the computed distribution of relaxation times), Range (two numbers: the shortest and longest data times), Zero (two zeros: the last two columns, two numbers each, are for easily placing marks of plotted distributions

Display

At each iteration the RESULTS part (second part) of the .tst file is shown on the screen above the plot. There are numerous items that appear only if they are relevant. We will go down the list of items that appear, or might appear if relevant. The name of the file being processed and the complete path and name of the output .dat file are given.

Next appears "_plt_" with a number to the left and another to the right. The number to the right is the program variable pltt (names referring to "plot"), which is the iteration number. The number to the left is the program variable plt which is the number of iterations since any reset.

Next is "_Change_", with a number on the left and one on the right. The number on the left is the percent change in error of fit for the last iteration. The number to the right is the largest fractional (not percent) change of any computed point relative to its amplitude-plus-noise since the last previous iteration. By watching these numbers one can see when the program is likely to finish.

Next is the SNR (signal-to-noise ratio), S/Rv = USig/RumV. "U" means unextrapolated and is the computed fit to the signal at the time of the first data point. RumV ("V" for Variation of local error of fit) is the noise value computed from errors of fit of second-nearest neighbors; it should be closer to the random noise, because slowly-varying errors of fit are suppressed. The SNR can be used in criteria given in UPEN-I for resolution of lines and line widths and also gives one measure of data quality.

If NN (Non-Negative constraint) is not being applied, Neg% is given; it is the integrated negative part of the computed distribution relative to the integrated total. If there are no sharp features to the computed distribution, Xneg% should be very small. Large values warrant careful review of all the diagnostics.

RmR is an important diagnostic, again with a number to the left and one to the right. The number to the left is RmR = Rrv = ln(Rum/RumV), which should normally be negative or at least not more than a few percent if positive, since the regression minimizes Rum, not RumV. To the right is RmR12 = ln(RumV1/RumV2), where RumV1 is the noise computed from errors of fit of the first Na (Number Averaged, 16 at present) pairs of nearest neighbours, and RumV2 from second- nearest neighbours. This is a measure of the alternation of the early data points about a smooth fit to the data. This is sometimes found even when only even echoes are used for T_2 data and sometimes even found in T_1 data. This is a common data problem, and it may not greatly affect the computed distribution if not excessive and if there are not large very short relaxation time components. A large RmR12 does, however, affect the statistics of the noise for the rest of the data range. The use of the first Na (= 16 at present) data midpoints instead of the points themselves does much to lessen this problem. The utility AvNa implements this. The quantity RumV (Rv), used in computing RmR, is noise computed from all pairs of second-nearest neighbors, where the contribution of a slowly- varying error of fit can often be

minimized. This parameter works best when there are closely- spaced data points. Positive values of more than a few percent usually indicate some data problems. That is, the data are not ideal in the sense of corresponding to random noise plus the sum of positive exponential components within the range of times covered by the data.

The item is "_Extrap_", with the number on the left giving the percent of the integrated signal extrapolated to times shorter than the first data time, and the number of the right giving the percent of the integrated signal extrapolated to times longer than the longest data time. UPEN gently suppresses extrapolation of a distribution beyond the range of the data. If SNR (Signal-to-Noise Ratio) and other factors are favorable, a distribution may be extended to shorter or longer times than covered by the data.

Then Beta00 is given, where beta00 is the compliance parameter, with higher values giving less smoothing of the computed distributions. In the program it begins as Beta000 (normally = 1) but may be increased from the keyboard (H) or decreased (h) in steps of factors of 21/2 or set to any desired value by keystroke (j) entry. Normally, values of beta00 much less than 1.0 give oversmoothing, and values much over 2.0 give undersmoothing, possibly giving more detail in the computed distribution than required by the data.

The number to the left of the next entry, "_BusyMMod_" , gives a measure of the sharpness and amount of detail; the number on the right is a measure of multimodality.

AvNa appears if AvNa has been called, either automatically or by being specified by AvNa$= "y". The following number is the Rum12 value before AvNa was called. Tlong is the relaxation time for which 3% of the signal is longer, the longest significant relaxation time. If (without NN) there is a negative peak at long times, this counts negatively towards the cumulative 3%.

Then, there is a list of interpolated times of the Peaks. Next, if there are resolved peaks, is Resolved_Peaks_Tgm and the geometric-mean (g-m) times and signal fractions of the resolved peaks. See the control parameter VALLEY, which controls how low the floor of the valley between a pair of peaks must be for the peaks to qualify as resolved. The parameter ValleyMx is the longest relaxation time that is used in computing the g-m time of the longest peak.

The entry RumNewOld has a number to the left and one to the right. The value of RmR12o before application of AvNa is printed with "AvNa" if AvNa has been implemented. The number to the left of RumNewOld is ln(Rum/Rumo); the number to the right is ln(RumV/RumVo).

To the left of _gmTra_ is the geometric-mean relaxation time of the computed distribution of relaxation times, and to the right is the rate-average time. If the CONVERGE utility has been called, CONVERGE is printed.

If AbsValue has been implemented, "AbsValue:asymp=" appears. The first number is the asymptote chosen by the program. The second number is the number of data points useful in determining the asymptote. The third number is Sinfld, the "old" value of Sinf (signal at infinite time), the value before applying AbsValue.

Three signal values are given around the printed "_XSigU_" . X means extrapolated to zero time; U means unextrapolated, that is, the fitted curve evaluated at the time of the first data point; the third is the difference between the first and last points, which is independent of the processing. If Sinf is input (for instance, = 0 for CPMG with phase cycling) Sinf is substituted for the last point.

Rum - Sinf The rms error of fit Rum is the number to the left of "_Rum_" ; RumV,

the estimated noise level, is to the right. Then Sinf is given. If Sinf is computed for CPMG data (instead of being set to 0 or some other value), its value should be compared to the noise value, RumV. If it is comparable to RumV, the possibility of absolute-value data should be considered.

Upen Parameters

Most Adjusted

FileChr$

The output files (.dat and .tst) use the file name stem, plus one added character that permits computation for several choices of parameters, including some automatic choices based on some of the input control parameters, without overwriting previously-computed outputs.

NNN$ MN$

No Non-Negative constraint. The data for many, but not all, relaxation time distributions have physical reasons for the distribution to be non-negative. The NN constraint can be lifted for exceptional cases or to investigate aspects of data quality also adjustable from the keyboard during computation.

Controls the choice of whether Sinf, the value of the fitted signal at infinite time, is included as a regression variable (not adjustable from the keyboard during computation). Permitted input values: " " for auto, (from certain preprocessing only) the program decides automatically, , MN=1 for T1 data and MN=0 for T2 data;

"n" for no; "y" for yes; "i" a value of Sinf is request of the user.

AvNa$ beta000

("Av" for "average"; "Na" for "Number averaged") It is possible to use the first Na (normally =16) midpoints of successive signal pairs instead of the signals themselves. This is to mitigate the effects of instrument adjustment problems that lead to the alternation of early data points about any smooth fit. It can be set to be on or off or to be called automatically when the problem is detected (not adjustable from the keyboard during computation). Permitted input values: "n" for no; "y" for yes; " " automatic (when RmR12 is high (>.05) uses the first Na midpoints).

This controls the starting value of a compliance parameter beta00, where larger values of beta00 (also adjustable from the keyboard during computation, see "Keyboard Input") allow more detail (not necessarily valid) in the computed fit. Default value: "1" (should usually not be more than 2).

AbsVal0$

This allows a number of options when absolute-value ("Modulus") data are being processed (not adjustable from the keyboard during computation). There is a wide range of data conditions and data problems. Permitted input values: " " for no (default); "y" for yes; "i" a value for the absolute-value asymptote (asym) is requested of the user; "a" for auto, if Sinf is positive and comparable to RumV treats data as absolute-value data; "b" as "a" but the final computation will be done disenabling Sinf regression; "c" as "b" but asym is evaluated from the single-channel noise; "d" as "y" but asym is evaluated from the single-channel noise; "e" as "d" but asks the user for an estimated baseline input (avblc).

MI

The number of logarithmically-spaced output relaxation times for which the distribution of relaxation times is computed (not adjustable from the keyboard during computation). MI is often about 100, but in some cases good data with sharp features can be improved by more points (and more computation time). Default value: "100".

MINimum t, where t is data time (as opposed to relaxation time, T). Data points with t<Mint are discarded in the computation (not adjustable from the keyboard during computation). Must be well under TE/D for windowed CPMG data. Default value: "0".

MAXimum t. Data points with t>Maxt are discarded in the computation (not adjustable from the keyboard during computation). Default value: "0".

Error-MaXimum. Some data sets may have points with "spike" noise, that is, a few points differing from an intermediate fit by more than the level of Gaussian random noise. These points can be automatically downweighted (not adjustable from the keyboard during computation).

Further information: http://software.dicam.unibo.it/upenwin

APPENDIX C

ARTS parameters

MAX e MIN: These are the minimum and maximum values of the signal (or of the T1 or T2 for QRT maps) to display the image. The signal is spread in the range of values between these two limits.

FITTING: Function used to create QRT maps. It makes a fit of n images acquired with different inversion or echo times.

FILTRI: Different filters, based on noise reduction, can be applied to improve the image quality.

ROI: The button ROI permits to create a region of interest, rectangular or circular with dimensions chosen by the user, inside the image. In this region quantitative information on signal amplitude or times can be obtained.

M: It gives the mean values of a ROI or the value of a single pixel selected.

ISTO: It creates the histogram of the image or of a ROI.

Cu: It calculates the cumulative curve of the pixels.

Dif: It makes the difference of two images.

Fu: It makes the fusion between two images.

Gr: It calculates the gradients maps, giving an edge detection as result.

Bibliography

- ✓ Adani F, I processi aerobici per il trattamento di rifiuti urbani. *Quaderni di Ingegneria Ambientale*, 2004, Cipa Srl, Milano.
- ✓ Agnew JM and Leonard JJ, The Physical Properties of Compost, *Compost Science & Utilization*, 2003, **11**, 238-264.
- ✓ Aringhieri R, Nanoporosity characteristics of some natural clay minerals and soils. *Clays and Clay Minerals*, 2004, **52**, 700–704.
- ✓ Assocarta, *Rapporto Ambientale dell'industria cartaria italiana (dati 2009–2010)*, 2012, published in http://www.assocarta.it/it/ pubblicazioni.html.
- ✓ Balbi L, Bortolotti V, Brizi L, Fantazzini P, Greco D, Mariani M, Vannini M and Vasini EM, PERFIDI filters validation: from nuclear magnetic resonance relaxometry to magnetic resonance imaging, Journal of Mechanics in Medicine and Biology, 2015, Vol. 15, No. 5. DOI: 10.1142/S0219519415400187
- ✓ Bayer JV, Jaeger F, Schaumann GE Proton nuclear magnetic resonance (NMR) relaxometry in soil science applications. *Open Magnetic Resonance*, 2010, J 3:15–26.
- ✓ BCFN, Food waste: causes, impacts and proposals, *Barilla centre food & nutrition*, 2012
- ✓ Becker E, A brief history of nuclear magnetic resonance, *Analytical chemistry*, 1993, &% (5), 295A-302A.
- ✓ Bellon-Maurel V, Orliac O and Christen P, Sensors and measurements in solid state fermentation: a review, *Process Biochem.*, 2003, **38** (6), 881-896.
- ✓ Bernal MP, Alburquerque JA and Moral R, Composting of animal manures and chemical criteria for compost maturity assessment. A review., *Bioresour. Technol.*, 2009, **100** (22), 5444-5453.
- ✓ Beauchamp CJ, Charest MH and Gosselin A, Examination of environmental quality of raw and composting de-inking paper sludge. *Chemosphere*, 2002, **46**, 887–895.
- ✓ Bernstein MA, King KF, Zhou XJ, Handbook of MRI, Pulse Sequence, 2004, Elsevier Academic Press.
- ✓ Beven K and Germann P, Macropores and water flow in soils revisited, *Water Resources Research*, 2013, **49** (6), 3071–3092.

- ✓ Borgia GC, Bortolotti V, Fantazzini P, Changes of the local pore space structure quantified in heterogeneous porous media by ^{1}H magnetic resonance relaxation tomography, *Journal of Applied Physics*, 2001, 90 (3), 1155-1163.
- ✓ Borgia GC, Palmonari C, Fantazzini P and Timellini G, Ceramic microstructure detected by NMR relaxation and imaging of fluids in the pores. *Magnetic Resonance Imaging*, 1996, **14**, 899–901.
- ✓ Borgia GC, Bortolotti V, Brown RJS, Fantazzini P, A robust method for calculating geometric mean times from multiexponential relaxation data, using only a few data points and only a few elementary operations. *Magn Reson Imaging*, 1996, 14, 895–897.
- ✓ Bortolotti V, Brown RJS and Fantazzini P, UpenWin: a software to invert multi-exponential relaxation decay data. Distributed by the University of Bologna, 2009, villiam.bortolotti@unibo.it.
- ✓ Bortolotti V, Fantazzini P, Gombia M, Greco D, Rinaldin G, Sykora S, PERFIDI filters to suppress and/or quantify relaxation time components in multi-component systems: An example for fat–water systems, *J Magn Reson*, 2010, 206:219–226.
- ✓ Bronick CJ and Lal R, Soil structure and management: a review. *Geoderma*, 2005, **124**, 3–22.
- ✓ P. Butz C, Hofmann and Tauscher B, Recent Developments in Noninvasive Techniques for Fresh Fruit and Vegetable Internal Quality Analysis, *Journal of Food Science*, 2005, **70**, R131–R141.
- ✓ Cabrera F, De Arambarri P, Madrid L, Toca CG, Desorption of phosphate from iron oxides in relation to equilibrium pH and porosity. *Geoderma*, 1981, **26**, 203–216.
- ✓ Chenu C, Plante AF, Clay-sized organo-mineral complexes in a cultivation chronosequence: revisiting the concept of the "primary organo-mineral complex". *European Journal of Soil Science*, 2006, **57** (4), 596-607.
- ✓ Coates GR, Xiao L, Prammer MG, NMR logging—principles and applications, 1999, Gulf Publishing Company, Halliburton Energy Services Publication, Houston, TX
- ✓ Cornell RM and Schwertmann U, *The iron oxides. Structure, properties, reactions, occurrences and uses*, 1996, Wiley-VCH, Weinheim.

- ✓ Czernik S and Bridgwater AV, Overview of Applications of Biomass Fast Pyrolysis Oil, *Energy & Fuels*, 2004, 18 (12), 590-598.
- ✓ De Jonge H and Mittelmeijer-Hazeleger MC, Adsorption of CO_2 and N_2 on soil organic matter: nature of porosity, surface area, and diffusion mechanisms. *Environmental Science & Technology*, 1996, **30,** 408–413.
- ✓ Della Vecchia G, Jommi C and Romero E, An insight into the water retention properties of compacted clayey soils. *Géotechnique*, 2011, **61**(4), 313–328.
- ✓ Dunn KJ, Bergamann DJ and LaTorraca GA, *Nuclear magnetic resonance petrophysical and logging applications*. In: Helbig K., Treitel S. (eds) Handbook of geophysical exploration, seismic exploration. 2002, vol 32, Pergamon Press, London, p 583.
- ✓ Echeverria J C, Garrido J J, Morera MT and Mazkiara C, Characterization of the porous structure of soils : adsorption of Nitrogen (77 K) and Carbon Dioxide (273 K), and mercury porosimetry. *European Journal of Soil Science*, 1999, **4**, 497–503.
- ✓ Ellis DW, Singer JM, Well-logging for earth scientists, Published by Springer, 2008.
- ✓ Farrar TC, Becker ED, Pulse and Fourier transform NMR. Introduction to theory and methods, 1971, Acedemic press, Orlando, Florida.
- ✓ Fava F, Federici F, Kalogerakis N, Mantzavinos D, Valorisation of agro-industrial by-products, effluents and waste: concept, opportunities and the case of olive mill wastewaters, *Journal of Chemical Technology & Biotechnology*, 2009, 84 (6), 895-900.
- ✓ Fernández-Ugalde O, Barré P, Hubert F, Virto I, Girardin C, Ferrage E, Caner L and Chenu C, Clay mineralogy differs qualitatively in aggregate-size classes: clay-mineral-based evidence for aggregate hierarchy in temperate soils. *European Journal of Soil Science*, 2013, **64** (4), 410-422.
- ✓ Fierro A, Norrie J, Gosselin A and Beauchamp CJ, Deinking sludge influences biomass , nitrogen and phosphorus status of several grass and legume species. Canadian Journal of Soil Science, 1997, **77** (4), 693–702.
- ✓ Fischer L, Zur Mühlen E, Brümmer GW and Niehaus H, Atomic force microscopy (AFM) investigations of the surface topography of a multidomain porous goethite. *European Journal of Soil Science*, 1996, **47,** 329–334.

- ✓ Foster MD, The relation between composition swelling in clays. *Clays and Clay Minerals*, 1954, **3** (1), 205–220.
- ✓ García R, De la Villa RV, Vegas I, Frías M and Sánchez de Rojas MI, The pozzolanic properties of paper sludge waste. *Construction and Building Materials*, 2008, **22** (7), 1484–1490.
- ✓ Grunewald E and Knight R, A laboratory study of NMR relaxation times and pore coupling in heterogeneous media. *Geophysics*, 2009, **74** (6), E215–E221.
- ✓ Haynes RJ, Naidu R, Influence of lime, fertilizer and manure applications on soil organic matter content and soil physical conditions: a review. *Nutrient Cycling in agroecosystems*, 1998, **51**, 123-137.
- ✓ Heister K, The measurement of the specific surface area of soils by gas and polar liquid adsorption methods—Limitations and potentials. *Geoderma*, 2014, 216, 75-87.
- ✓ Helm L, Relaxivity in paramagnetic systems: theory and mechanisms. *Prog Nucl Magn Reson Spectrosc*, 2006, 49(1):45–64
- ✓ Jaeger F, Bowe S, Van As H, Schaumann GE, Evaluation of ^{1}H NMR relaxometry for the assessment of pore-size distribution in soil samples. *European Journal of Soil Science*, 2009, **60** (6), 1052-106
- ✓ Kaiser K and Guggenberger G, Mineral Surfaces and Soil Organic Matter. *European Journal of Soil Science*, 2003, **54**, 219–236.
- ✓ Kleinberg RL, Utility of NMR T_2 distributions, connection with capillary pressure, clay effect, and determination of the surface relaxivity parameter ρ_2. *Magnetic Resonance Imaging*, 1996, **14**, 761–767.
- ✓ Kleinberg RL, Nuclear magnetic resonance. In Experimental methods in the physical sciences, Schlumberger-Doll Research, Ridgefield, Connecticut, 1999, Vol. 35, 337-385.
- ✓ Kuperman V, Magnetic resonance imaging. Physical principles and applications, Academic press, University of Chicago, 2000.
- ✓ Létal J, Jirák D, Šuderlová L, Hájek M, MRI 'texture' analysis of MR images of apples during ripening and storage, LWT - Food Science and Technology, 2003, 36, 719-727.
- ✓ Likon M and Trebše P, Recent Advances in Paper Mill Sludge Management. *Industrial Waste*, Prof. Kuan-Yeow Show (Ed.), 2012, ISBN: 978-953-51-0253-3, InTech, Available

from: http://www.intechopen.com/books/industrial-waste/papermill-sludge-as-valuable-raw-material

- ✓ Marcone M F, Wang S, Albabish W, Nie S, Somnarain D and Hill A, *Food Res. Int.*, 2013, **51**, 729-747.
- ✓ Mayer LM, Extent of coverage of mineral surfaces by organic matter in marine sediments. *Geochimica et Cosmochimica*, 1999, **63** (2), 207–215.
- ✓ Mayer LM, Xing B, Organic Matter–Surface Area Relationships in Acid Soils. *Soil Science Society of America Journal*, 2001, **65,** 250–258.
- ✓ Mayer LM, Schick LL, Hardy KR, Wagai R and McCarthy J, Organic Matter in Small Mesopores in Sediments and Soils. *Geochimica et Cosmochimica Acta*, 2004, **68** (19), 3863–3872.
- ✓ McMichael AJ, Powles JW, Butler CD, Uauy R, Food, livestock production, energy, climate change, and health, *Lancet*, 2007, 370, 1253-1263.
- ✓ Mitchell J, Gladden LF, Chandrasekera TC, Fordham EJ, Low-field permanent magnets for industrial process and quality control, *Progress in nuclear magnetic resonance spectroscopy*, 2014, 76, 1-60.
- ✓ Méndez A, Fidalgo JM, Guerrero F and Gascó G, Characterization and pyrolysis behaviour of different paper mill waste materials. *Journal of Analytical and Applied Pyrolysis*, 2009, **86**, 66–73.
- ✓ Mikutta C, Lang F and Kaupenjohann M, Soil organic matter clogs mineral pores: evidence from ^{1}H-NMR and N_2 adsorption. *Soil Science Society of America Journal*, 2004, **68** (6), 1853-1862.
- ✓ Mikutta R and Mikutta C, Stabilization of organic matter at micropores (<2nm) in acid forest subsoils. *Soil Science Society of America Journal*, 2006, **70** (6), 2049–2056.
- ✓ Mikutta R, Kleber M, Torn MS and Jahn R, Stabilization of soil organic matter: association with minerals or chemical recalcitrance? *Biogeochemistry*, 2006, **77** (1), 25–56.
- ✓ Miller FC, Matric water potential as an ecological determinant in compost, a substrate dense system, *Microb. Ecol.*, 1989, **18**, 59-71.
- ✓ Mirabella N, Castellani V and Sala S, Current options for the valorization of food manufacturing waste: a review, *J. Cleaner Prod*, 2013, **65**, 28-41.

- ✓ Mitreiter I, Oswald SE, Stallmach F, Investigation of Iron (III)- release in the pore water of natural sands by NMR relaxometry. *Open Magn Reson*, 2010, J 3:46–51.
- ✓ Mohan D, Pittman CU, Steele PH, Pyrolysis of Wood/Biomass for Bio-oil: A Critical Review, Energy & Fuels, 2006, 20 (3), 848-889.
- ✓ Nowacka M, Tylewicz U, Laghi L, Dalla Rosa M, Witrowa-Rajchert D, Effect of ultrasound treatment on the water state in kiwifruit during osmotic dehydration, Food chemistry, 2014, 144, 18-25.
- ✓ Pignatello JJ, Soil organic matter as nanoporous sorbent of organic pollutant. *Adv Colloid Interface Sci*, 1998, 76–77:445–467.
- ✓ Provencher SW, CONTIN: a general purpose constrained regularization program for inverting noisy linear algebraic and integral equations. *Comput Phys Commun*, 1982, 27(3):229–242.
- ✓ Rynk R, On-Farm Composting Handbook. Northeast Regional Agricultural Engineering Service, Cooperative Extension. Ithaca, New York, 1992.
- ✓ Rouquerol F, Rouquerol J and Sing K, *Adsorption by powders and porous solids*, 1999, Academic Press, San Diego USA.
- ✓ Séquaris JM, Guisado G, Magarinos M, Moreno C, Burauel P, Narres HD, Vereecken, H, Organic-carbon fractions in an agricultural topsoil assessed by the determination of the soil mineral surface area, *Journal of Plant Nutrition and Soil Science*, 2010, 173 (5), 699-705.
- ✓ Schaumann GE, Hobley E, Hurrass J and Rotard W, H-NMR relaxometry to monitor wetting and swelling kinetics in high-organic matter soils. *Plant and Soil*, 2005, 275, 1-20.
- ✓ Segrè A, Falasconi L, Il libro nero dello spreco alimentare in Italia [Italy's black book of food waste], 2011, Edizioni Ambiente
- ✓ Séquaris JM, Guisado G, Magarinos M, Moreno C, Burauel P, Narres HD and Vereecken H, Organic-Carbon fractions in an agricultural topsoil assessed by the determination of the soil mineral surface area. *Journal of Plant Nutrition and Soil Science*, 2010, 173 (5), 699–705.
- ✓ Sing KSW, Everett DH, Haul RAW, Moscou L, Pierotti RA, Rouquerol J and Siemieniewska T, Reporting physisorption data for gas/solid systems. *Pure Applied Chemistry*, 1985, 57, 603–619.

- ✓ Six J, Conant RT, Paul EA, Paustian K, Stabilization mechanisms of soil organic matter: Implications for C-saturation of soils. *Plant and soil*, 2002, 241, 155-176.
- ✓ Sykora S, Bortolotti V, Fantazzini P, PERFIDI: Parametrically enabled relaxation filters with double and multiple inversion, *Magn Reson Imag*, 2007, 25:529–532.
- ✓ Stevenson FJ, Organic matter in soils: pools, distribution, transformations, and function. In Humus chemistry: genesis, composition, reactions, 1994, pp 1-23, 2nd edn. Wiley and sons editors, New York
- ✓ Sundberg C and Jönsson H, Higher pH and faster decomposition in biowaste composting by increased aeration, *Waste Manag.*, 2008, **28** (3), 518–526.
- ✓ Vannini, M., Bonoli, A., Bortolotti, V. & Macini P. *In* Natural soil mixed with paper mill sludge characterization by ^{1}H nuclear magnetic resonance longitudinal relaxation time. 2012, *Proceedings of the 3rd congress on hazardous and waste materials*, 12–14 September 2012.
- ✓ Vogt C, Galvosas P, Klitzsch N, Stallmach F Self-diffusion studies of pore fluids in unconsolidated sediments by PFG NMR. *J Appl Geophys*, 2002, 50(4):455–467.
- ✓ Wagai R, Mayer LM and Kitayama K, Extent and nature of organic coverage of soil mineral surfaces assessed by a gas sorption approach. *Geoderma*, 2009, **149,** 152–160.
- ✓ Zeng Y, Trauth KM, Peyton RL and Banerji SK, Characterization of solid waste disposed at Columbia Sanitary Landfill in Missouri, *Waste Management and research*, 2005, 23 (1), 62-71.

- ✓ www.progression-systems.com
- ✓ www.zerowasteurope.eu
- ✓ www.ebyte.it Sykora
- ✓ www.nmr.uottawa.ca
- ✓ http://software.dicam.unibo.it/upenwin